

Laserspectroscopic determination of the nuclear charge radius of ^{13}C

Laserspektroskopische Bestimmung des Kernladungsradius von ^{13}C

Zur Erlangung des Grades eines Doktors der Naturwissenschaften (Dr. rer. nat.)

Genehmigte Dissertation von Patrick Matthias Müller aus Aschaffenburg

Tag der Einreichung: 16. Januar 2024, Tag der Prüfung: 14. Februar 2024

1. Gutachten: Prof. Dr. Wilfried Nörtershäuser

2. Gutachten: Prof. Dr. Thorsten Kröll

Darmstadt, Technische Universität Darmstadt



TECHNISCHE
UNIVERSITÄT
DARMSTADT

Fachbereich Physik
Institut für Kernphysik
AG Nörtershäuser



Laserspectroscopic determination of the nuclear charge radius of ^{13}C
Laserspektroskopische Bestimmung des Kernladungsradius von ^{13}C

Accepted doctoral thesis by Patrick Matthias Müller

Date of submission: 16. Januar 2024
Date of thesis defense: 14. Februar 2024

Darmstadt, Technische Universität Darmstadt

Bitte zitieren Sie dieses Dokument als:
URN: urn:nbn:de:tuda-tuprints-267460
URL: <https://tuprints.ulb.tu-darmstadt.de/26746>
Jahr der Veröffentlichung auf TUpprints: 2024

Dieses Dokument wird bereitgestellt von tuprints,
E-Publishing-Service der TU Darmstadt
<https://tuprints.ulb.tu-darmstadt.de>
tuprints@ulb.tu-darmstadt.de

Die Veröffentlichung steht unter folgender Creative Commons Lizenz:
Namensnennung 4.0 International
<https://creativecommons.org/licenses/by/4.0/>
This work is licensed under a Creative Commons License:
Attribution 4.0 International
<https://creativecommons.org/licenses/by/4.0/>

Erklärungen laut Promotionsordnung

§ 8 Abs. 1 lit. c PromO

Ich versichere hiermit, dass die elektronische Version meiner Dissertation mit der schriftlichen Version übereinstimmt.

§ 8 Abs. 1 lit. d PromO

Ich versichere hiermit, dass zu einem vorherigen Zeitpunkt noch keine Promotion versucht wurde. In diesem Fall sind nähere Angaben über Zeitpunkt, Hochschule, Dissertationsthema und Ergebnis dieses Versuchs mitzuteilen.

§ 9 Abs. 1 PromO

Ich versichere hiermit, dass die vorliegende Dissertation selbstständig und nur unter Verwendung der angegebenen Quellen verfasst wurde.

§ 9 Abs. 2 PromO

Die Arbeit hat bisher noch nicht zu Prüfungszwecken gedient.

Darmstadt, 16. Januar 2024

P. Müller

Abstract

Light nuclei, that consist of only a few nucleons, are exciting testing grounds for our understanding of fundamental interactions. Bound by the residual strong interaction acting between the quarks inside the protons and neutrons, these nuclei form interesting structures such as condensed α clusters or halo nuclei that are challenging to describe by nuclear theory. Over the last decades, *ab initio* nuclear structure calculations, that are rooted in quantum chromodynamics, were improved significantly. Providing precise benchmark values for these theories is essential to improve the precision of predictions on how nuclear matter emerges. The isotopes of the light element carbon (C) are highly interesting cases to study as they exhibit pronounced α clustering and are important contributors to the nucleosynthesis process in stars. Additionally, C is at the limit of what is computationally possible using higher-order nuclear structure calculations, and due to its unfavorable spectral properties, no experimental high-precision spectroscopy data is available so far.

In this work, the differential nuclear charge radius of $^{12,13}\text{C}$ is determined purely from results of *ab initio* nonrelativistic quantum electrodynamics atomic structure calculations and high-precision collinear laser spectroscopy measurements carried out at the Collinear Apparatus for Laser Spectroscopy and Applied Science (COALA), located at the Institute for Nuclear Physics at the Technical University Darmstadt. For this, first high-accuracy measurements of the $1s2s\ ^3\text{S}_1 \rightarrow 1s2p\ ^3\text{P}_{0,1,2}$ transitions in He-like $^{13}\text{C}^{4+}$ were carried out and combined with measurements in $^{12}\text{C}^{4+}$ from preceding work. The C $^{4+}$ isotopes in the metastable $^3\text{S}_1$ state are produced in an electron beam ion source and are accessible with lasers operated at a wavelength of 227.6 nm. The fluorescence detection region (FDR) of COALA at these deep-UV wavelengths was improved with a new lens-based FDR designed and built within this work. The new segment provides an improved signal-to-noise ratio compared to the previous mirror-based design. This considerably facilitated spectroscopy of the weakest transitions in $^{13}\text{C}^{4+}$, which split into hyperfine structure (HFS). The effect of hyperfine-induced mixing on the transition frequencies is investigated and benchmark values for atomic structure calculations are provided. The new model-independent $\delta\langle r^2 \rangle^{12,13} = -0.1245(66) \text{ fm}^2$ is compared to results from elastic electron scattering, muonic atom spectroscopy and *ab initio* nuclear structure calculations. In combination with the existing experimental results for ^{12}C , the absolute nuclear charge radius of ^{13}C is determined. An elaborate analysis of the fluorescence spectra and potential systematic uncertainties is presented that is enabled by the new Python package *qspec*, developed within this work for simulations and data analysis surrounding laser spectroscopy. The package was extensively tested during beamtimes at GSI, CERN/ISOLDE and ANL where it significantly contributed to decision-making processes by enabling a detailed live data analysis and simulations. In addition to the analysis of $^{13}\text{C}^{4+}$, an investigation of quantum interference effects and optical-population transfer in the HFS of $^{87}\text{Sr}^+$ is presented in the appendix.

Zusammenfassung

Leichte Kerne, die nur aus wenigen Nukleonen bestehen, sind ausgezeichnete Objekte, um unser Verständnis fundamentaler Wechselwirkungen zu überprüfen. Gebunden durch die verbleibende starke Wechselwirkung, die zwischen den Quarks im Inneren der Protonen und Neutronen wirkt, bilden diese Kerne interessante Strukturen wie kondensierte α -Gruppen (Cluster) oder Halo-Kerne, deren kerntheoretische Beschreibung herausfordernd ist. In den letzten Jahrzehnten wurden in der Quantenchromodynamik verwurzelte *ab initio* Kernstrukturberechnungen erheblich verbessert. Die Bereitstellung genauer Referenzwerte für diese Theorien ist unerlässlich, um die Präzision von Vorhersagen über die Entstehung der Kernmaterie zu verbessern. Die Isotope des leichten Elements Kohlenstoff (C) sind hochinteressant, da sie ausgeprägte α -Cluster aufweisen und ein wichtiger Bestandteil des Nukleosyntheseprozesses in Sternen sind. Darüber hinaus liegt C an der Grenze dessen, was mit Kernstrukturberechnungen höherer Ordnung berechenbar ist, und aufgrund seiner ungünstigen spektralen Eigenschaften sind bisher auch keine experimentellen hochpräzisen Spektroskopiedaten verfügbar.

In dieser Arbeit wird der differentielle Kernladungsradius von $^{12,13}\text{C}$ rein aus Ergebnissen von *ab initio* nichtrelativistischen quantenelektronodynamischen Atomstrukturrechnungen und hochpräzisen kollinearen Laserspektroskopie-Messungen bestimmt, die an der Kollinearen Apparatur für Laserspektroskopie und Angewandte Wissenschaft (KOALA) am Institut für Kernphysik der Technischen Universität Darmstadt durchgeführt wurden. Dazu wurden erstmals hochgenaue Messungen der $1s2s\,{}^3\text{S}_1 \rightarrow 1s2p\,{}^3\text{P}_{0,1,2}$ Übergänge in He-ähnlichem $^{13}\text{C}^{4+}$ durchgeführt und mit Messungen in $^{12}\text{C}^{4+}$ aus einer vorangegangenen Arbeit kombiniert. Die C^{4+} -Isotope im metastabilen ${}^3\text{S}_1$ -Zustand werden in einer Elektronenstrahl-Ionenquelle erzeugt und sind mit Lasern zugänglich, die bei einer Wellenlänge von 227,6 nm betrieben werden. Die Fluoreszenzdetektionsregion (FDR) von KOALA wurde mit einer neuen linsenbasierten FDR verbessert, die im Rahmen dieser Arbeit entwickelt und gebaut wurde. Das neue Segment bietet ein verbessertes Signal-zu-Rausch-Verhältnis im Vergleich zu dem früheren spiegelbasierten Design. Dies erleichterte die Spektroskopie der schwächsten Übergänge in $^{13}\text{C}^{4+}$, die sich durch die Hyperfeinstruktur aufspalten, erheblich. Die Auswirkung der hyperfein-induzierten Mischung auf die Übergangsfrequenzen wird untersucht und es werden Referenzwerte für Atomstrukturberechnungen angegeben. Der neue modellunabhängige $\delta\langle r^2 \rangle^{12,13} = -0,1245(66) \text{ fm}^2$ wird mit Ergebnissen aus elastischer Elektronenstreuung, Spektroskopie myonischer Atome und *ab initio* Kernstrukturrechnungen verglichen. In Kombination mit den vorhandenen experimentellen Ergebnissen für ^{12}C wird der absolute Kernladungsradius von ^{13}C bestimmt. Die ausführliche Analyse der Fluoreszenzspektren und möglicher systematischer Unsicherheiten wurde durch das neue Python-Paket *qspec* ermöglicht, das im Rahmen dieser Arbeit für Simulationen und Datenanalyse rund um die Laserspektroskopie entwickelt wurde. Das Paket wurde ausgiebig während mehrerer Strahlzeiten an GSI, CERN/ISOLDE und ANL getestet, wo es durch

eine detaillierte Live-Datenanalyse und Simulationen wesentlich zu Entscheidungsprozessen beitrug. Neben der Analyse von $^{13}\text{C}^{4+}$ wird als Ergänzung noch eine Untersuchung von Quanteninterferenzeffekten und optischem Populationstransfer in der Hyperfeinstruktur von $^{87}\text{Sr}^{+}$ im Anhang dieser Arbeit vorgestellt.

Contents

1	Introduction	1
2	Theoretical background	5
2.1	Nuclear structure	5
2.1.1	Nuclear structure of $^{12,13}\text{C}$	5
2.1.2	Chiral effective field theory	6
2.1.3	In-medium similarity renormalization group	10
2.2	Atomic structure	11
2.2.1	Atomic structure of C^{4+}	11
2.2.2	Hyperfine structure	12
2.2.3	Zeeman effect	15
2.2.4	Finite nuclear-size effect	16
2.2.5	Nonrelativistic QED in helium-like systems	19
2.2.6	Isotope shift	22
2.3	Fluorescence spectroscopy	23
2.3.1	Resonance lineshapes	24
2.3.2	Collinear laser spectroscopy	25
2.3.3	Photon recoil	27
2.4	Laser-atom interactions	28
2.4.1	Hamiltonian of an atom in classical Laser fields	29
2.4.2	The Lindblad master equation	30
2.4.3	Rate equations	32
2.4.4	Monte-Carlo master equation	32
2.4.5	Photon scattering rate	33
3	Python package <i>qspec</i>	37
3.1	Structure	37
3.2	Modular lineshape models	38
3.2.1	Modular system	39
3.2.2	Benchmark	40
3.3	Simulation of laser-atom interactions	42
3.3.1	Structure of <i>qspec.simulate</i>	42
3.3.2	Coordinate transformations	43
3.3.3	Construction of differential equations	46
3.3.4	Outlook	49

4 Experimental setup	51
4.1 Electron beam ion source	51
4.1.1 Production of $^{13}\text{C}^{4+}$ from CH_4 and CO_2	52
4.2 Laser spectroscopy beamline	53
4.3 Fluorescence detection region	56
4.3.1 Lens-based FDR	57
4.4 Laser setup	62
4.4.1 Laser beam production	62
4.4.2 Laser beam position stabilization	64
4.4.3 Laser- and ion-beam alignment	65
5 Collinear laser spectroscopy in $^{13}\text{C}^{4+}$	69
5.1 Fluorescence spectra of $^{13}\text{C}^{4+}$	69
5.1.1 Calibration of the Doppler shift	70
5.1.2 Background-free laser spectroscopy	71
5.1.3 Test of saturation spectroscopy	73
5.2 Determination of transition frequencies	75
5.2.1 Fitting fluorescence spectra	76
5.2.2 Selection criteria of measurements	76
5.2.3 Systematic uncertainties	79
5.2.4 Derivation of the final transition frequencies	83
5.3 Hyperfine structure of $^{13}\text{C}^{4+}$	84
5.4 Nuclear charge radius of ^{13}C	87
5.5 Nuclear structure calculations	90
5.6 Transition frequencies from pulsed operation	92
6 Conclusion and outlook	95
A Appendix	99
A.1 Quantum interference tests in $^{87}\text{Sr}^+$	99
Bibliography	107

List of Figures

2.1	Atomic level scheme of $^{12,13}\text{C}^{4+}$	12
2.2	Principle of collinear laser spectroscopy	26
2.3	Monte-Carlo simulation of photon recoils	34
3.1	Class diagram of <i>qspec.models</i>	39
3.2	Performance benchmark of <i>qspec.models</i>	41
3.3	Class diagram of <i>qspec.simulate</i>	43
3.4	Standard coordinate system of <i>qspec.simulate</i>	44
3.5	Transformation into the interaction picture in <i>qspec.simulate</i>	46
4.1	Electrostatic potentials in the electron beam ion source (EBIS)	52
4.2	Wienfilter spectrum of $^{13}\text{CH}_4$ and $^{13}\text{CO}_2$	53
4.3	Source region of the COALA beamline	54
4.4	Laser spectroscopy region of the COALA beamline	54
4.5	Cross sections of the ion beam	55
4.6	Fluorescence detection region (FDR)	56
4.7	Geometric efficiency of the FDR in dependence of its degrees of freedom	58
4.8	Geometric efficiency of the FDR in dependence of the source properties	59
4.9	Geometric efficiency of the FDR in dependence of the emission angle	60
4.10	Signal-to-noise ratios of the $^{13}\text{C}^{4+}$ measurements	61
4.11	Laser setup	63
4.12	Collinear and anticollinear laser beam paths	64
4.13	Signal of the laser beam position stabilization	65
4.14	Laser beam diameters along the beamline	66
5.1	Standard fluorescence spectrum of $^{13}\text{C}^{4+}$	69
5.2	Calibration of the voltage potential in the FDR	70
5.3	Resonance signals of the $1s2s\ ^3\text{S}_1 \rightarrow 1s2p\ ^3\text{P}_{0,1,2}$ transitions in $^{13}\text{C}^{4+}$	72
5.4	Resonance signals from saturation spectroscopy	73
5.5	Selection criteria of the $^{13}\text{C}^{4+}$ measurements	77
5.6	Fluorescence spectra of $^{13}\text{C}^{4+}$ rejected by different selection criteria	78
5.7	Transition frequencies of $^{13}\text{C}^{4+}$ from continuous EBIS operation	83
5.8	Hyperfine structure (HFS) spectrum of $^{13}\text{C}^{4+}$	85
5.9	Absolute and relative nuclear charge radii of $^{12,13}\text{C}$	88
5.10	Resonance signal of $^{13}\text{C}^{4+}$ recorded in pulsed EBIS operation	92
5.11	Transition frequencies of $^{13}\text{C}^{4+}$ from pulsed EBIS operation	93

A.1	Atomic level scheme of $^{87}\text{Sr}^+$	99
A.2	HFS spectrum of $^{87}\text{Sr}^+$ recorded with a lens system and low laser power	100
A.3	HFS spectrum of $^{87}\text{Sr}^+$ recorded with a lens system and high laser power	101
A.4	HFS spectrum of $^{87}\text{Sr}^+$ recorded with a mirror system and high laser power	103
A.5	Polarization sensitivity of the FDR	105

List of Tables

2.1	Basic nuclear properties of $^{12,13}\text{C}$	6
2.2	Power counting expansion of chiral effective field theory	9
2.3	The electron magnetic dipole matrix $T^{(1)}$	15
2.4	Center-of-gravity formulas for the $1s2s\,{}^3\text{S}_1 \rightarrow 1s2p\,{}^3\text{P}_{0,1,2}$ transitions	23
5.1	Transition frequencies of the $1s2s\,{}^3\text{S}_1 \rightarrow 1s2p\,{}^3\text{P}_{0,1,2}$ transitions in $^{13}\text{C}^{4+}$	75
5.2	Systematic uncertainties of the transition frequencies in $^{13}\text{C}^{4+}$	79
5.3	Results of photon-recoil simulations	81
5.4	Center-of-gravity frequencies of $^{13}\text{C}^{4+}$	85
5.5	Hyperfine structure parameters of $^{13}\text{C}^{4+}$	86
5.6	Isotope shifts between $^{12,13}\text{C}^{4+}$	87
5.7	Absolute and relative nuclear charge radii of $^{12,13}\text{C}$	89
5.8	Theoretical nuclear charge radii of $^{12,13}\text{C}$ from IMSRG calculations	91
5.9	Absolute transition frequencies determined in pulsed EBIS operation	93
A.1	Agreement of QI fit models with the hyperfine structure spectrum of $^{87}\text{Sr}^+$	102

1 Introduction

The description of nuclear structure beyond a point-like core got accelerated by the development of the nuclear shell model in 1949, for which Maria Goeppert Mayer and Hans D. Jensen together got awarded half of the physics Nobel Price in 1963 [1, 2]. From here, a golden-age of nuclear physics started that set forth the fundamental understanding of matter we use today. Already in the 1960s, the standard model of particle physics was developed and finalized only ten years later after the experimental discovery of the quarks [3, 4]. Calculations in the framework of the underlying theory of quantum chromodynamics (QCD) are extremely challenging and as of today, a prediction of multi-nucleon structures to meaningful precision require some form of effective theory, such as chiral effective field theory [5, 6]. In this *ab initio* theory, the interaction between the nucleons is expanded in a series of fundamental interactions that are ordered based on their importance. Different approaches were developed in the last decades that are able to predict nuclear electromagnetic moments and radii up to mass number $A \sim 80$ from first principle [7, 8]. These predictions need to be validated by experiments. Ever since the 1980s, collinear laser spectroscopy (CLS) has been proven to be a powerful method to determine nuclear properties across the entire nuclear chart [9–13]. The most common application is the determination of nuclear electromagnetic moments and differential mean-square charge radii

$$\delta \langle r^2 \rangle^{A,A'} := \langle r^2 \rangle^{A'} - \langle r^2 \rangle^A \quad (1.1)$$

from hyperfine structure spectra and isotope shift measurements, respectively. The lightest elements and their isotopes are particularly interesting cases to study. Due to their small amount of protons and neutrons, adding or removing a nucleon can lead to drastic structural changes. One interesting structure is the appearance of α clusters that can be observed throughout the light elements [14–21]. The transition between the independent particle shell model and a cluster-like structure can be understood by increasing multinucleon correlations due to residual short-range interactions. The strongly bound nucleus of ^{12}C is thought to be a cluster and mean-field coexisting system dominated by a $p_{3/2}$ subshell-closed configuration with significant admixture of a 3α cluster component [22–25]. The additional neutron in ^{13}C creates a covalent bond between the 3α cluster [18]. Several experimental approaches are actively pursued to uncover the complex structures of C isotopes [26]. In ^{12}C , direct detection of decay products from excited cluster states is used to gain information about the decaying state [27, 28], such as the excited Hoyle 0^+ state that is expected to play a major role in the nucleosynthesis process in stars [29]. In ^{13}C , elastic and inelastic scattering processes and nuclear (transfer) reactions are utilized to populate cluster states [30–33]. In these experiments, mainly energies

and decay properties of excited states are determined. Complementary to these, an accurate determination of the nuclear charge radius of ^{13}C relative to ^{12}C provides information on the structural change when compared with nuclear structure calculations. For ^{12}C , already several results from elastic electron scattering (e^- -scattering) [34–37] and muonic atom spectroscopy (μ -atoms) [38, 39] exist. However, for ^{13}C , only a single e^- -scattering [40] but comparable μ -atoms results [38, 41] are available. Both methods are model-dependent. In combination with *ab initio* atomic structure calculations, CLS can provide a model-independent result that not only serves as a benchmark value for theory but also for the other available experimental methods.

Another interesting structure in light nuclei are nucleon-halos, where one or two nucleons are well separated from the remaining core [42]. For example, in lithium, the size of the nucleus continuously decreases in $^{6–9}\text{Li}$ with the addition of neutrons. Adding another neutron yields the unbound ^{10}Li , while adding two neutrons results in ^{11}Li which exists as a ^9Li core with a two-neutron halo [19, 43–47]. In beryllium, single- and two-neutron halos are present in ^{11}Be and ^{14}Be , respectively [20, 48–53]. In contrast to the more common neutron-rich halo nuclei, the neutron-deficient isotope ^8B is expected to consist of a ^7Be core and a proton-halo [54–60]. However, the existence of a proton-halo in ^8B , which has not been found in any other element so far, has yet to be confirmed with a precise direct measurement of the nuclear charge radius. This work is part of the endeavor to establish the nuclear charge radius of ^8B using CLS. By combining high-precision CLS measurements with *ab initio* nonrelativistic quantum electrodynamics (NRQED) calculations in helium-like $^{10,11}\text{B}^{3+}$, absolute reference radii can be determined that are so far not available to the required precision from e^- -scattering or μ -atoms. The proton-halo would then be confirmed by determining the radius of ^8B relative to the references and the already known radius of ^7Be .

As a first test of this combined experimental and theoretical approach, previously the well-known nuclear charge radius of ^{12}C was determined from measurements of the $1s2s\,^3\text{S}_1 \rightarrow 1s2p\,^3\text{P}_{0,1,2}$ transition frequencies at the Collinear Apparatus for Laser Spectroscopy and Applied Science (COALA) [61, 62] in combination with NRQED calculations up to the order $m\alpha^7$ [63–65]. While the uncertainty of the absolute nuclear charge radius of ^{12}C extracted from this approach is currently limited by the theoretical precision, which is two orders of magnitude lower than the experimental precision, the fine-structure splittings of the $^3\text{P}_{0,1,2}$ states serve as valuable benchmark values for theory. These can be used to identify the leading order terms in the next higher order $m\alpha^8$ that are needed to further improve the theoretical precision. With the expected improvements and the increased precision due to the lower Z , in $^{10,11}\text{B}^{3+}$, the available theoretical precision would meet the requirements to identify the halo character of ^8B . However, the nonzero nuclear spins of $^{10,11}\text{B}$ constitute an additional challenge. The hyperfine structure in light helium-like systems is modulated by hyperfine-induced mixing, which shifts the center-of-gravity frequencies of the individual $^3\text{S}_1 \rightarrow ^3\text{P}_J$ transitions. With a nuclear spin of $1/2$, $^{13}\text{C}^{4+}$ is an ideal system to systematically investigate these shifts. When results from NRQED are available for $^{10,11}\text{B}^{3+}$, the underlying calculations must simultaneously reproduce the experimental results for $^{12,13}\text{C}^{4+}$.

In this work, measurements of the $1s2s\,^3\text{S}_1 \rightarrow 1s2p\,^3\text{P}_{0,1,2}$ transition frequencies of $^{13}\text{C}^{4+}$, produced with an electron beam ion source (EBIS) at COALA, are presented. The transition

freqencies are used to determine the isotope shift of $^{12,13}\text{C}^{4+}$ using the previous results for $^{12}\text{C}^{4+}$ from [64]. In combination with NRQED calculations, $\delta\langle r^2 \rangle^{12,13}$ is determined and compared to existing values from e^- -scattering and μ -atoms as well as new theoretical values that were provided by M. Heinz *et. al.* In combination with the precisely known charge radius of ^{12}C , the differential radius determined within this work is used to derive an improved absolute radius for ^{13}C that can also be compared to literature. The essential experimental results that enable the precise determination of the nuclear charge radius are the absolute frequencies of the nine transitions between the hyperfine structure states of $^{13}\text{C}^{4+}$. Therefore, great emphasis was placed on an accurate description of the absolute frequency determination and potential systematic errors. For example, in light systems with transitions in the laser-accessible UV-regime, the influence of photon recoils can be large, as the velocity change of a light system upon a single photon absorption is large [20, 64]. An accurate treatment of the laser-atom interactions enables a thorough analysis of systematic uncertainties that ideally are neither under- nor overestimated.

Within this work, the Python package *qspec* was developed that provides a module to simulate interactions of an atom with classical lasers. Here, it was used to accurately estimate uncertainties originating from photon recoils and the Zeeman effect. Additionally, the description of time-evolved quantum interference (QI) effects was tested using measurements of the $5s\ ^2\text{S}_{1/2} \rightarrow 5p\ ^2\text{P}_{3/2}$ transition in $^{87}\text{Sr}^+$. Fits of fluorescence spectra were carried out with a modular system of lineshape models that is also included in *qspec*. The module can be compared to the well-established *satlas2* package that is used by laser spectroscopy groups at KU Leuven, CERN/ISOLDE and JYVL [66, 67], but provides additional models, features and a performance boost.

2 Theoretical background

This chapter aims to provide the theoretical background required for this work. An introduction to nuclear and atomic structure theory, the interaction between light and matter and the experimental method of collinear laser spectroscopy is given.

2.1 Nuclear structure

Nuclear structure refers to the formation of a nucleus from its constituents, the protons and neutrons and to some extend their constituents, the quarks. This section provides an overview of the nuclear structure of $^{12,13}\text{C}$ especially and chiral effective field theory and the in-medium similarity renormalization group in general, which is a state-of-the-art framework for *ab initio* nuclear structure calculations.

2.1.1 Nuclear structure of $^{12,13}\text{C}$

Carbon is the family of nuclei which have six protons. The isotopic chain of carbon contains two stable isotopes, ^{12}C and ^{13}C , which have six and seven neutrons, respectively. Some basic properties of the $^{12,13}\text{C}$ nuclei are listed in Tab. 2.1. In the nuclear shell-model picture, the protons and six of the neutrons each occupy the two $1s_{1/2}$ states of the *s*-shell and the four $1p_{3/2}$ states of the *p*-shell. The extra neutron of ^{13}C then occupies a $1p_{1/2}$ state, resulting in a nuclear spin of $I = 1/2$. Due to the unpaired neutron, ^{13}C has a smaller binding energy per nucleon than ^{12}C that in turn is strongly bound due to the closed $1p_{3/2}$ neutron subshell. Directly produced from the 3α fusion process, the occurrence of ^{12}C in nature is favored with a natural abundance of 98.94(6) % [68]. The nuclear charge radius of the stronger bound ^{12}C is larger than that of ^{13}C [34–41]. This behavior also can be observed in other light nuclei such as Li [19], Be [20] or B [21] and can be explained with the formation of clusters of nucleons, predominantly α -cluster consisting of two protons and two neutrons. Adding neutrons to an existing cluster structure increases the binding strength between the clusters while the total binding energy per nucleon decreases. Hence, $^{12,13}\text{C}$ may be explained by three α -clusters that are bound together [22–25]. In reality, any system will not purely exhibit a cluster structure or an idealized shell model configuration but be a mixture of different structures. This superposition of fundamentally different structures makes these systems computationally challenging and, therefore, interesting cases for benchmarking nuclear structure calculations which will be elucidated in the following.

Table 2.1: Basic nuclear properties of $^{12,13}\text{C}$.

Property	^{12}C	^{13}C	Reference
Natural abundance (%)	98.94 (6)	1.06 (6)	[68]
Mass (u)	12	13.003 354 835 34 (25)	[69]
Binding energy per nucleon (MeV)	7.680 145 (5)	7.469 850 (5)	[69]
Nuclear spin	0	$1/2^-$	[70]
Nuclear magnetic moment (μ_N)	0	0.702 369 (4)	[70]
Nuclear g -factor	0	1.404 738 (8)	[70]
Proton shell configuration	$1s_{1/2}^2 1p_{3/2}^4$	$1s_{1/2}^2 1p_{3/2}^4$	
Neutron shell configuration	$1s_{1/2}^2 1p_{3/2}^4$	$1s_{1/2}^2 1p_{3/2}^4 1p_{1/2}$	

2.1.2 Chiral effective field theory

This section gives an overview over the framework of chiral effective field theory (EFT) and the in-medium similarity renormalization group (IMSRG) approach that was used to determine the theoretical nuclear charge radii presented in this work. The theoretical description and the used naming conventions are based on [6, 71, 72]. For a more detailed overview, please refer to these articles. To motivate the use of chiral EFT, a short summary of other methods is given first.

Status of other methods

The formation of nuclei is governed by the strong interaction and the electromagnetic force acting between the charged protons. Therefore, a true *ab initio* description of nuclear structure needs to be derived from the description of the quark-gluon dynamics. The theoretical framework for this is quantum chromodynamics (QCD) [6]. Finding solutions for systems of light quarks at low energies ($E \ll 1 \text{ GeV}$), as applicable in the case of neutrons and protons, is computationally challenging due to the running of the coupling constant of the strong interaction α_S . The perturbative approach, ordering contributions to the solution based on their importance using a power series in α_S fails since the coupling constant is of the order of one at this energy scale. The state-of-the-art non-perturbative approach to solve these “strong QCD” problems is Lattice QCD. It was successful in predicting the mass of several light hadrons [73]. Recently, the determination of nuclear charge radii of light nuclei came in reach using a new method called wave function matching, that makes use of the framework of chiral EFT [74, 75].

Any nuclear structure theory can make use of the fact that the inner structures of the protons and neutrons are not resolved at low energies. The inner degrees of freedom are “frozen” and the dynamics are governed only by the interaction of the colorless hadrons. In classical approaches, phenomenological two-body potentials, such as the Argonne v_{18} potential, are used to describe the nucleon-nucleon dynamics [76, 77]. However, these approaches have difficulties in including necessary ($n \geq 3$)-body interactions since there is no experimental data to fix the respective model parameters. An example of an extension to the Argonne v_{18}

potential is the Illinois-7 potential [78]. Although these approaches are successful in predicting binding energies in light nuclei up to $A = 12$, the results are model-dependent and it is difficult to specify theoretical uncertainties. Moreover, the underlying fundamental symmetries of QCD must be included explicitly, as there is no direct connection to QCD [71].

Derivation of the theory

Chiral EFT is directly derived from the QCD Lagrangian and, hence, inherently maintains the chiral and gauge symmetries of QCD. Contributions to free-space nucleon interactions are ordered based on importance in a power counting expansion [71] and combined to build nuclear systems. Therefore, it is an *ab initio* theory in the sense that it is directly founded in QCD and does not start out with a certain model potential but with the fundamental interactions that produce the many-body potentials. In the following, the fundamentals of QCD are introduced.

QCD symmetries QCD describes the dynamics of quarks, *i.e.*, the elementary constituents of the proton and the neutron. There are six so-called flavors of quarks that can be split into two sets of three depending on whether their charge is positive or negative. The first set has charge $2/3$ in units of the elementary charge e and includes the *up*, *charm* and *top* quarks (u, c, t), the second set has charge $-1/3$ and includes the *down*, *strange* and *bottom* quarks (d, s, b). All quarks are spin- $1/2$ particles. The strong interaction acts between the quarks which have a so-called color charge that can take three different values: red, green and blue. Quarks only appear in bound states with other quarks such that the bound system is colorless. This can either be a combination of all three colors or a pair of a color and its anticolor (negative color charge). This phenomenon is called confinement. The strong interaction between the color charges is described by a local non-abelian gauge symmetry $SU(3)_{\text{color}}$. Consequently, there are eight gauge bosons, the gluons, corresponding to the eight generators of $SU(3)_{\text{color}}$ that mediate the force between the quarks. The QCD lagrangian can be written as [71]

$$\mathcal{L}_{\text{QCD}} = -\frac{1}{2g^2} \text{Tr}(G_{\mu\nu}^a G_a^{\mu\nu}) + \bar{q}^i i\gamma^\mu (D_\mu)_{ij} q^j - \bar{q}_i \mathcal{M} q^i = \mathcal{L}_{\text{QCD}}^0 - \bar{q} \mathcal{M} q, \quad (2.1)$$

where G is the gluon field strength tensor with a indexing the eight gluons and μ and ν indexing space-time, g is the gauge coupling constant, q_i are the quark fields $q_i^T(x) = (u_i(x), d_i(x), c_i(x), \dots)$ with color 3-index i , D_μ is the gauge covariant derivative that couples the quark fields to the gluon field, γ^μ are the Dirac matrices and \mathcal{M} is the mass tensor defining the masses of the quarks. The Einstein summation notation is applied in all indexes. The colorless protons and neutrons only consist of the two lightest quarks (u, d) which have masses 2.2 and 4.7 MeV/c² [79]. Taking only these two into consideration such that $q_i^T(x) = (u_i(x), d_i(x))$ and setting their masses to zero since $m_{u/d} \ll 1$ GeV, the QCD Lagrangian is given by the mass-independent $\mathcal{L}_{\text{QCD}}^0$. This Lagrangian obeys an additional symmetry. The two quarks are identical with respect to the strong interaction. Hence, for both chiralities $I \in \{L, R\}$, there exists an independent set $SU(2)_I$ of unitary transformations whose generators can be used to define conserved axial ($A = L - R$) and vector ($V = L + R$) currents [71]

$$A_k^\mu = \bar{q} \gamma^\mu \gamma_5 \frac{\sigma_k}{2} q, \quad V_k^\mu = \bar{q} \gamma^\mu \frac{\sigma_k}{2} q, \quad (2.2)$$

where σ_k are the Pauli-matrices, the generators of $SU(2)$. This is called chiral symmetry. In reality, the quarks are not massless. Hence, chiral symmetry is only an approximation and the axial and vector currents are not conserved. A consequence of the explicitly broken chiral symmetry is the existence of light Goldstone bosons [71, 80, 81]. The number of these bosons is equal to the number of generators of the corresponding broken symmetry group $SU(2)$ and can be identified as the three pions $|\pi^- \rangle = |d\bar{u}\rangle$, $|\pi^+ \rangle = |u\bar{d}\rangle$ and $|\pi^0 \rangle = \frac{1}{\sqrt{2}}(|u\bar{u}\rangle - |d\bar{d}\rangle)$. The pions are crucial in explaining the attractive force between the colorless nucleons. Single pion exchange is responsible for the long-range behavior of the nucleon-nucleon (NN) interaction and two-pion exchange is the main contribution to the intermediate range attractive force (~ 0.9 fm) [71]. A strong repulsive behavior between nucleons at small distances ($\lesssim 0.7$ fm) is a consequence of the spin-spin interaction of the quarks [82, 83].

Power counting expansion An effective field theory (EFT) can be build based on these fundamental interactions. Contributions to the full Lagrangian are ordered based on importance in a power counting expansion in Ω/Λ_χ with leading order (LO) Ω^0/Λ_χ^0 . Here, Ω is the energy scale of the system defined by the momenta of the nucleons and Λ_χ is the energy above which additional degrees of freedom are resolved. The breakdown energy Λ_χ is directly associated with the mass of the lightest particle or field excitation that is not explicitly considered in the EFT. For example, in pion-less perturbative EFT, where no particles are considered other than the nucleons, only contact interactions contribute and the breakdown energy is $\Lambda_\chi = m_\pi c^2 \approx 140$ MeV [79], implicating the condition $Q \ll m_\pi c^2$. In so-called pion-full chiral EFT, there are two contributions to the LO of the power counting expansion: The contact interaction and the single pion exchange. The breakdown energy becomes the mass of the next heavier particles, the σ -meson [72] and hence, $\Lambda_\chi = m_\sigma c^2 \approx 500$ MeV [79]. There was a long standing controversy about the existence of the σ -meson which is believed to be rather a two-pion molecule than a classical quark-antiquark pair [84, 85]. However, its existence is confirmed now and its name was changed to $f_0(500)$. The considered energies in pion-full EFT are of the order of the pion mass $Q \approx m_\pi c^2$. It must be ensured that Q is well below the energy of Δ resonances $E_\Delta - E_{p/n} \approx 300$ MeV. Otherwise, these also need to be considered explicitly [72, 86]. The Lagrangians of the LO in pion-full chiral EFT can be found in [71] and will not be discussed here. The next-to-leading-order (NLO) terms are of the order of Ω^2/Λ_χ^2 and include two-pion exchanges and higher order contact interactions. Note that there are no contributions of the order of Ω/Λ_χ due to the parity invariance of the strong interaction, as only terms linear in the particle momenta contribute. At the next-to-next-to-leading-order (N^2LO), in addition to the two-body interactions, also three-body interactions need to be considered. This is a consequence of treating the nucleons as point-like particles, which are actually extended bodies distorted in the proximity of other nucleons [6, 71]. The mathematical expressions of the individual contributions are directly linked to Feynman diagrams. In Tab. 2.2, a collection of the Feynman diagrams contributing to the power counting expansion is shown for two-body and

three-body interactions up to $N^3\text{LO}$. Higher order terms up to $N^4\text{LO}$ and four-body interactions are already developed and considered, *e.g.*, in [6, 71]. The contact interaction contributions depend on free coupling parameters which need to be derived from QCD or experimental results from two-nucleon scattering or deuteron properties [6].

Table 2.2: Selection of Feynman diagrams of the power counting expansion. The numbers next to the diagrams specify the amount of free parameters that need to be added at the given order. The three dots below indicate that there are more than the drawn diagrams. The missing columns in $N^2\text{LO}$ indicate that there are no new loop and contact interaction diagrams at this order. Vertices of dimension $\Delta = 0, 1, 2$ and 4 are drawn as dots, circles, squares and diamonds, respectively. The table is adapted from those found in [6, 71].

	NN	3N
LO $\mathcal{O}(Q^0/\Lambda_\chi^0)$		
NLO $\mathcal{O}(Q^2/\Lambda_\chi^2)$		
$N^2\text{LO}$ $\mathcal{O}(Q^3/\Lambda_\chi^3)$		
$N^3\text{LO}$ $\mathcal{O}(Q^4/\Lambda_\chi^4)$		

Renormalization The Lagrangians associated with the contact-interaction and loop diagrams in Tab. 2.2 generally include infinities. For large momentum transfers q in contact interactions, higher order terms become indistinguishable from the LO contact interaction due to the shorter duration of the dynamics, in accordance with the uncertainty principle $\Delta E \Delta t \gtrsim \frac{\hbar}{2}$. Consequently, infinitely many higher order terms would have to be considered as $q \rightarrow \infty$. To regularize the theory, a cutoff-momentum Λ is introduced that defines an upper bound to the momentum transfer. Since $\Delta p \Delta x \gtrsim \frac{\hbar}{2}$, this cutoff defines the minimum size of structures that can be resolved with the EFT and may therefore alternatively be called the resolution scale. This introduces a new issue: Physical results should not depend on the artificially defined resolution. To get rid of this dependence, the EFT is renormalized by making the coupling parameters dependent on the resolution scale Λ . The coupling constants become “running couplings”. The differential equation that can be derived for Λ are called renormalization group (RG) equations and in general can be written as [87]

$$\Lambda \frac{dC_i}{d\Lambda}(\Lambda) = \beta(C_i(\Lambda)), \quad (2.3)$$

with the coupling parameter C_i and a function β that defines the running of the coupling.

2.1.3 In-medium similarity renormalization group

The idea of the similarity renormalization group (SRG) is to decouple low-energy from high-energy states while renormalizing all operators and keeping low-energy observables unchanged to improve the convergence of many-body calculations [6, 88]. This is achieved by applying a unitary transformation $U(s)$ to all operators such that [6]

$$H(s) = U(s) H U^\dagger(s) \equiv T_{\text{rel}} + V_{\text{NN}}(s) + V_{\text{3N}}(s), \quad (2.4)$$

where T_{rel} is the relative kinetic energy of the system and $V_{\text{NN}}(s)$ and $V_{\text{3N}}(s)$ are the transformed two-body and three-body potentials constructed from the respective diagrams in Tab. 2.2 that now depend on a flow parameter s . The derivative of Eq. (2.4) with respect to s is the flow equation [6]

$$\frac{dH(s)}{ds} = \frac{dV_{\text{NN}}(s)}{ds} + \frac{dV_{\text{3N}}(s)}{ds} = [\eta(s), H(s)], \quad \eta(s) = \frac{dU(s)}{ds} U^\dagger(s) = -\eta^\dagger(s). \quad (2.5)$$

with the commutator $[a, b] = ab - ba$. Here, n -body interactions only enter the n -body part of the flow equation. In this free-space SRG approach, the evolution of the NN interactions with s is completely determined by the free-space solution of Eq. (2.5) and remains valid for all nuclei [89]. However, the computational cost of this method increases exponentially with the mass number A , as the Hamiltonian needs to be represented in a Jacobi or single-particle basis [90].

The in-medium similarity renormalization group (IMSRG) solves this problem by normal-ordering the Hamiltonian with respect to a reference state $|\Phi\rangle$. The transformed Hamiltonian is then usually written as [90, 91]

$$H(s) = E(s) + f(s) + \Gamma(s) + W(s) + \mathcal{O}(4\text{-body operators}), \quad (2.6)$$

where $E(s) = \langle \Phi | H(s) | \Phi \rangle$, and $f(s)$, $\Gamma(s)$ and $W(s)$ are the normal-ordered one- to three-body contributions. The normal-ordered Hamiltonian describes the residual interaction beyond the expectation value of the trivial reference state. Here, free-space 3N interactions already enter the zero-body in-medium contribution $E(s)$ [91]. Solving the flow equation, brings $H(s \rightarrow \infty)$ into a block-diagonal form such that the eigen energy $E(s \rightarrow \infty)$ of $|\Phi\rangle$ becomes the correlated energy that includes the admixture of all considered particle-hole excitation states.

The mean-square nuclear charge radius of a system in the reference state is derived by determining the expectation value of the proton radius operator [91, 92]

$$R_p^2 = \frac{1}{Z} \sum_{i=1}^A (\mathbf{r}_i - \mathbf{R})^2 P_p(i), \quad \mathbf{R} = \frac{1}{A} \sum_{i=1}^A \mathbf{r}_i, \quad P_p(i) = \begin{cases} 1 & \text{if proton} \\ 0 & \text{else} \end{cases} \quad (2.7)$$

where \mathbf{R} is the center-of-mass coordinate of the nucleus, $P_p(i)$ is a projection operator for the i th nucleon, Z is the number of protons and A the number of nucleons. The charge radius is determined by considering additional corrections through [93]

$$R_C = \sqrt{\langle R_p^2 \rangle + \langle r_p^2 \rangle + \frac{N}{Z} \langle r_n^2 \rangle + \frac{3\hbar^2}{4m_p^2 c^2} + \langle r^2 \rangle_{so}}, \quad (2.8)$$

where $\langle r_p^2 \rangle = 0.8770 \text{ fm}^2$ and $\langle r_n^2 \rangle = -0.1149 \text{ fm}^2$ are the proton and neutron mean-square charge radii, $3\hbar^2/(4m_p^2 c^2) = 0.033 \text{ fm}^2$ is the relativistic Darwin-Foldy correction, $\langle r^2 \rangle_{so}$ is a spin-orbit correction and N is the number of neutrons. The proton radius is the older larger value that was questioned by the proton radius puzzle [94, 95] and got replaced by a smaller value in the latest review of particle physics [79]. The spin-orbit correction depends on the nucleus and is especially relevant for halo nuclei [96]. The wavefunctions in position space required to compute R_C are linear combinations of perturbatively constructed natural orbitals. For details see [92].

2.2 Atomic structure

In order to gain information about the nuclear structure of an atom via laser spectroscopy, a precise quantitative description of the atomic structure is required. In the following sections, the properties of $^{13}\text{C}^{4+}$ and the atomic structure theory required for the analysis presented in this work are described. All energy values in the following sections are given either as energies in eV, vacuum wavelengths in nm or transition frequencies in MHz or GHz, depending on their order of magnitude.

2.2.1 Atomic structure of C^{4+}

In helium-like systems, the nucleus and two negatively charged electrons form a three-body system. The two electrons, being spin- $1/2$ particles, are coupled to either have a total spin of $S = 0$ (singlet) or $S = 1$ (triplet). Since radiative transitions between these two couplings are strongly suppressed due to their insensitivity to the electric component of electro-magnetic waves, they can be viewed as two separate systems. The level scheme of helium-like systems in general and C^{4+} in particular is shown in Fig. 2.1.

In C^{4+} , the transition into the first excited state $1s2p\ ^1\text{P}_1$ with a transition energy of $E = 308 \text{ eV}$ corresponding to a transition wavelength of $\lambda = 4.0 \text{ nm}$ [97] and a natural linewidth of $\Delta\nu = 141 \text{ GHz}$ is far out of reach for high-precision laser spectroscopy. However, as a consequence of the Pauli exclusion principle, the lowest-lying triplet state is already the

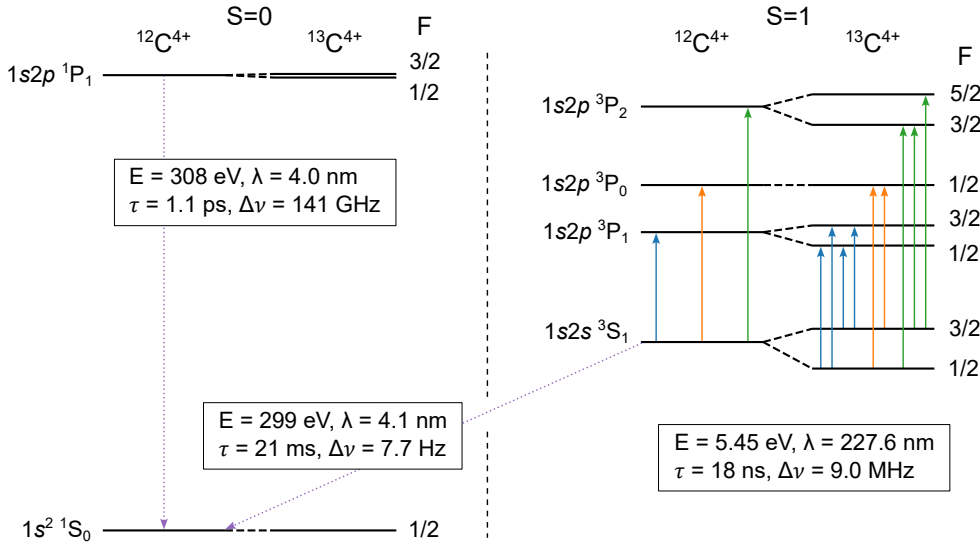


Figure 2.1: Level scheme of the lowest states in helium-like $^{12,13}\text{C}^{4+}$ relevant for this work. The hyperfine structure splittings of the triplet states relative to each other are to scale based on the results of this work. The fine-structure energies are not to scale. Energies E , corresponding transition wavelength λ , mean lifetimes τ and natural transition linewidth $\Delta\nu$ are indicated.

$1s2s\ 3S_1$ state. This metastable state lies 299 eV (4.1 nm) above the ground state of the singlet system, into which it decays via a magnetic dipole transition with a mean lifetime of $\tau = 21$ ms [97]. This high-lying metastable state enables addressing C^{4+} with optical frequencies by exciting the electron from the $2s$ shell into the $2p$ shell of the triplet system. The wavelengths of the $1s2s\ 3S_1 \rightarrow 1s2p\ 3P_{0,1,2}$ transitions are in the UV-regime between 227.2 nm and 227.9 nm and have natural linewidths of only 9.0 MHz [97].

In $^{13}\text{C}^{4+}$, the electronic states split into additional states due to the magnetic interaction of the electrons with the spin- $1/2$ nucleus. Therefore, the three available transitions in $^{12}\text{C}^{4+}$ become nine transitions in $^{13}\text{C}^{4+}$. The splittings of the transitions are of the order of 50 GHz. Since it is the goal of this work to extract the difference of the nuclear charge radii of ^{12}C and ^{13}C , the additional energy shift due to the hyperfine structure in $^{13}\text{C}^{4+}$ needs to be determined to extract the shift caused purely by the electrostatic change of the potential inside the nucleus.

2.2.2 Hyperfine structure

In this work, hyperfine structure (HFS) refers to the splitting of atomic energy levels arising due to the electro-magnetic moments of the nucleus of dipole or higher order. The derivation of the hyperfine structure formulas is based on the formulas and notations used in [98–100]. The interaction Hamiltonian of the hyperfine structure can be written as [98–100]

$$H_{\text{HFS}} = \sum_{k \geq 1} \left[\mathbf{M}^{(k)} \otimes \mathbf{T}^{(k)} \right]_0^{(0)} \equiv \sum_{k \geq 1} \mathbf{M}^{(k)} \cdot \mathbf{T}^{(k)} \equiv \sum_{k \geq 1} \sum_{\lambda=-k}^k (-1)^\lambda M_{-\lambda}^{(k)} \cdot T_\lambda^{(k)}, \quad (2.9)$$

where $\mathbf{M}^{(k)}$ and $\mathbf{T}^{(k)}$ are irreducible tensor operators of rank k in the nuclear and electronic space, respectively. Let the states of the atomic system be denoted by the state vector $|\alpha I, \gamma J; FM\rangle$ where I , J and F are the nuclear spin, the total electronic angular momentum and the total angular momentum of the complete system, respectively. α as well as γ are tuples of the remaining quantum numbers required to uniquely identify the quantum states. By applying the Wigner-Eckart theorem multiple times, the geometrical part of H_{HFS} can be calculated to separate the nuclear from the electronic system. Using Eq. (C.1) and (2.105) from [98], results in

$$\begin{aligned} & \langle \alpha I, \gamma J; Fm | H_{\text{HFS}} | \alpha' I', \gamma' J'; F'm' \rangle \\ &= \sum_{k \geq 1} (-1)^{F-m} \begin{pmatrix} F & 0 & F' \\ -m & 0 & m' \end{pmatrix} \langle \alpha I, \gamma J; F | \mathbf{M}^{(k)} \cdot \mathbf{T}^{(k)} | \alpha' I', \gamma' J'; F' \rangle \end{aligned} \quad (2.10)$$

$$= \sum_{k \geq 1} (-1)^{I'+J+F} \left\{ \begin{matrix} I & J & F \\ J' & I' & k \end{matrix} \right\} \langle \alpha I | \mathbf{M}^{(k)} | \alpha' I' \rangle \langle \gamma J | \mathbf{T}^{(k)} | \gamma' J' \rangle \delta_{FF'} \delta_{mm'}, \quad (2.11)$$

where $(::)$ and $\{::\}$ are the Wigner-3j and -6j symbols and reduced matrix elements are denoted by $\langle \cdot | | \cdot | | \cdot \rangle$. For the atomic systems treated in this work, the off-diagonal elements of $\mathbf{M}^{(k)}$ can be neglected such that $I = I'$. However, in $^{13}\text{C}^{4+}$, the off-diagonal elements of $\mathbf{T}^{(k)}$ give rise to hyperfine-induced mixing.

Due to the parity-conserving nature of the strong nuclear and the electromagnetic force which are, to very good approximation, the main contributors to the nuclear structure, the odd electric and the even magnetic moments in Eq. (2.11) vanish in the laboratory frame. Note that there is an ongoing effort to probe magnetic quadrupole moments in octupole-deformed nuclei in which the contribution of parity-violating forces such as the weak interaction but also possible “beyond-the Standard Model” forces are enhanced due to energetically close lying states with opposite parity and equal spin [101, 102].

In most measurements of electronic transitions, the multipole expansion can be limited to the magnetic dipole ($k = 1$) and electric quadrupole ($k = 2$) order due to experimental precision. In $^{13}\text{C}^{4+}$, the $k = 2$ term completely vanishes due to the rotational symmetry of the spin- $1/2$ nucleus. Defining the nuclear magnetic dipole and spectroscopic electric quadrupole moments as

$$\mu_I := \langle \alpha I (m_I = I) | M_0^{(1)} | \alpha II \rangle, \quad \frac{eQ}{2} := \langle \alpha II | M_0^{(2)} | \alpha II \rangle, \quad (2.12)$$

allows to express Eq. (2.11), again by using the Wigner-Eckart theorem, as

$$\begin{aligned}
& \langle \alpha I, \gamma J; Fm | H_{\text{HFS}}^{k \leq 2} | \alpha I, \gamma' J'; Fm \rangle \\
&= (-1)^{I+J+F} \begin{Bmatrix} I & J & F \\ J' & I & 1 \end{Bmatrix} \sqrt{\frac{(2I+1)(I+1)}{I}} \mu_I \langle \gamma J | \mathbf{T}^{(1)} | \gamma' J' \rangle \\
&+ (-1)^{I+J+F} \begin{Bmatrix} I & J & F \\ J' & I & 2 \end{Bmatrix} \sqrt{\frac{(2I+3)(I+1)}{I(2I-1)}} \frac{eQ}{2} \langle \gamma J | \mathbf{T}^{(2)} | \gamma' J' \rangle. \quad (2.13)
\end{aligned}$$

What remains to be specified in more detail are the matrix elements of the electronic tensor operators $\mathbf{T}^{(k)}$. If the off-diagonal elements can be neglected, Eq. (2.13) can be rewritten into a simpler expression. By defining the hyperfine structure constants [100]

$$A := \frac{\mu_I \langle \gamma J J | T_0^{(1)} | \gamma' J J \rangle}{IJ} = \frac{\mu_I B_e}{IJ} \quad (2.14)$$

$$B := 2eQ \langle \gamma J J | T_0^{(2)} | \gamma' J J \rangle = eQ \frac{\partial^2 V_e}{\partial z^2}, \quad (2.15)$$

where B_e and $\partial^2 V_e / \partial z^2$ are the expectation values of the magnetic flux density and the curvature of the electrostatic potential of the electrons at the nucleus, respectively. The eigenvalues of H_{HFS} are given by [100]

$$E_{\text{HFS}}^{k \leq 2} = A \frac{K}{2} + B \frac{\frac{3}{4}K(K+1) - I(I+1)J(J+1)}{2I(2I-1)J(2J-1)}, \quad (2.16)$$

$$K := F(F+1) - I(I+1) - J(J+1). \quad (2.17)$$

If the off-diagonal elements $\langle \gamma J | \mathbf{T}^{(k)} | \gamma' J' \rangle$ need to be considered, the complete Hamiltonian $H = H_0 + H_{\text{HFS}}$ needs to be diagonalized, *i.e.*, the eigenvalue equations [99]

$$E_{\gamma J}^F C_{\gamma J}^F = E_{\gamma J} C_{\gamma J}^F + \sum_{\substack{\gamma' J' \\ J' = F - I}}^{F+I} \langle \alpha I, \gamma J; Fm | H_{\text{HFS}} | \alpha I, \gamma' J'; Fm \rangle C_{\gamma' J'}^F \quad (2.18)$$

must be solved. Here, $E_{\gamma J}$ are the eigenvalues of the fine-structure Hamiltonian H_0 which is independent of the quantum number F and $C_{\gamma J}^F$ are the components of the eigenvectors. Equation (2.18) cannot be parameterized and fitted to spectroscopy data without using input from atomic theory. A list of the matrix elements of $\mathbf{T}^{(1)}$ of the $1s2p\,{}^3P_{0,1,2}$ and 1P_1 states in helium-like systems is given in [99]. The values for ${}^{13}\text{C}^{4+}$, used in this work, are listed in Tab. 2.3. For the calculations, Johnson *et al.* used relativistic configuration-interaction wave functions including contributions from Coulomb and Breit-Rabi interactions. The nuclear moments can be found, *e.g.*, in [70]. For ${}^{13}\text{C}$, a nuclear magnetic moment of $0.702369(4) \mu_N$ is specified.

Table 2.3: Values of the matrix elements $\langle \gamma J || \mathbf{T}^{(1)} || \gamma' J' \rangle \equiv \langle (2S + 1)J || \mathbf{T}^{(1)} || (2S' + 1)J' \rangle$ for the $1s2p\ ^3P_{0,1,2}$ and 1P_1 states in $^{13}\text{C}^{4+}$ taken from [99]. All values are given in units of $\frac{e^2}{4\pi\epsilon_0} \frac{1}{4\pi a_0^2} \frac{1}{m_p c} = 13\,074.70\, \text{MHz}$, where m_p is the proton mass and a_0 the Bohr radius.

$\mathbf{T}^{(1)}$	$ 30\rangle$	$ 31\rangle$	$ 32\rangle$	$ 11\rangle$
$\langle 30 $	0	2.8606	0	-2.0372
$\langle 31 $	2.8606	2.7045	3.2263	-3.6508
$\langle 32 $	0	3.2263	5.8064	4.6926
$\langle 11 $	-2.0372	-3.6508	4.6926	0.050184

2.2.3 Zeeman effect

For a given quantum number F , an external magnetic field shifts the otherwise degenerate energy levels $|Fm_F\rangle$. This shift can be considered by extending the Hamiltonian with the energy contribution of the magnetic dipole of the atom in an external magnetic field

$$H_{\text{Zeeman}} = -\mu \cdot \mathbf{B}. \quad (2.19)$$

The only external magnetic field that contributes to the measurements presented in this work is that of the earth. Since it is weak compared with the hyperfine structure splitting, it can be treated perturbatively. Its eigenvalues can be written as

$$E_{m_F} = -m_F g_F \mu_B B, \quad (2.20)$$

where g_F , μ_B and B are the Landé factor, the Bohr magneton and the absolute value of the magnetic flux density, respectively. The factor g_F in terms of the angular momentum quantum numbers S, L, J, I, F and the Landé factors $g_l = -1$, $g_s = -2.0023$ and $g_I = \mu_I/(\mu_N I)$ with the nuclear magneton μ_N and the nuclear spin I is then given by

$$g_F = g_J \frac{F(F+1) + J(J+1) - I(I+1)}{2F(F+1)} + g_I \frac{\mu_N}{\mu_B} \frac{F(F+1) - J(J+1) + I(I+1)}{2F(F+1)} \quad (2.21)$$

$$g_J = g_l \frac{J(J+1) + L(L+1) - S(S+1)}{2J(J+1)} + g_s \frac{J(J+1) - L(L+1) + S(S+1)}{2J(J+1)}. \quad (2.22)$$

It should be noted that Eq. (2.21) strictly only holds for LS -coupling and if there is no hyperfine-induced mixing. However, for the investigated transitions in $^{13}\text{C}^{4+}$, these assumptions are sufficiently fulfilled given the size of the Zeeman effect induced by the magnetic field of the earth, which can be roughly estimated from the size of the Bohr magneton 1.4 MHz/G and $B_{\text{earth}} \approx 0.5\text{ G}$ to be of the order of 1 MHz.

The energy shift of an atomic transition between two states $|Fm_F\rangle \rightarrow |F'm_{F'}\rangle$ is then given by

$$\Delta E_{m_F \rightarrow m_{F'}} = (m_F g_F - m_{F'} g_{F'}) \mu_B B, \quad (2.23)$$

so that for π transitions ($\Delta m_F := m_{F'} - m_F = 0$)

$$\Delta E_{m_F}^\pi = m_F (g_F - g_{F'}) \mu_B B \quad (2.24)$$

and for σ^\pm transitions ($\Delta m_F = \pm 1$)

$$\Delta E_{m_F}^\pm = \Delta E_{m_F}^\pi \mp g_{F'} \mu_B B. \quad (2.25)$$

In laser spectroscopy, transitions are driven by polarized laser light. In the rotating frame of the atom, linearly polarized light can drive π transitions and, depending on the quantization axis, also σ^\pm transitions, but only to the same proportion. Circularly polarized light on the other hand favors either σ^- or σ^+ transitions. Consequently, linearly polarized light leads to a symmetric splitting of the transition energies, whereas circularly light leads to a shift of the mean transition energy. Therefore, the Zeeman effect can cause a systematic shift in the determination of transition frequencies from fluorescence spectra. A detailed estimation of the Zeeman effect in $^{13}\text{C}^{4+}$ is provided in Sec. 5.2.3.

2.2.4 Finite nuclear-size effect

The Hamiltonian H_{HFS} defined in Eq. (2.9) only describes the energy of the electrons in the electromagnetic potential of the nucleus if they are outside of the nucleus. Since in the most cases, the nucleus is much smaller than the extent of the electronic wave functions, this approximation suffices. However, with sufficient precision or in large nuclei, the shift of the hyperfine-structure energies due to the nuclear volume becomes visible. This “finite-size” effect, which enters all orders of the electromagnetic multipole expansion, is also named the Breit-Rosenthal-Crawford-Schawlow effect [103, 104]. The latter being usually only used to designate the respective contribution to hyperfine-structure anomalies of the magnetic dipole order. The leading, electric monopole order is included in the fine-structure energies $E_{\gamma J}$. For a point-like nucleus, it is given by

$$\mathbf{M}^{(0)} \cdot \mathbf{T}^{(0)} = - \sum_i \frac{Ze^2}{4\pi\epsilon_0} \frac{1}{r_i}, \quad (2.26)$$

where Z is the nuclear charge number and r_i the distance between the i th electron and the nucleus. The finite-size effect is the deviation of the fine-structure energies from Eq. (2.26) due to the probability of the electrons to be located inside the nuclear volume. This can be utilized to extract the mean-square nuclear charge radius or differences thereof from atomic

energies, which is shown in the following. The Hamiltonian of the finite-size effect can be written straightforward as

$$H_{\text{fs}} = -\frac{e^2}{4\pi\epsilon_0} \sum_{j=1}^Z \sum_i \left(\frac{1}{|\mathbf{r}_i - \mathbf{r}_j|} - \frac{1}{r_i} \right), \quad (2.27)$$

where the second term removes the contribution that has already been included in the approximation of a point-like nucleus. Using the Laplace expansion

$$\frac{1}{|\mathbf{r}_i - \mathbf{r}_j|} = \sum_{l=0}^{\infty} \frac{4\pi}{2l+1} \sum_{m=-l}^l (-1)^m \frac{r_<^l}{r_>^{l+1}} Y_l^{-m}(\theta_i, \phi_i) Y_l^m(\theta_j, \phi_j), \quad (2.28)$$

with $r_< := \min(r_i, r_j)$, $r_> := \max(r_i, r_j)$ and the normalized spherical harmonic functions Y_l^m in lowest order ($l = 0$), taking only the monopole contribution into account, leads to the approximation

$$\begin{aligned} H_{\text{fs}} &\approx -\frac{e^2}{4\pi\epsilon_0} \sum_{j=1}^Z \sum_i \left(\frac{1}{r_i} \Theta(r_i - r_j) + \frac{1}{r_j} \Theta(r_j - r_i) - \frac{1}{r_i} \right) \\ &= -\frac{e^2}{4\pi\epsilon_0} \sum_{j=1}^Z \sum_i \left(\frac{1}{r_j} - \frac{1}{r_i} \right) \Theta(r_j - r_i), \end{aligned} \quad (2.29)$$

where Θ is the Heaviside function. To calculate the energy eigenvalues, it is sufficient to treat the positions of the indistinguishable protons using a probability density function

$$\begin{aligned} \rho(\mathbf{r}) &= \langle \alpha I | \frac{1}{Z} \sum_{j=1}^Z \delta(\mathbf{r} - \mathbf{r}_j) | \alpha I \rangle \\ &= \int \dots \int \frac{1}{Z} \sum_{j=1}^Z \delta(\mathbf{r} - \mathbf{r}_j) |\Psi_{\alpha I}(\mathbf{r}_1, \dots, \mathbf{r}_Z)|^2 d^3 r_1 \dots d^3 r_Z, \end{aligned} \quad (2.30)$$

where $\delta(\mathbf{r} - \mathbf{r}_j)$ is the Dirac delta distribution, so that for any operator $f(\mathbf{r}_j)$

$$\begin{aligned}
\langle \alpha I | \sum_{j=1}^Z f(\mathbf{r}_j) | \alpha I \rangle &= \int \langle \alpha I | \sum_{j=1}^Z f(\mathbf{r}) \delta(\mathbf{r} - \mathbf{r}_j) | \alpha I \rangle d^3 \mathbf{r} \\
&= Z \int f(\mathbf{r}) \left[\int \dots \int \frac{1}{Z} \sum_{j=1}^Z \delta(\mathbf{r} - \mathbf{r}_j) |\Psi_{\alpha I}(\mathbf{r}_1, \dots, \mathbf{r}_Z)|^2 d^3 \mathbf{r}_1 \dots d^3 \mathbf{r}_Z \right] d^3 \mathbf{r} \\
&= Z \int f(\mathbf{r}) \rho(\mathbf{r}) d^3 \mathbf{r}.
\end{aligned} \tag{2.31}$$

The eigenvalues of the Hamiltonian for the finite-size effect in an ion with charge Q are then

$$\begin{aligned}
E_{\text{fs}} &= \langle \alpha I, \gamma J | H_{\text{fs}} | \alpha I, \gamma J \rangle \\
&= \int \rho(\mathbf{r}) \left[-\frac{Ze^2}{4\pi\epsilon_0} \sum_{i=1}^{Z-Q} \int \dots \int_{r_i \leq r} |\Psi_{\gamma J}(\mathbf{r}_1, \dots, \mathbf{r}_{Z-Q})|^2 \left(\frac{1}{r} - \frac{1}{r_i} \right) d^3 \mathbf{r}_1 \dots d^3 \mathbf{r}_{Z-Q} \right] d^3 \mathbf{r}.
\end{aligned} \tag{2.32}$$

Equation (2.32) is the starting point of the derivation of the finite-size contribution to the isotope shift of atomic transitions which was introduced originally by E. C. Seltzer [105] and is also referenced in [100]. There, also the electronic wave functions are written as a probability density function. To transform Eq. (2.32) into the differential form, the probability density or wave functions can simply be replaced by differences of these functions.

The expression in the square brackets, in the following named $g(\mathbf{r})$, depends only on the electronic wave functions and is independent of the proton density ρ . Therefore, Eq. (2.32) may be written as [105]

$$E_{\text{fs}} = \int \rho(\mathbf{r}) g(\mathbf{r}) d^3 \mathbf{r} \tag{2.33}$$

$$= \int_0^\infty \rho_r(r) F_{\gamma J} \left[r^2 + \frac{C_2}{C_1} r^4 + \frac{C_3}{C_1} r^6 + \mathcal{O}(r^8) \right] dr \tag{2.34}$$

$$= F_{\gamma J} \left[\langle r^2 \rangle + \frac{C_2}{C_1} \langle r^4 \rangle + \frac{C_3}{C_1} \langle r^6 \rangle + \mathcal{O}(\langle r^8 \rangle) \right] = F_{\gamma J} \Lambda_{\alpha I}, \tag{2.35}$$

where in Eq. (2.34), a spherically symmetric nuclear charge distribution ρ_r was assumed. Note that odd radial moments vanish due to the same argument given in Sec. 2.2.2 why the odd electric multipole moments in the hyperfine structure Hamiltonian vanish. The numbers C_k are called the Seltzer coefficients [105]. An explicit expression of $F_{\gamma J}$ is given below in Sec. 2.2.5, Eq. (2.43). The contribution of the finite-size effect to the difference of a transition energy between two isotopes A and A' can be expressed by replacing $F_{\gamma J}$ with $F_{\gamma J \rightarrow \gamma' J'} = F_{\gamma' J'} - F_{\gamma J}$ and $\langle r^{2k} \rangle$ with $\delta \langle r^{2k} \rangle^{AA'} = \langle r^{2k} \rangle^{A'} - \langle r^{2k} \rangle^A$ in Eq. (2.35). Hence, the moments of the nuclear charge distribution and the differences thereof can be extracted from electronic transition

frequencies if the energy eigenvalues of a hypothetical point-like nucleus and $F_{\gamma J \rightarrow \gamma' J'}$ can be calculated to sufficient precision.

It should be noted that in addition to the Breit-Rosenthal effect, also a distribution of the magnetization inside the nuclear volume leads to a shift of the hyperfine structure energies. This effect is called the Bohr-Weisskopf effect [106] and is usually also used in connection with hyperfine-structure anomalies. It plays a particular important role in highly-charged heavy ions such as hydrogen- or lithium-like Bi where the valence electron has a large overlap with the nucleus so that the energies significantly deviate from Eq. (2.9). In the example of Bi, the two finite-size effects are unwanted contributions to the atomic energy levels that significantly increase the difficulty of testing bound-state QED calculations [107, 108].

2.2.5 Nonrelativistic QED in helium-like systems

Nonrelativistic quantum electrodynamics (NRQED) calculations can be used to determine the electronic energy levels in helium-like systems and the electronic contribution to the isotope shift to very high precision [100, 109, 110]. Improved NRQED calculations have been carried out by Yerokhin *et al.* for C^{4+} [65] and are used in this work to determine the differential mean-square nuclear charge radius $\delta\langle r^2 \rangle^{12,13}$ between ^{12}C and ^{13}C . In the following, the theory used for the NRQED calculations is described mainly based on the conventions used in [110]. The nonrelativistic Hamiltonian of a multi-electron atom with a point-like nucleus is given by [100, 110]

$$H^{(2)} = \frac{\mathbf{P}^2}{2M} + \sum_i \frac{\mathbf{p}_i^2}{2m} + \frac{e^2}{4\pi\epsilon_0} \left(\sum_{i < j} \frac{1}{|\mathbf{r}_i - \mathbf{r}_j|} - \sum_i \frac{Z}{|\mathbf{r}_i - \mathbf{R}|} \right), \quad (2.36)$$

where \mathbf{P} is the total momentum of the nucleus, M the mass of the nucleus, \mathbf{p}_i the momenta of the electrons, m the electron mass, \mathbf{r}_i the positions of the electrons and \mathbf{R} the position of the nucleus. By using that the sum of all momenta vanishes in the rest-frame of the atom, Eq. (2.36) can be rewritten into

$$H^{(2)} = \sum_i \frac{\mathbf{p}_i^2}{2\mu} + \sum_{i < j} \frac{\mathbf{p}_i \cdot \mathbf{p}_j}{M} + \frac{e^2}{4\pi\epsilon_0} \left(\sum_{i < j} \frac{1}{|\mathbf{r}_i - \mathbf{r}_j|} - \sum_i \frac{Z}{r_i} \right), \quad (2.37)$$

where $\mu = mM/(m + M)$ is the reduced mass and r_i are the radial distances of the electrons to the center of gravity. It is numerically advantageous to use dimensionless units [100]. Redefining $\mathbf{p}_i \rightarrow \mu c \alpha \tilde{\mathbf{p}}_i$, $\mathbf{r}_i \rightarrow \hbar \tilde{\mathbf{r}}_i / (\mu c \alpha)$ and $H^{(2)} \rightarrow c^2 \tilde{H}^{(2)}$ yields the Hamiltonian specified in [110]

$$\frac{\tilde{H}^{(2)}}{\mu\alpha^2} = H_{\infty}^{(2)} + \frac{\mu}{m} H_{\text{rec}}^{(2)} = \left[\sum_i \left(\frac{\tilde{\mathbf{p}}_i^2}{2} - \frac{Z}{\tilde{r}_i} \right) + \sum_{i < j} \frac{1}{|\tilde{\mathbf{r}}_i - \tilde{\mathbf{r}}_j|} \right] + \frac{\mu}{m} \left[\frac{m}{M} \sum_{i < j} \tilde{\mathbf{p}}_i \cdot \tilde{\mathbf{p}}_j \right]. \quad (2.38)$$

The first step to the solution of this eigenvalue problem for helium-like systems is to find (eigen-) wave functions $\Psi(\mathbf{r}_1, \mathbf{r}_2)$ and the eigenvalues of $H_{\infty}^{(2)}$, as described in [111]. In short, the energy of a reference state, which is an eigenvalue of $H_{\infty}^{(2)}$, is minimized by varying the parameters of the wave functions that span the basis set. The set of wave functions used dates back to E. A. Hylleraas [112] and explicitly includes correlations between the two electrons. The optimization technique was first implemented to sufficient precision by V. I. Korobov [113, 114].

With the wave functions of $H_{\infty}^{(2)}$ constructed, all additional energy contributions are treated as perturbations. The corrections arising from quantum electrodynamics are represented by a power series in the fine-structure constant α such that energy eigenvalues E can be written as [110]

$$E = m\alpha^2 \mathcal{E}^{(2)} + m\alpha^4 \mathcal{E}^{(4)} + m\alpha^5 \mathcal{E}^{(5)} + m\alpha^6 \mathcal{E}^{(6)} + m\alpha^7 \mathcal{E}^{(7)} + \mathcal{O}(m\alpha^8). \quad (2.39)$$

where the first corrections enter at order $m\alpha^4$. This expansion does not strictly include only powers of natural numbers, but also includes terms which depend on $\ln \alpha$. The contribution of the recoil, also called mass-polarization term $H_{\text{rec}}^{(2)}$ and relativistic corrections are considered as part of a power series of $\mathcal{E}^{(n)}$ in m/M

$$\mathcal{E}^{(n)} = \mathcal{E}_{\infty}^{(n)} + \mathcal{E}_M^{(n)} + \mathcal{E}_{M^2}^{(n)} + \mathcal{O}(M^3). \quad (2.40)$$

Here, $\mathcal{E}_{\infty}^{(2)}$ directly corresponds to the eigenvalue of $H_{\infty}^{(2)}$. If calculating isotope shifts, the first order recoil correction $\mathcal{E}_M^{(2)}$ can be identified as the sum of normal and specific mass shift [110]

$$\mathcal{E}_M^{(2)} = -\frac{m}{M} \mathcal{E}_{\infty}^{(2)} + \left(\frac{\mu}{m} \right)^2 \langle H_{\text{rec}}^{(2)} \rangle \quad (2.41)$$

Taking the difference of Eq. (2.41) for two nuclei with mass numbers A and A' and reversing the coordinate transformations yields the usual formula for the mass shift

$$\begin{aligned}
h\nu^{A'} - h\nu^A &= mc^2\alpha^2(\mathcal{E}_{M_{A'}}^{(2)} - \mathcal{E}_{M_A}^{(2)}) \\
&= \frac{mc^2\alpha^2}{\tilde{\mu}^{A,A'}} \left(m\mathcal{E}_{\infty}^{(2)} + \mu \frac{\mu}{m} \left\langle \sum_{i < j} \tilde{\mathbf{p}}_i \cdot \tilde{\mathbf{p}}_j \right\rangle \right) \\
&= \frac{1}{\tilde{\mu}^{A,A'}} (K_{\text{NMS}} + K_{\text{SMS}}) = \frac{K}{\tilde{\mu}^{A,A'}} \tag{2.42}
\end{aligned}$$

where $\tilde{\mu}^{A,A'} = M_A M_{A'} / (M_{A'} - M_A)$ and $K_{\text{NMS/SMS}}$ are the normal and specific mass shift constants. The mass shift used in this work not only includes the $\mathcal{E}_M^{(2)}$ term, but all mass-dependent terms up to order $m\alpha^6$. The fine and hyperfine structure splittings contribute as relativistic corrections in $\mathcal{E}^{(4)}$. The finite-size effect to the lowest order depends on the mean-square nuclear charge radius as specified in Eq. (2.35). Higher orders can be neglected for light nuclei such as C. The field-shift constant in SI-units is given by

$$F_{\gamma J} = \frac{Ze^2}{6\varepsilon_0} \sum_i \int \dots \int |\Psi_{\gamma J}(\mathbf{r}_i = \mathbf{0})|^2 d^3\mathbf{r}_{j \neq i}, \tag{2.43}$$

where the integral term corresponds to the probability density of the i th electron to be located at the nucleus. The energy of a transition under the assumption of a point-like nucleus $E_{i \rightarrow f}^{\text{point-like}}$ calculated with Eq. (2.39) together with the field-shift constant determined from Eq. (2.43) can be used to extract the mean-square nuclear charge radius $\langle r^2 \rangle$ from measurements of an atomic transition energy $E_{i \rightarrow f}^{\text{exp}}$ with

$$\langle r^2 \rangle = \frac{E_{i \rightarrow f}^{\text{exp}} - E_{i \rightarrow f}^{\text{point-like}}}{F_{i \rightarrow f}}. \tag{2.44}$$

Through this approach, the charge radius of ^{12}C was determined using only laser spectroscopy and atomic structure calculations of the $1s2s\ 3\text{S}_1 \rightarrow 1s2p\ 3\text{P}_{0,1,2}$ transitions in $^{12}\text{C}^{4+}$ [63, 64]. This was the first time, the “all-optical” approach was used in a helium-like ion in the optical-wavelength range where MHz-precision can be reached. However, currently, the best available atomic structure calculations have “only” a precision of 0.1 to 1 GHz for absolute transition frequencies [63, 64]. In this work, the isotope shifts of the same transitions between ^{12}C and ^{13}C are determined. In this differential approach, the atomic structure calculations are more precise, since all mass-independent contributions to the power series in Eq. (2.40) cancel. While for absolute energies, the calculations up to order $m\alpha^7$ were not sufficient to reach the experimental precision, for the isotope shift, an expansion up to order $m\alpha^6$ suffices to surpass it.

2.2.6 Isotope shift

In this work, the isotope shift refers to the difference of a transition energy, or its corresponding frequency, between two isotopes. The isotope shift between two isotopes with mass number A and A' can be defined as

$$\delta E_{i \rightarrow f}^{AA'} = E_{i \rightarrow f}^{A'} - E_{i \rightarrow f}^A = h(\nu_{i \rightarrow f}^{A'} - \nu_{i \rightarrow f}^A). \quad (2.45)$$

With Eq. (2.42) and (2.44), the usual formula for the isotope shift of a transition is recovered

$$h\delta\nu_{i \rightarrow f}^{AA'} = \frac{K_{i \rightarrow f}}{\tilde{\mu}^{A,A'}} + F_{i \rightarrow f} \delta\langle r^2 \rangle^{AA'}. \quad (2.46)$$

The differential mean-square nuclear charge radius between the two isotopes can be calculated by modifying Eq. (2.46) into

$$\delta\langle r^2 \rangle^{AA'} = \frac{\delta E_{i \rightarrow f}^{\text{exp}} - \delta E_{i \rightarrow f}^{\text{point-like}}}{F_{i \rightarrow f}} = \frac{h\delta\nu_{i \rightarrow f}^{AA'} - K_{i \rightarrow f}/\tilde{\mu}^{A,A'}}{F_{i \rightarrow f}}, \quad (2.47)$$

where $\delta\nu_{i \rightarrow f}^{AA'}$ corresponds to an experimentally determined isotope-shift frequency and $K_{i \rightarrow f}/\tilde{\mu}^{A,A'}$ to the mass-shift contribution determined by theory as described in Sec. 2.2.5. Note that for the purpose of extracting $\delta\langle r^2 \rangle^{AA'}$, in Eq. (2.45), the $\nu_{i \rightarrow f}$ can be arbitrary linear combinations of transition energies. With this, the precision of $\delta\langle r^2 \rangle^{AA'}$ can be increased when more than one transition is accessible in the experiment. In case of the transitions in C^{4+} measured within this work and [63, 64], the best precision is achieved by defining $\nu_{i \rightarrow f}$ as the center of gravity of all $1s2s\,{}^3\text{S}_1 \rightarrow 1s2p\,{}^3\text{P}_{0,1,2}$ transitions

$$\nu_{i \rightarrow f} = \sum_{t \in {}^3\text{S}_1 \rightarrow {}^3\text{P}_{J'}} w_t \nu_t, \quad w_t = \frac{(2F+1)(2F'+1)(2J'+1)}{3(2I+1)(2J+1)} \begin{Bmatrix} J' & J & 1 \\ F & F' & I \end{Bmatrix}^2, \quad (2.48)$$

where w_t is the relative line strength of the transition $|JF\rangle \rightarrow |J'F'\rangle$ between two hyperfine-structure states if there was no hyperfine-induced mixing. In case of ${}^{12}\text{C}$, with a nuclear spin of zero, $F \equiv J$ and $F' \equiv J'$. The atomic structure calculations yield the energies of the states and not the transition frequencies. In this case, Eq. (2.48) can be rearranged into [110]

$$E_{i \rightarrow f} = E({}^3\text{P}) - E({}^3\text{S}), \quad E({}^{2S+1}L) = \sum_{J,F} \frac{(2F+1)E({}^{2S+1}L_{J,F})}{(2I+1)(2S+1)(2L+1)}. \quad (2.49)$$

Explicit expressions of Eq. (2.48) and (2.49) are given Tab. 2.4.

Table 2.4: Formulas for the center-of-gravity transition frequencies $\bar{\nu}_{J'}$ of the $1s2s\ ^3S_1, \rightarrow 1s2p\ ^3P_{0,1,2}$ transitions in $^{12,13}C^{4+}$ as functions of the individual transition frequencies $\nu_{J'}(F, F')$ and center-of-gravity level energies \bar{E}_J and $\bar{E}'_{J'}$ of the involved states as functions of the individual level energies $E_J(F)$ and $E'_{J'}(F')$ of the hyperfine-structure states.

Transition	Center-of-gravity transition frequency
$^3S_1 \rightarrow ^3P_0$	$\bar{\nu}_0 := \frac{1}{3}\nu_0(\frac{1}{2}, \frac{1}{2}) + \frac{2}{3}\nu_0(\frac{3}{2}, \frac{1}{2})$
$^3S_1 \rightarrow ^3P_1$	$\bar{\nu}_1 := \frac{2}{9}\nu_1(\frac{1}{2}, \frac{1}{2}) + \frac{1}{9}\nu_1(\frac{1}{2}, \frac{3}{2}) + \frac{1}{9}\nu_1(\frac{3}{2}, \frac{1}{2}) + \frac{5}{9}\nu_1(\frac{3}{2}, \frac{3}{2})$
$^3S_1 \rightarrow ^3P_2$	$\bar{\nu}_2 := \frac{1}{3}\nu_2(\frac{1}{2}, \frac{3}{2}) + \frac{1}{15}\nu_2(\frac{3}{2}, \frac{3}{2}) + \frac{3}{5}\nu_2(\frac{3}{2}, \frac{5}{2})$
$^3S \rightarrow ^3P$	$\bar{\nu} := \frac{1}{9}\bar{\nu}_0 + \frac{1}{3}\bar{\nu}_1 + \frac{5}{9}\bar{\nu}_2$
Energy level	Center-of-gravity level energy
3S_1	$\bar{E}_1 := \frac{1}{3}E_1(\frac{1}{2}) + \frac{2}{3}E_1(\frac{3}{2})$
3P_0	$\bar{E}'_0 := E'_0(\frac{1}{2})$
3P_1	$\bar{E}'_1 := \frac{1}{3}E'_1(\frac{1}{2}) + \frac{2}{3}E'_1(\frac{3}{2})$
3P_2	$\bar{E}'_2 := \frac{2}{5}E'_2(\frac{3}{2}) + \frac{3}{5}E'_2(\frac{5}{2})$
3P	$\bar{E}' := \frac{1}{9}\bar{E}'_0 + \frac{1}{3}\bar{E}'_1 + \frac{5}{9}\bar{E}'_2$

2.3 Fluorescence spectroscopy

In an atomic system, the energy difference E between two electronic states is directly related to a transition frequency ν_0 through the Planck constant $E = h\nu_0$. If the energy, or frequency ν , of a photon matches that of the transition, an electron in the initial state can be transferred into the final state by absorbing the photon. From the energetically upper state, the electron can spontaneously decay to a lower state by emitting a photon into a random direction whose distribution is given by the properties of the two states. By systematically changing the frequency of the incoming photons and counting the spontaneously emitted photons, the transition frequency between the two states can be extracted from the resulting resonance spectrum. This method is called fluorescence spectroscopy.

To define the frequency of the incident photon in the optical regime precisely enough to extract nuclear structure information, using a laser is inevitable. It should be noted, however, that nuclear structure information from frequency measurements has been obtained since the 1920s. With the invention of the frequency comb, frequency measurements with 10^{-18} relative precision in the optical regime became possible [115–118]. However, even with a hypothetical arbitrarily precisely defined laser frequency, the precision of the extracted transition frequency will be limited due to the Doppler effect caused by the thermal motion of the probed atoms, which causes a broadening of the resonance spectrum. This is called Doppler-broadening. Different approaches can be pursued to overcome this limitation. Within this work, collinear

laser spectroscopy is used to compress the Doppler width of $^{13}\text{C}^{4+}$ ions through electrostatic acceleration.

2.3.1 Resonance lineshapes

To extract transition frequencies from fluorescence spectra, the frequency position of a resonance signal, caused by exciting an atom from a lower state into an upper state, needs to be determined. In collinear laser spectroscopy, the resonance signal of a single electronic transition is usually given by a Voigt profile, which is a convolution of a Lorentz and a Gauss profile [119]

$$V(\nu, \Delta\nu_L, \sigma) = \int_{-\infty}^{\infty} L(\nu - \nu', \Delta\nu_L) G(\nu', \sigma) d\nu' \quad (2.50)$$

$$L(\nu, \Delta\nu_L) = \frac{1}{2\pi} \frac{\Gamma}{\nu^2 + \frac{1}{4}\Delta\nu_L^2} \quad (2.51)$$

$$G(\nu, \sigma) = \frac{1}{\sqrt{2\pi}\sigma} \exp\left(-\frac{\nu^2}{2\sigma^2}\right), \quad (2.52)$$

where $\Delta\nu_L$ is the full width at half maximum (FWHM) of the Lorentzian and σ is the standard deviation of the Gaussian. The FWHM of the Voigt profile within 0.02 % accuracy is given by [120]

$$\Delta\nu_V \approx 0.5346\Delta\nu_L + \sqrt{0.2166\Delta\nu_L^2 + 8\ln(2)\sigma^2}. \quad (2.53)$$

The Gaussian part of the Voigt profile originates from the Doppler-shifted laser frequencies due to the motion of the atoms or ions and thus describes their velocity distribution. This is called Doppler-broadening. While the Gaussian shape naturally occurs for particle ensembles in thermal equilibrium, in collinear laser spectroscopy, where the velocity distribution of the ions is compressed along the axis of acceleration, the Gaussian shape most commonly stems from statistical fluctuations of the voltage potentials. Depending on the ion beam properties, the Gauss function can be replaced by any other velocity distribution to define more specialized lineshapes.

The Lorentzian part of the Voigt originates from the finite lifetime of the excited state τ involved in the laser-driven transition. The minimum width of the Lorentzian corresponds to the natural linewidth of the transition and is related to the lifetime through

$$\Delta\nu_{L,\min} = \frac{1}{2\pi\tau}. \quad (2.54)$$

However, it can be broadened by effects that are homogeneous with respect to the ion velocities. The most important effects here are collision and saturation broadening. Both effects can be imagined as a decrease of the mean lifetime of the excited state. In the former,

collisions with other particles depopulate the excited state while in the latter, stimulated emission increases the rate of the population transfer from the upper to the lower state. Here the Lorentz width increases with the laser intensity I according to

$$\Delta\nu_{L,\text{sat}} = \Delta\nu_L \sqrt{1 + \frac{I}{I_0}}, \quad (2.55)$$

where I_0 is the saturation intensity. Typical values for the saturation in measurements with C^{4+} are estimated in Sec. 5.2.3. Similar to the Gaussian, also the Lorentzian lineshape needs to be replaced in some cases. For example, if the interaction time of an ion with the laser T is short compared with τ , which can be especially relevant for slow transitions of highly-charged light ions, the lineshape becomes a squared sinc function [119]

$$S(\nu, T) = \frac{1}{\pi^2 T} \frac{\sin^2(\pi\nu T)}{\nu^2}, \quad (2.56)$$

with an FWHM of the central peak of

$$\Delta\nu_S \approx \frac{5.6}{2\pi T}. \quad (2.57)$$

In the case of $^{13}\text{C}^{4+}$, the interaction time until the first fluorescence photons can be detected is 67 ns which is well above the mean lifetime of the excited states of 18 ns. Another example of an effect that causes a distorted Lorentz shape is quantum interference which is explained in Sec. 2.4.5.

2.3.2 Collinear laser spectroscopy

Collinear laser spectroscopy (CLS) has proven to be a valuable method to extract information about the nuclear structure of nuclei across the entire nuclear chart [11, 12]. In particular, nuclear charge radii and electro-magnetic moments of nuclei determined from CLS serve as important benchmark values for nuclear structure theory, as in [21, 121–125] for some recent examples. While CLS experiments at on-line facilities like CERN/ISOLDE, NSCL/FRIB, JYVL or ANL focus on the investigation of short-lived radioactive isotopes, off-line setups such as the one used within this work are specialized to achieve highest precision. Here, quasi-simultaneous collinear-anticollinear laser spectroscopy is used to determine the absolute electronic transition frequencies of the $1s2s\ ^3\text{S}_1 \rightarrow 1s2p\ ^3\text{P}_{0,1,2}$ transitions in $^{13}\text{C}^{4+}$. These can be used in combination with the results in $^{12}\text{C}^{4+}$ to extract the differential nuclear charge radius between the two isotopes in a nuclear-model independent way. Figure 2.2 depicts the principle setup of a collinear laser spectroscopy experiment.

Doppler compression In collinear laser spectroscopy, ions are electrostatically accelerated by a potential difference U between the ion source region and the laser-ion interaction region.

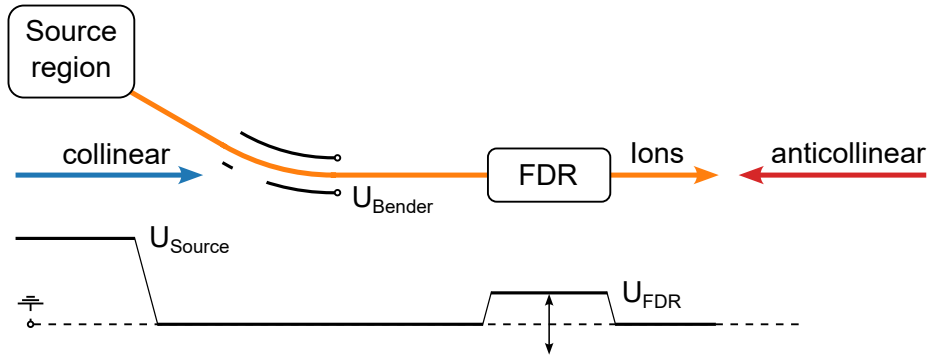


Figure 2.2: Upper row: The principle of collinear laser spectroscopy. Ions are produced on a high-voltage potential U_{Source} in the source region. After electrostatic acceleration, the ions are electrostatically bent (U_{Bender}) to be superposed with a collinear and/or an anticollinear laser beam. In the fluorescence detection region (FDR), the velocity of the ions is adjusted to scan the laser frequencies over the resonance signal by applying an additional voltage U_{FDR} and utilizing the Doppler effect. Lower row: The basic electrostatic potentials in collinear laser spectroscopy. The potential differences are not to scale.

The relativistic velocity component β in the direction of acceleration is given by

$$\beta = \sqrt{1 - \frac{1}{\left(\gamma_0 + \frac{qU}{mc^2}\right)^2}}, \quad \gamma = \frac{1}{\sqrt{1 - \beta^2}}, \quad \beta = \frac{v}{c}, \quad (2.58)$$

where c is the speed of light and γ_0 , q and m are the time-dilation factor of the initial velocity, the electric charge and the mass of the ion, respectively. Taking the derivative of Eq. (2.58) with respect to U shows that the velocity spread $\Delta\beta$ decreases with increasing velocity as the energy spread $q\Delta U$ stays constant

$$\Delta\beta = \frac{1}{\beta} \frac{q\Delta U}{\gamma mc^2}. \quad (2.59)$$

Hence, the Doppler broadening is strongly compressed and an acceleration voltage of a few 10 kV is sufficient to reduce it to the natural linewidth [126].

Collinear-anticollinear measurements For the moving ions, the laser frequency ν in the rest-frame of the accelerated ions is shifted from the laboratory frequency ν_{lab} by

$$\nu = \nu_{\text{lab}}\gamma(1 - \beta \cos \alpha), \quad (2.60)$$

where α is the angle between the laser and the ion beam in the laboratory frame. If the laser is aligned in collinear (c, $\alpha = 0$) or anticollinear (a, $\alpha = \pi$) direction, Eq. (2.60) simplifies to

$$\nu = \nu_{\text{lab}}\gamma(1 \mp \beta). \quad (2.61)$$

To achieve a sub-MHz precision, the kinetic ion energy needs to be known to a few meV which is impossible due to the limited knowledge of the exact ion source potential and additional contact potentials of the order of typically a few V. To circumvent this problem, a spectrum can be recorded simultaneously in collinear and anticollinear direction. By multiplying Eq. (2.61) of both cases with each other using the resonant laser frequencies $\nu_{c/a}$, the rest-frame transition frequency ν_0 can be readily obtained without knowing the ion velocity

$$\nu_0^2 = \nu_c \nu_a \gamma_c \gamma_a (1 - \beta_c)(1 + \beta_a) \stackrel{\beta_c = \beta_a}{=} \nu_c \nu_a, \quad (2.62)$$

where the last step indicates that it must be ensured to address ions of the same velocity in both cases/measurements.

Doppler tuning Due to the working principle of the laser that requires a fixed resonator size to maintain lasing at a single frequency, it is advantageous to stabilize the laser frequencies to fixed values and scan the acceleration voltage instead. This is called “Doppler tuning” and changes the velocity and, hence, the laser frequencies in the rest-frame of the ions. Since the laser frequencies cannot be set exactly to values where the resonances appear at the same scan voltage for both laser configurations, $\beta_c \neq \beta_a$ and thus, the last step in Eq. (2.62) does no longer hold. However, this error can be corrected if the difference $\Delta U := U_c - U_a$ between the two voltages at which the resonances appear is determined. Depending on the accuracy with which the laser frequencies were chosen, a linear correction suffices

$$\nu_0^2 = \nu_c \nu_a \left(1 - \frac{q\Delta U}{\beta \gamma m c^2} \right). \quad (2.63)$$

The sensitivity to β , *i.e.*, to the absolute voltage increases only slowly with an increasing voltage difference such that a few V difference between the resonance positions do not introduce any resolvable systematic shifts. An estimation of potential systematic errors due to an unknown absolute voltage is given in Sec. 5.2.3.

2.3.3 Photon recoil

The energy and the momentum of a photon are given by $E_\gamma = h\nu$ and $p_\gamma = h\nu/c$, respectively. When absorbing a photon, the atom gains its momentum so that nonrelativistically in the initial rest frame of the atom

$$p_{\text{atom}} = mv = h\nu/c = p_{\gamma} \quad (2.64)$$

Since this also changes the kinetic energy of the atom, the energy of the photon needs to be slightly higher than the transition energy $h\nu_0$ of the transition that gets excited. This extra energy can be derived straightforward

$$\begin{aligned} h\delta\nu_{\text{rec}} &:= h\nu - h\nu_0 = \frac{1}{2}mv^2 \\ \stackrel{(2.64)}{\Leftrightarrow} \quad \delta\nu_{\text{rec}} &= \frac{h\nu^2}{2mc^2} \\ \stackrel{(2.62)}{\Leftrightarrow} \quad \delta\nu_{\text{rec}} &= \frac{h\nu_c\nu_a}{2mc^2}. \end{aligned} \quad (2.65)$$

To fulfill momentum and energy conservation upon absorption of a photon, the small correction $\delta\nu_{\text{rec}}$ due to the photon recoil needs to be applied to Eq. (2.63), such that finally

$$\nu_0 = \sqrt{\nu_c\nu_a \left(1 - \frac{q\Delta U}{\beta\gamma mc^2} \right)} - \delta\nu_{\text{rec}}. \quad (2.66)$$

Therefore, the transition frequency determined with Eq. (2.66) directly corresponds to energies derived from atomic theory. While the momentum transfer of a single photon can be treated exactly with Eq. (2.66), repeated scattering of photons leads to systematic effects due to the stochastic nature of the process. Since spontaneous emission of photons is isotropic with respect to the laser beam axis, the atom on average accelerates in the propagation direction of the laser if multiple photon absorption and spontaneous emission cycles occur. The mean velocity gained per absorption is given by Eq. (2.64). Due to the Doppler effect, this also changes the resonant laboratory-frame laser frequency to good approximation by

$$\nu\beta \stackrel{(2.64)}{=} \frac{h\nu^2}{mc^2} \stackrel{(2.65)}{=} 2\delta\nu_{\text{rec}}. \quad (2.67)$$

Since the shift is positive for both collinear and anticollinear geometry, photon recoils can lead to a systematic shift in the transition frequency determination. Therefore, this effect was investigated with simulations of the laser-atom interactions described in Sec. 2.4.4 that are then used to estimate a systematic uncertainty in Sec. 5.2.3.

2.4 Laser-atom interactions

The interaction between a thermalized atom and one or more lasers can be described quantum mechanically using the Lindblad master equation. In the following, the derivation of the master equation is outlined. Additionally, a Monte-Carlo approach and the rate equations

are described. Solutions of the equations derived here are implemented in the *qspec* package, described in Sec. 3. For a more detailed derivation of the Lindblad master equation, see for example [127–129].

2.4.1 Hamiltonian of an atom in classical Laser fields

The complete Hamiltonian of an atom interacting with a laser may be written as

$$H = H_A + H_L + H_R + H_{AL} + H_{AR}, \quad (2.68)$$

where H_A describes the atom, H_L the laser field, H_R the thermal reservoir or vacuum and H_{AL} and H_{AR} the interaction of the atom with the laser field and the vacuum, respectively. This Hamiltonian which needs to be described in second quantization can be vastly simplified for the application of CLS.

The atom can be described by a set of internal states $|i\rangle$ and its kinetic energy. In the rest-frame of the atom the kinetic energy is zero. Neglecting photon recoils for now, the atomic system is given by

$$H_A = \sum_i \hbar \omega_i \hat{\sigma}_{ii}, \quad (2.69)$$

with the energy eigenvalues $\hbar \omega_i$ and the system operator $\hat{\sigma}_{ij} = |i\rangle \langle j|$. The thermal reservoir is assumed to be an energy continuum of photons in thermal equilibrium. Hence, it is large so that the interaction with the atom will effectively not change its state and thus, H_R can be neglected. In the dipole approximation, the interaction of the atom with the reservoir can be written as [128]

$$H_{AR} = \hbar \sum_{\substack{i,j \\ i \neq j}} \hat{\sigma}_{ij} \sum_{\mathcal{H}_R} \alpha_R(\omega) \hat{b}_{\mathbf{k},q} e^{-i\omega t} + \alpha_R^*(\omega) \hat{b}_{\mathbf{k},q}^\dagger e^{i\omega t} d^3 \mathbf{k}, \quad (2.70)$$

where $\alpha_R(\omega)$ is the coupling strength between the atom and the reservoir, and $\hat{b}_{\mathbf{k},q}^\dagger$ is a reservoir excitation operator that creates a photon with wavenumber $|\mathbf{k}| = \omega/c$ and polarization q while $\hat{b}_{\mathbf{k},q}$ annihilates a photon with the same properties. The sum-integral extends over all possible wavenumbers and polarizations spanning the Hilbert space of the reservoir \mathcal{H}_R .

In CLS, the laser beam is usually a collimated Gaussian beam with a spectral width below 100 kHz, which in most cases is much smaller than the natural linewidth, and a laser power above 1 μ W. Similarly to the large thermal reservoir, it follows that changes to the laser field through photon absorption and emission can be neglected. Hence H_L can be removed from Eq. (2.68). Moreover, in first approximation and in the rest-frame of the atom, a laser beam k can be described as a classical monochromatic plane wave of the form

$$\mathbf{E}_k = \mathbf{q}\varepsilon \cos(\tilde{\omega}_k t), \quad (2.71)$$

where ε is the amplitude of the electric field, \mathbf{q} is the complex polarization vector and $\tilde{\omega}_k = 2\pi\nu$ is the angular frequency of the laser. Using again the dipole approximation, the laser-atom interaction can be written as

$$H_{\text{AL}} = \hbar \sum_k \sum_{\substack{i,j \\ i \neq j}} \hat{\sigma}_{ij} \Omega_{ij}^k \cos(\tilde{\omega}_k t), \quad (2.72)$$

where $\Omega_{ij}^k = \varepsilon \mathbf{d}_{ij} \cdot \mathbf{q} / \hbar$ are the complex-valued Rabi frequencies with the atomic dipole transition elements \mathbf{d}_{ij} .

2.4.2 The Lindblad master equation

To solve the dynamics of this problem computationally, the dependencies on “fast rotating” terms $e^{i\omega t}$ in Eq. (2.70) and (2.72), where ω lies in the optical regime, need to be removed. Following [129], this is achieved by applying the transformation

$$H' = U^\dagger H U + i\hbar \frac{dU^\dagger}{dt} U, \quad U := \exp(-itH_A/\hbar) \quad (2.73)$$

to get

$$H'_A = 0 \quad (2.74)$$

$$\begin{aligned} H'_{\text{AR}} &= \hbar \sum_{\substack{i,j \\ \omega_i < \omega_j}} \sum_{\mathcal{H}_R} \alpha_R(\Delta_{ij}) \hat{\sigma}_{ij}^\dagger \hat{b} e^{i\Delta_{ij}t} + \text{h.c. } d\mathbf{k}' \\ &\equiv i\hbar \sum_{\substack{i,j \\ \omega_i < \omega_j}} \left(\hat{\sigma}_{ij}^\dagger \hat{F}(t) - \hat{F}^\dagger(t) \hat{\sigma}_{ij} \right) \end{aligned} \quad (2.75)$$

$$H'_{\text{AL}} = \hbar \sum_k \sum_{\substack{i,j \\ \omega_i < \omega_j}} \frac{1}{2} \left(\Omega_{ij}^{k*} \hat{\sigma}_{ij}^\dagger e^{i\tilde{\Delta}_{ij}^k t} + \Omega_{ij}^k \hat{\sigma}_{ij} e^{-i\tilde{\Delta}_{ij}^k t} \right) \quad (2.76)$$

where $\Delta_{ij} := \omega_j - \omega_i - \omega$, $\tilde{\Delta}_{ij}^k := \omega_j - \omega_i - \tilde{\omega}_k$, with $\omega_i < \omega_j$ after applying the rotating-wave approximation (RWA), and \hat{F} is a time-dependent Langevin-force operator that couples the system to the thermal reservoir. The system Hamiltonian

$$H_S := H'_A + H'_{\text{AL}} \quad (2.77)$$

only describes coherent dynamics, whereas H'_{AR} perturbs the coherence and can dissipate energy into the reservoir. Under the set of conditions described below, the density matrix of the system

$$\rho_S := \text{Tr}_R(\rho) = \sum_{|b\rangle \in \mathcal{H}_R} \langle b|\rho|b\rangle \quad (2.78)$$

evolves according to the Lindblad master equation [127–129]

$$\frac{\partial \rho_S}{\partial t} = -\frac{i}{\hbar}[H_S, \rho_S] + \sum_{\substack{i,j \\ \omega_i < \omega_j}} \Gamma_{ij}(\bar{n}_{ij} + 1)\mathcal{D}[\hat{\sigma}_{ij}]\rho_S + \Gamma_{ij}\bar{n}_{ij}\mathcal{D}[\hat{\sigma}_{ij}^\dagger]\rho_S \quad (2.79)$$

$$\mathcal{D}[\hat{\sigma}]\rho := \hat{\sigma}\rho\hat{\sigma}^\dagger - \frac{1}{2}(\hat{\sigma}^\dagger\hat{\sigma}\rho + \rho\hat{\sigma}^\dagger\hat{\sigma}) \quad (2.80)$$

$$\bar{n}_{ij} \stackrel{\text{e.g.}}{=} \left[\exp\left(\frac{\hbar\omega_{ij}}{k_B T}\right) - 1 \right]^{-1} \quad (2.81)$$

where \bar{n} is the distribution of thermal photons with the Boltzmann constant k_B and the temperature T , $\mathcal{D}[\hat{\sigma}]$ is the Lindblad superoperator and Γ_{ij} is the spontaneous decay rate of state $|j\rangle$ into $|i\rangle$. Note that for optical frequencies $\bar{n}_{ij}(\hbar\omega_{ij} \gg k_B T) \approx 0$. While the system Hamiltonian is not limited to the simplifications made here, the following assumptions about the reservoir interaction need to be made for Eq. (2.79) to be valid:

1. Only dipole interactions are considered, *i.e.*, energy contributions of the form $E_{\text{dipole}} = \alpha \mathbf{S}^{(1)} \cdot \mathbf{T}^{(1)}$, where $\mathbf{S}^{(1)}$ is a dipole moment of the system and $\mathbf{T}^{(1)}$ the dipole moment of an external field.
2. The coupling of the atom to the thermal reservoir is weak, so that $\Gamma_{ij} \ll \omega_{ij}$. Terms of the order α_R^3 and higher are neglected.
3. Energy corrections of the system eigenstates due to the interaction with the thermal reservoir and self-interaction are neglected.
4. System and thermal reservoir are decoupled and the reservoir is in thermal equilibrium from the beginning, so that $\rho(t) = \rho_S(t) \otimes \rho_R(0)$.
5. The dynamics of fast oscillating terms of the order $\omega_{ij} + \omega \gg |\omega_{ij} - \omega|$ are neglected (RWA).

Note that H_S is still explicitly time-dependent. This time dependence can be removed with a unitary transformation if the laser-driven transitions do not form loops. The required unitary transformation is introduced in Sec. 3.3.3.

2.4.3 Rate equations

For simulations surrounding CLS, the accurate coherent solution of the master equation is often not required, since dipole transitions mostly have short lifetimes compared with the usual interaction time in the experiment. In this case, it is sufficient to assume that coherences between atomic states are in equilibrium so that the off-diagonal density matrix elements are time-independent, $\partial\rho_{ij}/\partial t = 0$ for $i \neq j$. The description of the state dynamics can then be limited to the diagonal elements of ρ which yields the rate equations [130]

$$\frac{\partial\rho_{ii}}{\partial t} = \sum_{j \neq i} \left(\sum_k R_{ij}^k \right) (\rho_{jj} - \rho_{ii}) + (\bar{n}_{ij} + 1)(\Gamma_{ij}\rho_{jj} - \Gamma_{ji}\rho_{ii}) + \bar{n}_{ij}(\Gamma_{ji}\rho_{jj} - \Gamma_{ij}\rho_{ii}), \quad (2.82)$$

where R_{ij}^k are the elements of a symmetric matrix R^k that describes the stimulated emission and absorption rates induced by laser k . Specific expressions for R_{ij}^k , Γ_{ij} as well as the dipole transition elements d_{ij} are given in Sec. 3 for a general atomic system with hyperfine structure. In Fig. 2.3, a solution of the rate equations for a closed transition is compared with the solution of the master equation and a Monte-Carlo master equation approach discussed in the next section. In Sec. 5.1.3, the rate equations are used to simulate a fluorescence spectrum obtained from saturation spectroscopy.

2.4.4 Monte-Carlo master equation

The Lindblad master equation defined in Eq. (2.79) does not include the mechanical dynamics of the atom in the laser field. Including the momentum of the atom in the system Hamiltonian requires solving the time evolution of 3-dimensional¹ probability density functions for the n discrete internal states of the atom. This is computationally challenging. A simpler approach is a Monte-Carlo simulation that evolves the system Hamiltonian coherently until a spontaneous decay event occurs that resets the system. When this happens, the coherence information is lost and the Hamiltonian can be adjusted to describe the changed situation after the decay, e.g., due to a changed momentum. The basic principle of this approach is to evolve the Hamiltonian according to the Schrödinger equation

$$i\hbar \frac{\partial\psi(t)}{\partial t} = H\psi(t), \quad (2.83)$$

with the complex state vector $\psi(t)$, and let the dissipative interaction with the reservoir decrease the norm $|\psi(t)|^2$ according to the rates Γ_{ij} such that

$$|\psi(0)|^2 = 1 \quad \text{and} \quad |\psi(t \rightarrow \infty)|^2 = 0. \quad (2.84)$$

The Hamiltonian that fulfills these conditions can be written as [131, 132]

¹6-dimensional for the complete phase-space if spatial variations of the laser fields are included.

$$H = H_S - \frac{i\hbar}{2} \sum_n C_n. \quad (2.85)$$

where C_n are the transition operators that, in case of the Hamiltonian described in Sec. 2.4.2 are given by

$$C^- = \Gamma(\bar{n} + 1)\hat{\sigma}^\dagger\hat{\sigma}, \quad C^+ = \Gamma\bar{n}\hat{\sigma}\hat{\sigma}^\dagger, \quad (2.86)$$

where all the indexes ij were omitted for better visibility. An incoherent interaction occurs whenever the norm $|\psi(t)|^2$ falls below a uniformly randomly generated number $c \in (0, 1]$. The state of the atom afterwards is determined by the relative probabilities of the transitions at the time when the “collapse of the state vector” occurs

$$p_n(t) = \frac{\langle \psi(t) | C_n | \psi(t) \rangle}{\sum_i \langle \psi(t) | C_i | \psi(t) \rangle}. \quad (2.87)$$

The time evolution of the new state vector is again governed by the Schrödinger equation. Advantageously, the Hamiltonian that defines the time evolution after the collapse can be altered since the coherence is lost. For example, the detunings of the lasers in H'_{AL} can be adjusted to move into the rest-frame of the atom after a momentum change. This can be used to classically simulate photon recoils while retaining a coherent time evolution of the system states. Figure 2.3 shows results of the simulation of photon recoils caused by driving the closed ${}^3S_1, F = 3/2 \rightarrow {}^3P_2, F' = 5/2$ transition of ${}^{13}\text{C}^{4+}$ with a laser. The time evolution of the atomic states calculated with the Monte-Carlo approach perfectly follows the result from the standard master equation approach. The result obtained from solving the rate equations deviates during the first 0.1 μs and then reproduces the same equilibrium state as the coherent methods. The number of photon recoils defined as $n_{\text{rec}} := \delta v_x / v_{\text{rec}}$ follow distributions with frequency-dependent means that itself follow a Lorentzian centered around the resonance frequency with a slight shift towards larger frequencies. The mean number of photon recoils reaches 2.4 in resonance and drops below 1 roughly at a distance of one natural linewidth from the center frequency.

2.4.5 Photon scattering rate

In fluorescence spectroscopy, a resonance signal is obtained from photons spontaneously emitted by an atom that passes the acceptance angle of the detector. The rate of photons scattered into a direction \mathbf{k}_{sc} through spontaneous decay can be calculated from the system density matrix ρ_S by defining a detection operator [100]



Figure 2.3: (a) The time evolution of the 3S_1 and 3P_2 states of $^{13}\text{C}^{4+}$ driven by a laser being resonant with the $F = 3/2 \rightarrow F' = 5/2$ transition, which was simulated with the `qspec` package introduced in Sec. 3. The Monte-Carlo (MC) master equation approach (solid line) is compared to solutions of the conventional master equation (dashed line) and the rate equations (dotted line). To produce the shown statistics in the solution of the MC master equation, $\sim 10\,000$ ions were simulated. (b) The velocity distribution of ions now in the 3P_2 state at the time they were excited after a total propagation time of $0.29\, \mu\text{s}$ for different laser frequencies in units of the recoil velocity $v_{\text{rec}} = 0.135\, \text{m/s}$. The simulation is started in the rest-frame of each ion such that $\mathbf{v}(t = 0) = \mathbf{0}$.

$$D(\mathbf{k}_{\text{sc}}) := \frac{1}{4\pi} \sum_{\mathbf{q} \in \mathcal{P}(\mathbf{k}_{\text{sc}})} \sum_{f \in \mathcal{F}} \sum_{i, j \in \mathcal{I}_f} \sqrt{\Gamma_{fi} \Gamma_{fj}} \frac{(\mathbf{q} \cdot \mathbf{d}_{fi})(\mathbf{d}_{fj}^* \cdot \mathbf{q}^*)}{\mathbf{d}_{fi} \cdot \mathbf{d}_{fj}^*} \hat{\sigma}_{ij}, \quad (2.88)$$

where \mathcal{F} is the set of all final states, \mathcal{I}_f is the set of all states whose spontaneous decay into state $|f\rangle$ is detectable and $\mathcal{P}(\mathbf{k}_{\text{sc}})$ is a basis set of polarizations for a photon with propagation direction \mathbf{k}_{sc} . Calculating the expectation value is straightforward and yields

$$\frac{d\Gamma}{d\Omega}(\mathbf{k}_{\text{sc}}) := \text{Tr}(\rho_S D(\mathbf{k}_{\text{sc}})) = \frac{1}{4\pi} \sum_{\mathbf{q} \in \mathcal{P}(\mathbf{k}_{\text{sc}})} \sum_{f \in \mathcal{F}} \sum_{i, j \in \mathcal{I}_f} \sqrt{\Gamma_{fi} \Gamma_{fj}} \frac{(\mathbf{q} \cdot \mathbf{d}_{fi})(\mathbf{d}_{fj}^* \cdot \mathbf{q}^*)}{\mathbf{d}_{fi} \cdot \mathbf{d}_{fj}^*} \rho_{ij}^*, \quad (2.89)$$

with the density matrix elements ρ_{ij} . In order to solve Eq. (2.89) for an actual atomic system, specific coordinate systems need to be chosen. A possible choice is described in Sec. 3.3.2. This scattering rate also includes quantum interference (QI) effects. In Sec. A.1, it is used to simulate the fluorescence spectrum of $^{87}\text{Sr}^+$ and to compare it to a perturbative QI scattering rate described in [133] that does not take optical population transfer into account. The hyperfine structure spectrum of a closed electronic transition in terms of the perturbative

scattering rate can be written as [133, 134]

$$\begin{aligned}
\frac{d\Gamma}{d\Omega}(\mathbf{k}_{sc}) &:= \frac{1}{4\pi} \frac{I}{I_0} \left(\frac{\Gamma}{2}\right)^3 \left[\sum_{F'} \frac{f(\mathbf{q}, \mathbf{k}_{sc}, F, F')}{\Delta_{FF'}^2 + (\Gamma/2)^2} + \sum_{\substack{F', F'' \\ F' \neq F''}} \frac{g(\mathbf{q}, \mathbf{k}_{sc}, F, F', F'')}{(\Delta_{FF'} + \frac{i}{2}\Gamma)(\Delta_{FF''} - \frac{i}{2}\Gamma)} \right] \\
f(\mathbf{q}, \mathbf{k}_{sc}, F, F') &= A_F^{F'} + B_F^{F'} p(\mathbf{q}, \mathbf{k}_{sc}) \\
g(\mathbf{q}, \mathbf{k}_{sc}, F, F', F'') &= C_F^{F'F''} p(\mathbf{q}, \mathbf{k}_{sc}) \\
I_0 &= \frac{\hbar\Gamma\omega^3}{12\pi c^2}, \tag{2.90}
\end{aligned}$$

where the geometric factor $p(\mathbf{k}_{sc}, \mathbf{q})$ takes values in $[-0.5, 1]$ and depends on the polarization of incident and the directions of detectable scattered photons, I_0 is the saturation intensity and Γ is the natural linewidth of the closed electronic transition. The coefficients $A_F^{F'}$, $B_F^{F'}$ and $C_F^{F'F''}$ purely depend on angular momentum algebra and can be calculated according to the formulas in [133].

3 Python package *qspec*

The analysis of experimental results often requires writing many code scripts or programs that are based on functions that describe the physics of the experiment. In a certain field of science, those functions are most probably the same for many users. To facilitate the analysis and simulation of laser spectroscopy experiments, the *qspec* Python package was developed. It provides common physical functions, models and simulations but also more general methods for data processing. Whenever useful, the functions are compatible with *numpy* arrays, enabling fast processing of large data samples. Apart from *numpy*, a minimal set of scientific Python packages are required. These are the established packages *scipy* [135], *sympy* and *matplotlib* [136]. As parts of the *qspec* package are written in C++, currently only Windows systems are supported. However, the package may be extended to Linux-based systems or Mac OS in the future. Other Python packages whose contents overlap with the *qspec* package are *satlas2* which is used by laser spectroscopy groups at KU Leuven, CERN/ISOLDE and JYVL for fitting of online data [66, 67] and, e.g., the *PyLCP* package for simulating laser cooling of alkali atoms [137]. How *qspec* differs from these existing packages is illustrated in the following. The *qspec* package is available on the Python Package index (PyPi) [138].

3.1 Structure

The *qspec* package consists of seven main modules. These are named *algebra*, *analyze*, *models*, *physics*, *simulate*, *stats* and *tools* and are summarized in the following. All functions and variables can be accessed directly without the need to specify the correct module by importing the entire package.

qspec.algebra The *algebra* module contains functions related to angular momentum coupling such as Wigner-*j*-symbols, reduced dipole matrix elements and relative transition strengths for electronic transitions. It makes use of the *sympy* package to determine algebraic expressions of these objects.

qspec.analyze The *analyze* module contains general purpose routines for data fitting as well as a convenience class for King plots [139]. For fitting nonlinear data, these routines include wrappers that extend the *scipy.optimize.curve_fit* and the *scipy.odr.odr* routine, which use least square optimization and orthogonal distance regression, respectively.

For fitting linear functions to data, the algorithm developed by York *et. al.* [140] and the Monte-Carlo method explained in the supplementary material of [141] were implemented. The latter can also be used to fit a straight line to data points in an *n*-dimensional vector

space. Both algorithms take correlations between all vector components of the data points into consideration.

qspec.models The *models* module contains classes and helper functions to primarily, but not exclusively, create lineshape models of fluorescence spectra in a modular way for nonlinear curve-fitting. This module can be compared to the *satlas2* Python package which is commonly used by laser spectroscopy groups at KU Leuven, CERN/ISOLDE and JYVL [66, 67]. In *models*, additional features such as a numerical convolution of two models or consideration of quantum interference (QI) effects are available. The *models* module is described in more detail in Sec. 3.2.

qspec.physics The *physics* module provides basic physical relations and observables surrounding collinear laser spectroscopy (CLS). Examples are relations between particle energy, velocity, acceleration voltage and Doppler-shifted laser frequency or functions to calculate hyperfine structure or Zeeman shifts, refractive indices, photon recoils, etc.

qspec.simulate The *simulate* module offers simulations of laser-atom interactions. The core feature is an object-oriented solver for the master, rate and Schrödinger equations, written in C++ for better performance, which can be set up as easy as drawing an atomic level scheme. Additional functions to calculate, *e.g.*, quantum interference effects in fluorescence spectra are also included. The *simulate* module is described in Sec. 3.3.

qspec.stats The *stats* module contains routines for the statistical analysis of data. In addition to basic statistical measures such as the (weighted) average or median, the module also provides a Monte-Carlo error propagator. In combination with the nonlinear curve fitters of the *analyze* module, this can be used to calculate uncertainty bands of fitted functions under consideration of all parameter correlations.

qspec.tools The *tools* module provides multidimensional methods for data processing, general mathematical functions as well as general functions useful for scripting. Some examples are the conversion between lists and dictionaries, merging intervals, rounding to n significant decimal places, transforming vectors or printing colored text to the console.

3.2 Modular lineshape models

The *models* module was built to serve as a new basis for fitting and analyzing fluorescence spectra using the group-internal analysis program *Pollifit*. For this, a complete new graphical user interface (GUI) which supports all features of *models* and vastly extends the functionality of the previous GUI was implemented. Although so far, only the specific data-file format produced by the group-internal data acquisition system is supported, other data formats may be added in the future. The underlying *models* itself can be used independently of the GUI and specific file formats.

3.2.1 Modular system

The general structure of the modular system is depicted in Fig. 3.1. All models inherit from the super class *Model*. Instances of *Model* are callable with a defined number of arguments which are an *x*-value and the parameters of the defined fit model. Different models can be combined by specifying the attribute *model* which is always the first argument of the constructor of a model and can either be *None* or another *Model* instance. For example, a Gaussian peak with a variable amplitude that is shifted along the *x*- and *y*-axis

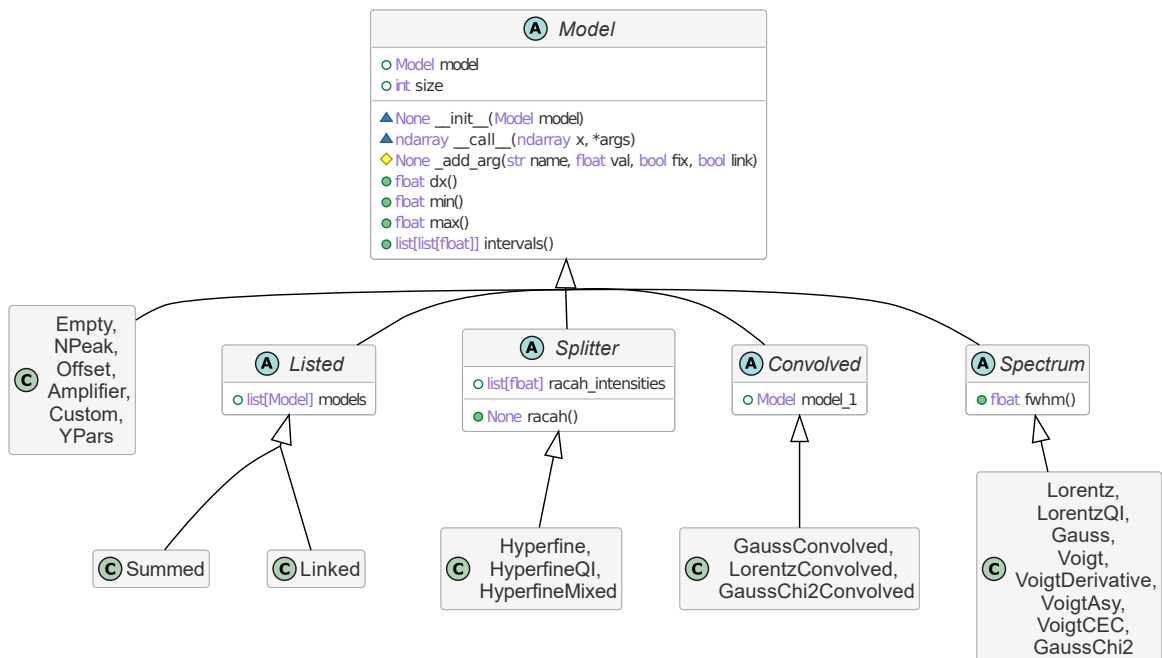


Figure 3.1: Inheritance diagram of the classes contained in *qspec.models* including characteristic attributes and methods. Attribute types are colored purple. The solid arrow lines indicate inheritance. The diagram was generated using the program *PlantUML*.

$$f(x, \sigma, p_0, x_0, y_0) = p_0 \exp \left[\frac{(x - x_0)^2}{2\sigma^2} \right] + y_0 \quad (3.1)$$

may be defined by combining three models as in the following lines of code.

```

1 | f = Offset(NPeak(Gauss(), n_peaks=1), offset=[0])
2 | # f.names = ['sigma', 'x0', 'p0', 'off0e0']

```

Here, a gaussian model with the parameter σ is passed to an *NPeak* model, which creates a single amplitude parameter p_0 and *x*-axis shift parameter x_0 , that is then passed to the *Offset*

model which adds a zeroth-order polynomial as y -axis offset, *i.e.*, a constant y_0 . The line starting with `#` is a comment that shows the names of the model parameters.

Once a model is defined, it can be further customized by modifying the behavior of the individual parameters. Parameters can be free, fixed, functions of other parameters, have hard bounds or be constraint by an expectation value with an uncertainty that is considered during fitting. The following lines of code define a model of two separated Gauss peaks, where σ_0 is expected to assume the value 5(0.9) and $\sigma_1 = 2\sigma_0$.

```
1 | f = Summed([Gauss(), Gauss()])
2 | f.set_fix(0, '5(0.9)')
3 | f.set_fix(1, '2 * sigma_0')
4 | # f.names = ['sigma_0', 'sigma_1',
5 | #                 'center_0', 'int_0', 'center_1', 'int_1']
```

If multiple data sets are to be fitted with the same model and shared parameters, the *Linked* model can be used. Consider the following lines of code.

```
1 | models = [Gauss() for _ in range(3)]
2 | for m in models:
3 |     m.set_link(0, True)
4 | f = Linked(models)
5 | # f.names = ['sigma_0', 'sigma_1', 'sigma_2']
6 | # f.fixes = [    False, 'sigma_0', 'sigma_0']
```

Here, three *Gauss* models are created and their σ are specified to be linked. The *Linked* model has σ_1 and σ_2 fixed to σ_0 and takes a list of x -arrays as the first argument when called. In CLS, spectra often show hyperfine structures caused by multiple nuclear states [142–144]. The *Hyperfine* model or a sum thereof facilitate fitting hyperfine spectra and only require the peak model, the total angular momenta J, J' of the electronic states and the nuclear spin I for instantiation. Variations of the *Hyperfine* model are available that also consider quantum-interference effects and hyperfine-induced mixing. Models that use lineshapes that cannot be described by a Voigt, such as the quantum-interference model or a model that correctly describes the Doppler compression of thermally distributed ions, often do not include the Gauss or Lorentz contribution appearing in the experiment. These models require to calculate a convolution integral for which an analytic expression is often not available. For this, *qspec.models* provides the *Convolved* model which solves the convolution integral numerically. It is clear that combining or linking models and data sets which also need to solve integrals quickly get computationally expensive. Therefore, the number of required model function calls was minimized. A performance test of *qspec.models* is described in the following section.

3.2.2 Benchmark

The computation of a fit model should be fast to enable the analysis of large amounts of data. The performance of the *models* module was tested by comparing its execution time to that of the *satlas2* package for a fit with shared parameters to different data sets. The data sets are randomly generated hyperfine structure spectra of a $J = 1/2 \rightarrow J' = 3/2$ transition with nuclear spin $I = 7/2$. The following model was used to fit a single data set

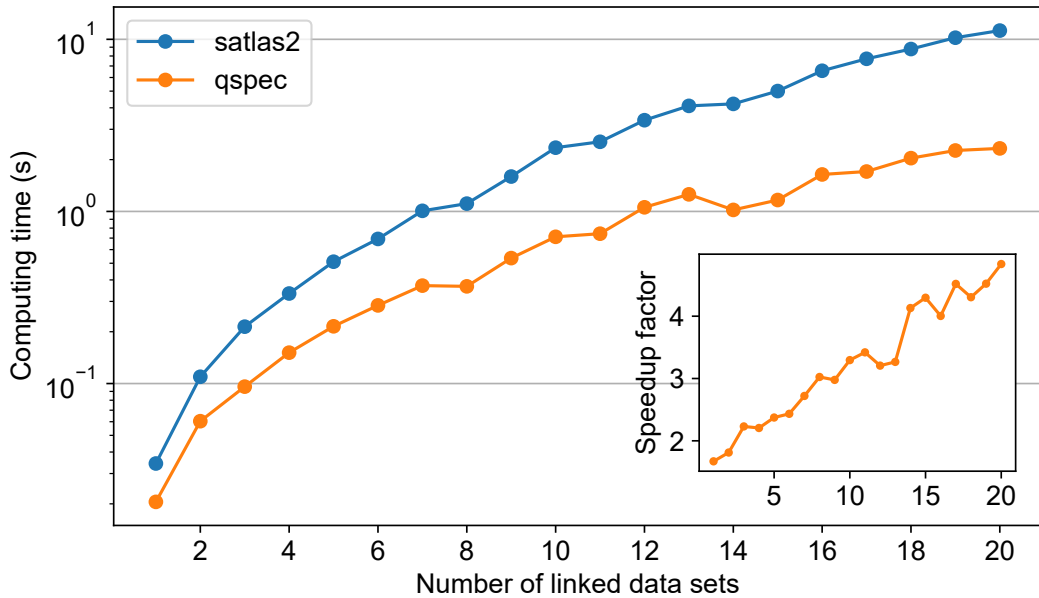


Figure 3.2: Performance of *qspec* compared with the *satlas2* package for fitting different numbers of linked data sets. The computing time of *satlas2* divided by that of *qspec* grows linearly with the number of linked data sets as shown in the plot inset. The results of *satlas2* are correctly reproduced by *qspec*.

$$\begin{aligned}
 f(x, \Gamma, \sigma, A_{\text{l}}, A_{\text{u}}, B_{\text{u}}, p_0, x_0, y_0) \\
 = \sum_{|F_{\text{u}} - F_{\text{l}}| \leq 1} p_0 \text{Voigt}[x - x_0 - \delta x_{\text{u}}(A_{\text{u}}, B_{\text{u}}) + \delta x_{\text{l}}(A_{\text{l}}), \Gamma, \sigma] + y_0
 \end{aligned} \tag{3.2}$$

where Γ and σ are the Lorentz and Gauss widths, $\delta x_{\text{l/u}}$ are the hyperfine structure shifts of the lower and the upper states according to Eq. (2.16), $A_{\text{l/u}}$ and B_{u} are the hyperfine structure constants, p_0 is the signal height and x_0 and y_0 are the x - and y -axis offsets, respectively. The fits of the individual data sets are linked by sharing all fit parameters except p_0 and y_0 . This benchmark test was adopted from the documentation of *satlas2* where it was compared to its predecessor *satlas*. There, a 100-times lower computing time was found for *satlas2*. Figure 3.2 shows the computing time of *satlas2* and *qspec* as well as the ratio of these. The *qspec* package further reduces the computing time by a factor that increases linearly with the number of linked data sets. In the case of this test, a factor of 4 is achieved at around 15 linked data sets. This test proves that *qspec* is capable of supporting the analysis of large data sets and can serve as an alternative to the established *satlas2* package. The speed improvement and features that are not available in *satlas2* such as numerical convolutions, consideration of quantum interference effects and using soft bounds for parameters are advantages of the *qspec* package.

3.3 Simulation of laser-atom interactions

Controlling the population dynamics of the electronic states of an atom in laser fields allows for many interesting applications such as optical population transfer [145], polarizing ion beams in storage rings [146, 147], driving Raman transitions [148] or quantum computing [149]. To predict and interpret experimental results, accurate and fast calculations of the dynamics are required. A powerful and well-established tool to solve the dynamics of open quantum systems in general is the *qutip* Python package [132]. However, it requires the user to set up simulations by manually defining Hamiltonians which can be quite challenging and laborious if large atomic systems are to be investigated. The *qspec.simulate* module provides an intuitive object-oriented user interface that is comparable to drawing an atomic level scheme and is described in Sec. 3.3.1. The mathematical objects required to solve the Schrödinger, master or rate equations are generated automatically from the definition of the laser-atom system, which is described in Sec. 3.3.3. The *simulate* module also allows to include the mechanical dynamics of atoms in laser fields using a Monte-Carlo approach for the master equation. This is used in Sec. 5.2.3 to estimate systematic shifts caused by photon recoils in CLS. It should be noted that other Python packages exist that also describe laser-atom interactions. However, often they are developed for a specific application such as, e.g., the *PyLCP* package for laser cooling of alkali atoms [137]. Although the fundamental structure of *qspec.simulate* is designed to be as general as possible and easy to expand, currently the implemented functions are limited to applications surrounding laser spectroscopy with “classical” lasers. An evaluation of upgradability and an overview of features planned for the future are given in Sec. 3.3.4. An introduction to the mathematical description of laser-atom interactions as they are implemented in *qspec.simulate* is provided in Sec. 2.4.

3.3.1 Structure of *qspec.simulate*

The classes that define a laser-atom interaction are depicted in Fig. 3.3. An *Atom* object holds a list of states $|SL; JI; Fm\rangle$ and a *DecayMap* object that defines the spontaneous decay channels. A *State* is defined by its quantum numbers. The user specifies the eigenfrequency of the decoupled $|SL; J\rangle$ state. Additional shifts are calculated from hyperfine structure constants and the electro-magnetic *Environment*. A state label, that does not have to be unique, is used to link states through the *DecayMap*. Here, a list of label pairs is identified with a list of Einstein A_{ji} coefficients. A *Laser* object defines an electro-magnetic plane wave that has a frequency, intensity, *Polarization* and direction. The *Polarization* encapsulates the complex amplitude of the electro-magnetic wave which is specified either in cartesian coordinates directly or in the rotating frame of the atom as $\mathbf{q} = (q_{\sigma-}, q_{\pi}, q_{\sigma+})^T$. The transformation between the two coordinate systems is derived from the specified quantization axis and is described in more detail in Sec. 3.3.2. An atom and a list of lasers are combined in an *Interaction* object. The *Interaction* object generates the Hamiltonian in dipole and rotating-wave approximation as well as rate matrices from the properties of the atom and the lasers to be used in a set of solvers. How the Hamiltonian is constructed is described in detail in Sec. 3.3.3. Currently, the solvers include the Einstein rate equations, the Schrödinger equation, the master equation as well as a Monte-Carlo solver for the master equation which also allows to simulate the mechanical

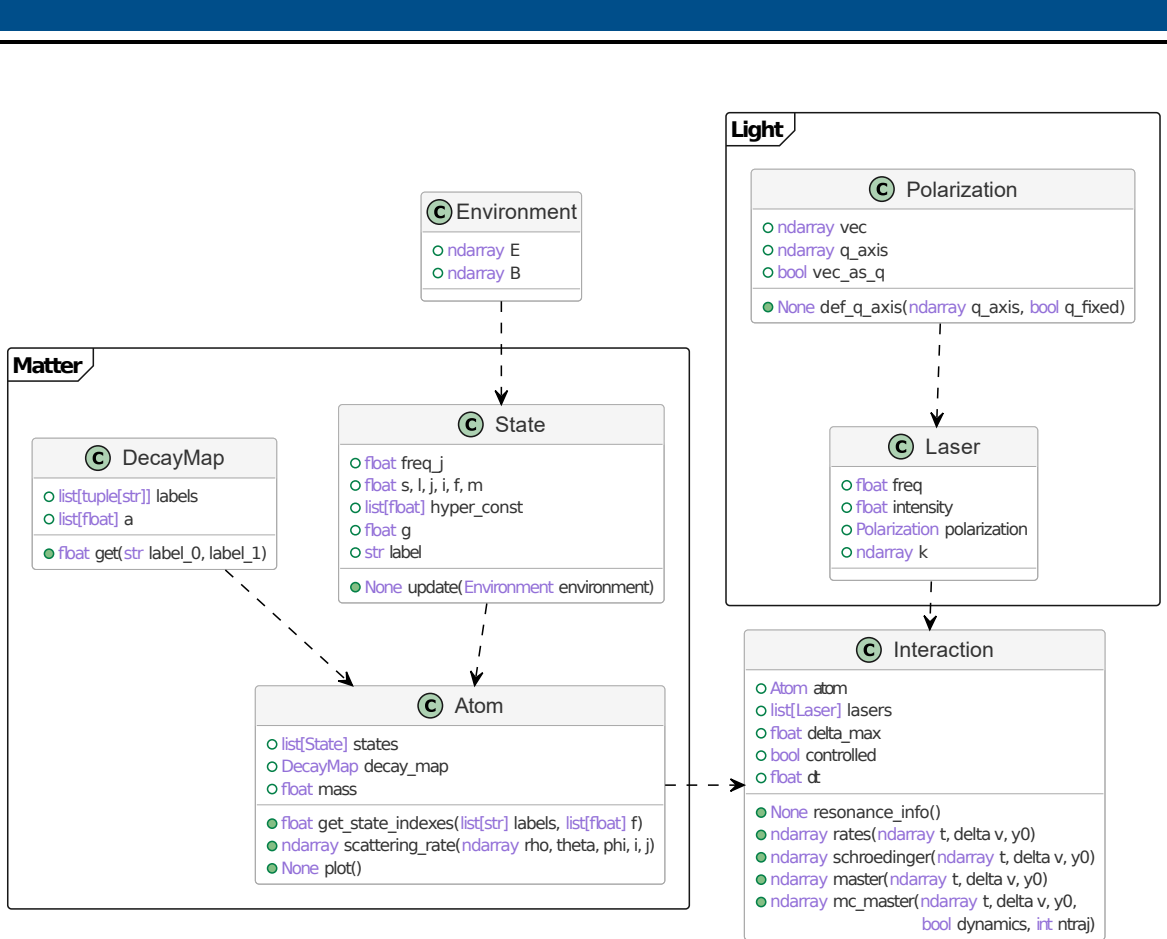


Figure 3.3: Classes contained in `qspec.simulate` that are used to set up a simulation including characteristic attributes and methods. The single dashed arrow lines indicate that objects of a class are contained in attributes of another class. The diagram was generated using the program *PlantUML*.

dynamics of the atom in the laser fields. The differential equations underlying the solvers are introduced in Sec. 2.4. The solvers must be fine-tuned to the time scale of the interaction by using the `controlled` attribute or by manually setting the integration steps `dt`. The solvers return the population of the atomic states in their distinct format, *i.e.*, population vectors, state vectors or density matrices. The density matrix of the system, or an array thereof, can be passed to the `Atom` object to calculate the scattering rate into a solid angle Ω according to Eq. (2.89).

3.3.2 Coordinate transformations

Specific coordinate systems need to be fixed to relate the polarization of a laser to σ^\pm and π transitions in the atom and those to a scattering rate into a solid angle in the laboratory coordinate system. The inner structure of an atomic system is commonly described in a complex spherical basis. If the quantization axis is arbitrarily chosen to be the z -axis, the spherical basis vectors in cartesian coordinates are given by

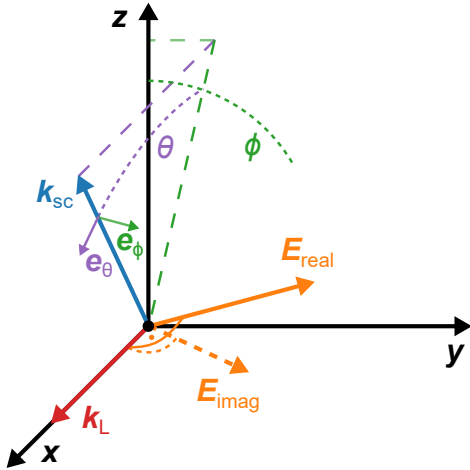


Figure 3.4: Standard coordinate system used in *qspec.simulate*. Without explicit specification by the user, lasers propagate along the x -axis (red). The real and complex polarization vectors (orange) then lie in the yz -plane. The direction of scattered light (blue) is specified through the angles $\theta \in [-\pi/2, \pi/2]$ (purple) and $\phi \in [0, 2\pi]$ (green). The basis set of the polarization of the scattered light is given by the two unit vectors e_θ and e_ϕ .

$$e_{-1} = \frac{1}{\sqrt{2}} \begin{pmatrix} 1 \\ i \\ 0 \end{pmatrix} \quad e_0 = \begin{pmatrix} 0 \\ 0 \\ 1 \end{pmatrix} \quad e_{+1} = \frac{1}{\sqrt{2}} \begin{pmatrix} -1 \\ i \\ 0 \end{pmatrix}. \quad (3.3)$$

If the polarization of light is expressed in the spherical basis, then the polarization components proportional to e_{-1} , e_0 and e_{+1} excite the σ^- , π and σ^+ transitions, respectively. Therefore, *qspec.simulate* transforms the polarization vector into the complex spherical basis using the unitary transformation

$$T = \frac{1}{\sqrt{2}} \begin{pmatrix} 1 & -i & 0 \\ 0 & 0 & \sqrt{2} \\ -1 & -i & 0 \end{pmatrix}. \quad (3.4)$$

The user specifies the polarization, *i.e.*, the complex-valued electric field amplitude, either in cartesian or directly in spherical coordinates with respect to a user-defined quantization axis. For example, the following line of code creates σ^+ polarization with respect to e_x which is the default laser propagation direction.

```
1 | pol = Polarization([0, 0, 1], vec_as_q=True, q_axis=[1, 0, 0])
2 | # pol.x = [0., 0.70710678j, 0.70710678]
3 | # pol.q = [0., 0., 1.]
```

The attributes x and q are the resulting polarization vectors in cartesian and spherical coordinates, respectively. In the atomic system, where the quantization axis was set to e_z , the above defined polarization is not pure σ^+ light anymore. By transforming the cartesian polarization vector x according to the rotation R of the quantization axis of the atom (here e_z) onto the user-defined quantization axis of the polarization (here e_x), the resulting vector can be expressed in the spherical basis of the atom

$$\mathbf{q}' = T(R\mathbf{x}) = \begin{pmatrix} 1 \\ \sqrt{2} \\ 1 \end{pmatrix}. \quad (3.5)$$

The dynamics of the state population in the atom can be calculated now by distributing the laser power according to \mathbf{q}' . Note that in the presence of an external magnetic flux density \mathbf{B} , the rotation R is extended by the rotation of \mathbf{e}_z onto \mathbf{B} .

Light emitted from the atom in the laboratory frame is best described in spherical polar coordinates as depicted in Fig. 3.4. The angles (θ, ϕ) are defined so that \mathbf{e}_r lies in the polarization plane for $\theta = 0$. The orthonormal unit vectors of the spherical polar coordinate system are [134]

$$\mathbf{e}_r = \begin{pmatrix} \sin(\theta) \\ \cos(\theta) \sin(\phi) \\ \cos(\theta) \cos(\phi) \end{pmatrix} \quad \mathbf{e}_\theta = \begin{pmatrix} \cos(\theta) \\ -\sin(\theta) \sin(\phi) \\ -\sin(\theta) \cos(\phi) \end{pmatrix} \quad \mathbf{e}_\phi = \begin{pmatrix} 0 \\ \cos(\phi) \\ -\sin(\phi) \end{pmatrix}. \quad (3.6)$$

The angle-dependent scattering rate defined in Eq. (2.89) can be calculated straightforward by transforming the spherical transition dipole moments $\mathbf{d}' = (d_{-1}, d_0, d_{+1})^T$ into the laboratory frame

$$\mathbf{d} = T^{-1}\mathbf{d}' = \frac{1}{\sqrt{2}} \begin{pmatrix} [d_{-1} - d_{+1}] \\ -i[d_{-1} + d_{+1}] \\ \sqrt{2}d_0 \end{pmatrix} \quad (3.7)$$

and calculating the scalar products $\mathbf{e}_\theta \cdot \mathbf{d}$ and $\mathbf{e}_\phi \cdot \mathbf{d}$ of the two possible polarizations [133]. The integral

$$\Gamma_{\text{sc}} = \iint_{\Omega} \frac{d\Gamma_{\text{sc}}}{d\Omega'}(\theta, \phi) \cos(\theta) d\theta d\phi \quad (3.8)$$

gives the total scattering rate into the solid angle Ω . The scattering rate into the full 4π solid angle does not depend on off-diagonal elements of the density matrix and thus can be obtained faster by multiplying the spontaneous decay rate with the excited state population for all detectable decay channels

$$\Gamma_{\text{sc}}(4\pi) = \sum_{f \in \mathcal{F}} \sum_{i \in \mathcal{I}_f} \Gamma_{fi} \rho_{ii}. \quad (3.9)$$

3.3.3 Construction of differential equations

To solve the differential equations describing the laser-atom interactions introduced in Sec. 2.4, the required mathematical objects such as rate matrices and Hamiltonians need to be constructed from the user-specified state information. The user specifies states $|i\rangle$ with eigenfrequencies ν_i , that are linked through spontaneous decay, as well as lasers with frequencies $\tilde{\nu}_k$, intensities I_k and polarizations q^k . *Interaction* objects combine the atomic states with the lasers by first creating a symmetric map

$$M_{ij}^k = \begin{cases} 1 & |i\rangle \leftrightarrow |j\rangle \text{ driven by laser } k \\ 0 & \text{else} \end{cases} \quad (3.10)$$

of all states. Two states $|i\rangle$ and $|j\rangle$ are only driven by laser k if the following conditions are fulfilled

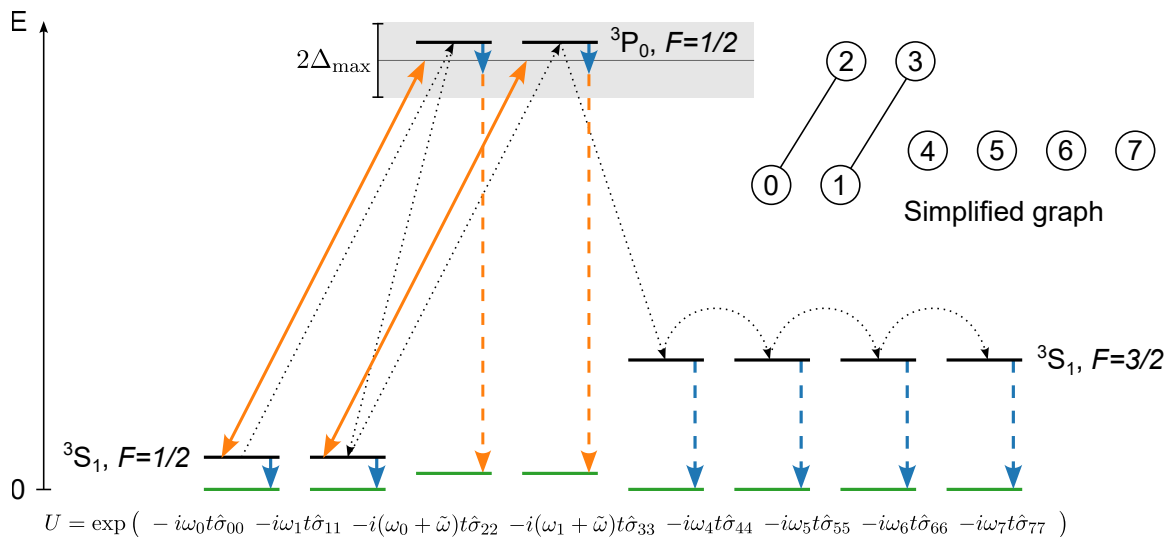


Figure 3.5: Transformation scheme for a Hamiltonian of a π -polarized laser that drives a $^3S_1, F = 1/2 \rightarrow ^3P_0, F' = 1/2$ transition. The degenerate magnetic sublevels depict the diagonal elements of the Hamiltonian before (black) and after (green) the unitary transformation U is applied. Laser-driven transitions are shown as solid orange arrows. The energy shifts from the transformation are shown as dashed colored arrows. The black dotted arrows show the propagation path through the six independent graphs. The resonance condition Δ_{\max} can be chosen freely. Note that here, the laser would additionally drive the transitions $2 \leftrightarrow 5$ and $3 \leftrightarrow 6$ if $\Delta_{\max} > |\omega_2 - \omega_5 - \tilde{\omega}|$. This would change the graph and thus, also the transformation U .

$$|J_j - J_i| \leq 1, \quad 0 \leftrightarrow 0 \quad (3.11)$$

$$|F_j - F_i| \leq 1, \quad 0 \leftrightarrow 0 \quad (3.12)$$

$$|m_j - m_i| \leq 1, \quad 0 \leftrightarrow 0 \quad \text{if } \Delta J, F = 0 \quad (3.13)$$

$$A_{ji} > 0, \quad \nu_j > \nu_i \quad (3.14)$$

$$I_k > 0 \quad (3.15)$$

$$(\mathbf{q}^k)_{m_j - m_i} \neq 0, \quad \nu_j > \nu_i \quad (3.16)$$

$$|\nu_j - \nu_i| - \tilde{\nu}_k \leq \Delta_{\max}, \quad (3.17)$$

with the Einstein A_{ji} coefficient and a frequency value Δ_{\max} set by the user to cut off fast oscillations in coherent dynamics. Using this map of laser-driven transitions, the objects required to construct the differential equations introduced in Sec. 2.4 can be obtained from the A_{ji} defined by the *DecayMap* object, angular momentum algebra and the symmetric rate matrix R^k following the conventions in [130, 133]

$$\tilde{\Gamma}_{ij} = \begin{cases} A_{ji} & \omega_i < \omega_j \\ A_{ij} & \text{else} \end{cases} \quad (3.18)$$

$$a_{ij} = (-1)^{I+J_j+F_i+1} \sqrt{2F_i+1} \sqrt{2J_j+1} \langle F_i, m_i; 1, m_j - m_i | F_j m_j \rangle \begin{Bmatrix} J_j & J_i & 1 \\ F_i & F_j & I \end{Bmatrix} \quad (3.19)$$

$$d_{ij} = \sqrt{\frac{3\pi\varepsilon_0 c^3 \hbar \tilde{\Gamma}_{ji}}{\omega_{ij}^3}} a_{ij} \quad (3.20)$$

$$\Omega_{ij}^k = E \frac{d_{ij}(\mathbf{q}^k)_{m_j - m_i}}{\hbar} M_{ij}^k = \sqrt{\frac{2I_k}{\varepsilon_0 c}} \frac{d_{ij}(\mathbf{q}^k)_{m_j - m_i}}{\hbar} M_{ij}^k \quad (3.21)$$

$$\Gamma_{ij} = a_{ij}^2 A_{ji} \quad (3.22)$$

$$R_{ij}^k = \frac{|\Omega_{ij}^k|^2 \tilde{\Gamma}_{ji}}{(\tilde{\omega}_k - |\omega_j - \omega_i|)^2 + \frac{1}{4} \tilde{\Gamma}_{ji}^2}, \quad (3.23)$$

where $\omega := 2\pi\nu$ are angular frequencies, $\tilde{\Gamma}$ is a symmetric matrix of natural linewidths and $\langle \dots | \dots \rangle$ are the Clebsch-Gordan coefficients.

For the Schrödinger and master equation, the Hamiltonian of the system given in Eq. (2.77) is required. For computational efficiency, it is desirable to have a time-independent Hamiltonian which does not depend on exponential functions. Hence, *qspec.simulate* transforms the Hamiltonian into an interaction picture and applies the rotating-wave approximation (RWA) to remove fast oscillating terms. However, if there is more than one laser driving a single transition or if multiple lasers form a loop of laser-driven transitions, the time-dependence cannot be eliminated completely. *qspec.simulate* automatically detects these loops and calculates the time-dependent Rabi frequencies. The algorithm implemented within this work can be imagined as a graph search in the undirected graph defined by the map M_{ij}^k . It is

illustrated and described in Fig. 3.5 based on a π -polarized laser with frequency $\tilde{\omega}$ that drives the $1s2s\ ^3S_1$, $F = 1/2 \rightarrow 1s2p\ ^3P_0$, $F' = 1/2$ transition in $^{13}\text{C}^{4+}$. The resulting time-independent Hamiltonian in this case is given by

$$H = (\omega_2 - \omega_0 - \tilde{\omega})(\hat{\sigma}_{22} + \hat{\sigma}_{33}) + \frac{\Omega}{2}(\hat{\sigma}_{02} + \hat{\sigma}_{13}) + \frac{\Omega^*}{2}(\hat{\sigma}_{20} + \hat{\sigma}_{31}), \quad (3.24)$$

where the indexes numerate the states depicted in Fig. 3.5 from left to right. Note that here, $\omega_0 = \omega_1$ and $\omega_2 = \omega_3$, due to the degeneracy of the magnetic substates. With the Hamiltonian constructed, `qspec.simulate` uses the two C++ libraries *Eigen* and *Boost.Numeric.Odeint* to perform matrix operations and integrate the differential equations, respectively. The following code example solves the master equation for the 8×8 density matrix of the system displayed in Fig. 3.5 for 101 laser frequencies in the interval $[-50 \text{ MHz}, 50 \text{ MHz}]$ and 291 time steps in the interval $[0 \mu\text{s}, 0.29 \mu\text{s}]$. This results in 1 881 024 complex-valued density-matrix elements. On an Intel® Core™ i7-9700K CPU, the master equation (line 32) took 58 ms to compute. The computing time of the other lines can be neglected.

```

1 import numpy as np
2 import qspec as qs
3 from qspec.simulate import *
4
5 mass = 13.001161 # Mass of 13C4+
6 a_ps = 56.21 # Einstein coefficient (MHz)
7 a_hyper = 42234.8 # HFS constant of the S state (MHz)
8 nu0 = 1_316_147_920.6 # Transition frequency (MHz)
9 dnu = qs.hyperfine(i=0.5, j=1, f=0.5, a=a_hyper) # HFS shift (MHz)
10
11 s = construct_electronic_state(
12     0., s=1, l=0, j=1, i=0.5, hyper_const=[a_hyper], label='s')
13
14 p = construct_electronic_state(
15     nu0, s=1, l=1, j=0, i=0.5, label='p')
16
17 decays = DecayMap([('s', 'p')], [a_ps])
18 c13 = Atom(s + p, decay_map=decays, mass=mass)
19
20 intensity = 1169 # Laser intensity (uW / mm2)
21 polarization = Polarization([0, 1, 0], vec_as_q=True)
22 laser = Laser(nu0 - dnu, intensity, polarization)
23
24 delta_max = 500 # Maximum laser detuning
25 interaction = Interaction(c13, [laser], delta_max=delta_max)
26 interaction.resonance_info()
27
28 delta = np.linspace(-50, 50, 101) # Create 101 frequency steps (MHz)
29 times = np.linspace(0, 0.29, 291) # Create 291 time steps (μs)
30
31 # Solving the master equation gives an array with shape (101, 8, 8, 291)
32 rho = interaction.master(times, delta=delta)
33 sc_rate = c13.scattering_rate(rho) # 4π scattering rate (MHz)

```

3.3.4 Outlook

The core feature of the *qspec.simulate* module is the automatic construction of all mathematical objects required to simulate laser-atom interactions from a simple specification of the system. For this, arbitrary atomic systems that only consist of discrete states can be specified. The differential equation solvers use multiprocessing to enable fast solutions for large parameter spaces. These features constitute a strong basis for an expansion of the module to a larger set of physical systems. New features that are straightforward to implement are, *e.g.*, molecular systems or finite laser linewidths $\gamma \ll A_{ji}$ that lead to dephasing. A larger effort would be the addition of the quantized radiation field to include the quantum dynamics of weak electro-magnetic fields or the inclusion of time- and position-dependent electric and magnetic fields. Other interesting expansions are time-dependent laser intensities and velocities. These would allow to simulate pulsed lasers and “classically” trapped ions, respectively. This also requires some caution. The simulation of pulsed lasers suggests high-energy laser pulses that drive non-dipole transitions or even ionize the atom. The implementation of a quantum-mechanically accurate description of high-energy laser pulses interacting with a general atom would be a large effort that is not foreseen in the nearer future. However, the addition of time-dependent incoherent transition rates between arbitrary states could be an option to effectively approximate such systems.

4 Experimental setup

The measurements discussed in this work were carried out at the Collinear Apparatus for Laser Spectroscopy and Applied Science (COALA) located in the Institute for Nuclear Physics at the Technical University of Darmstadt. An overview of the setup and its application is given in [61]. The most recent updates for the C^{4+} measurements are outlined in [62]. The beamline has been utilized in various high-precision collinear laser spectroscopy experiments and demonstrated a level of precision comparable to that of ion trap experiments [145, 150, 151]. Measurements of already known electronic transitions were used for high-precision high-voltage determination to provide a calibration reference for the most precise high-voltage dividers [152, 153]. Most recently, measurements with $^{12}C^{4+}$ were conducted that provide the absolute transition frequencies required to calculate the isotope shifts and the nuclear charge radii presented in this work [63, 64]. This chapter gives a detailed description of the current setup including all additional upgrades installed for the measurements with $^{13}C^{4+}$.

4.1 Electron beam ion source

A beam of $^{13}C^{4+}$ ions is produced in an electron beam ion source (EBIS-A, DREEBIT GmbH). A detailed characterization of the source is given in [63]. Here, only the information that is relevant for this work is given. A cross-sectional view of the ion-optical elements inside the EBIS and a sketch of the applied potentials is shown in Fig. 4.1. An electron beam with a beam current of 85 ± 2 mA is produced on a voltage potential of -2.1 kV by heating a cathode with a DC current of 4.20 ± 0.05 A and focused into the trap region with permanent magnets that produce a homogeneous magnetic field parallel to the electron-beam direction with a magnetic induction of $B \approx 600$ mT. The three segments of the axial electrostatic trap AT1, AT2 and AT3 can be set on individual voltages U_0 , U_A and U_{B1}, U_{B2} defining the high-voltage, the trap and the wall potentials, respectively. The voltage of the wall segment in beamline direction (AT3) can be rapidly switched between high (U_{B1}) and low (U_{B2}) to enable pulsed operation of the EBIS. Alternatively, it can be set to a voltage $U_A < U_{\text{Leak}} < U_0$ to produce a constant leak current of ions. The wall segment in opposing direction is fixed to the high-voltage potential U_0 .

The ions are produced in the focus of the electron beam on the trap potential U_A through electron-impact ionization and charge breeding. Once formed, the positively charged ions are confined axially by the electrostatic trap electrodes and radially by the negatively charged electron beam. Within this work, $^{13}C^{4+}$ ions were produced by introducing 99 %-enriched $^{13}CH_4$ methane gas at a pressure of $6 \cdot 10^{-8}$ mbar into the EBIS. After leaving the trap region as a pulsed or continuous beam, the ions pass the electron collector, repeller, an einzellens,

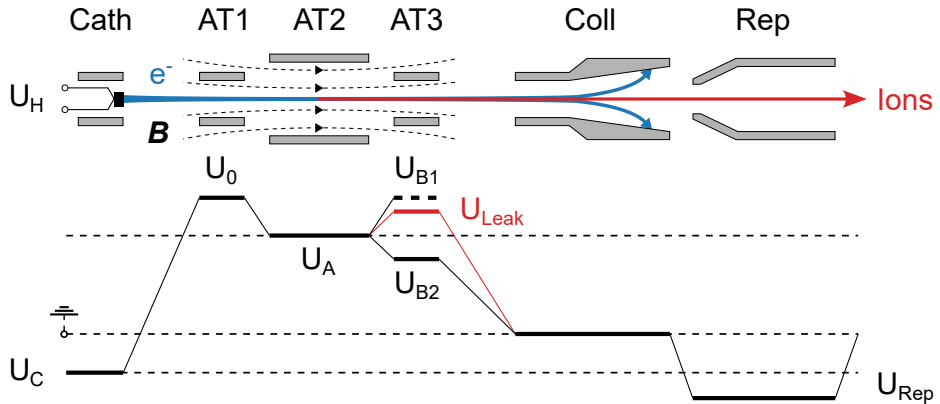


Figure 4.1: Upper row: Ion optical elements of the electron beam ion source (EBIS) of type EBIS-A from DREEBIT GmbH with cathode (Cath), axial trap electrodes (AT1-3), electron collector (Coll) and repeller electrode (Rep). Lower row: The electrostatic potentials in the EBIS. The potential differences are not to scale. The figure was drawn based on those in [63, 154].

xy-steerer as well as a velocity filter (Wien filter, WF). The repeller redirects the electrons onto the collector which is cooled with deionized water to carry away the dissipated energy of the electron beam. In the velocity filter, ions are separated by their charge-to-mass ratio using a magnetic flux density B from a permanent magnet and a tunable electric field $E = U_{WF}/d$ perpendicular to B according to

$$\frac{q}{m} = \frac{2}{U_A} \left(\frac{U_{WF}}{Bd} \right)^2, \quad (4.1)$$

where $U_A = 12.5$ kV, the magnetic flux density $B \approx 0.5$ T and the distance between the velocity-filter electrodes $d = 1.89$ mm. After passing the velocity filter, the ions are entering the main beamline.

4.1.1 Production of $^{13}\text{C}^{4+}$ from CH_4 and CO_2

In addition to $^{13}\text{CH}_4$, tests with $^{13}\text{CO}_2$ were performed to investigate the impact of a secondary element heavier than C on the production of highly charged C. In particular, the use of CO_2 is mandatory to investigate the radioactive isotope ^{14}C , which is planned in the future, due to higher exemption levels. To quantify the production, the ion current on a Faraday cup behind the velocity filter is used to monitor the ion current while a mass scan is performed. Exemplary mass spectra of both gas compounds are depicted in Fig. 4.2. The two spectra were taken in direct succession, starting with CH_4 . In the CH_4 spectrum, more residual N and O gas is present which can be reduced by repeatedly purging the source reservoir. By chance, the $^{13}\text{C}^{4+}$ peak ended up having the same height for both investigated gas compounds, as can be seen in the inset plot in Fig. 4.2. Consequently, using CH_4 to produce a beam of $^{13}\text{C}^{4+}$ ions yields

20 % more beam current if the source reservoir is properly purged. However, given the similar production rates, both gas compounds are suitable for measurements with C^{4+} .

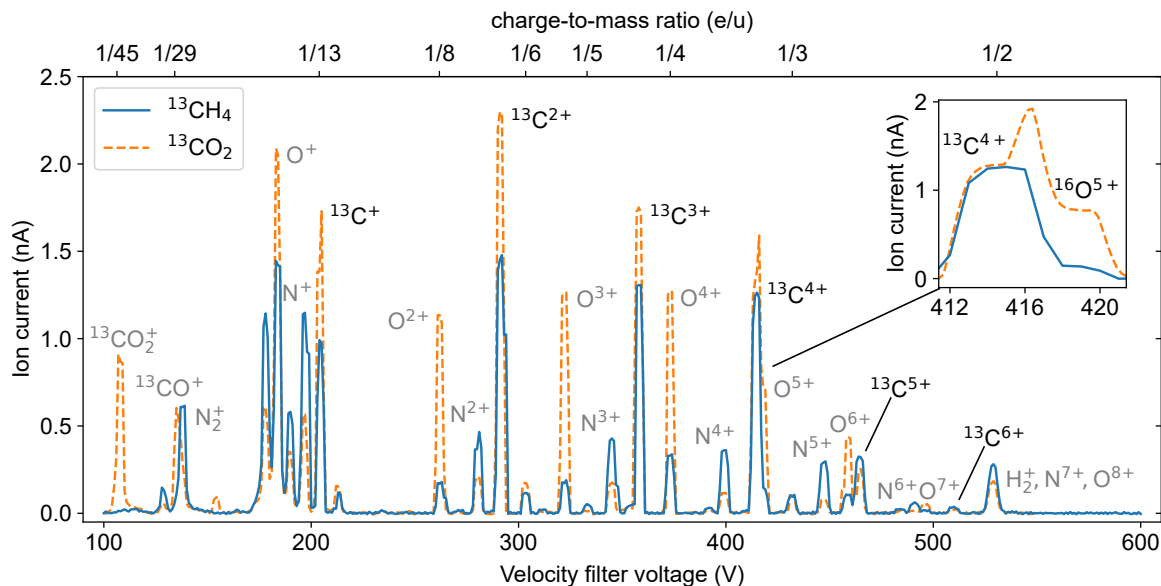


Figure 4.2: m/q -separated ion current behind the velocity filter for an EBIS operation with CH_4 and CO_2 . The 99 %-enriched $^{13}\text{CH}_4$ methane or $^{13}\text{CO}_2$ carbon-dioxide gases yield the six different charge states of ^{13}C . Residual air inside the source gives rise to small peaks of N and O. In contrast to using ^{12}C , the small peak of the bare $^{13}\text{C}^{6+}$ ion is well separated from the H_2^+ peak.

4.2 Laser spectroscopy beamline

A sketch of the entire beamline is divided into Fig. 4.3 and 4.4. Figure 4.3 shows the ion source region and the injection into the main collinear beamline. Up to three ion sources can be connected to the switchyard to allow for easy changes between ion species without mounting or dismounting ion sources. In Fig. 4.3 only those ion sources used in the present work are shown. All ion sources are at least equipped with an *einzellens* and an *xy*-steerer for beam alignment before injection into the beam-merging switchyard. Here, electrostatic benders deflect the ions by either 60° or 10° to be superposed with the laser beams. The switchyard and bender designs are based on a switchyard element used at the Extra Low ENergy Antiproton (ELENA) ring at CERN [155] and modified for the purpose of CLS including additional ports. It features five larger (DN160CF) and one smaller port (DN40CF) angled at 60° to each other. The small one is located on the main beamline axis and is equipped with a viewglas and serves as the laser entry or exit port for collinear and anticollinear laser spectroscopy, respectively. Another DN100CF port is located at an angle of 10° with respect to the beamline axis and the laser entry port. Three pairs of bending electrodes are used to transfer the ion beam between the ports. A motorized beam-diagnostic station centered on top of the switchyard can be moved

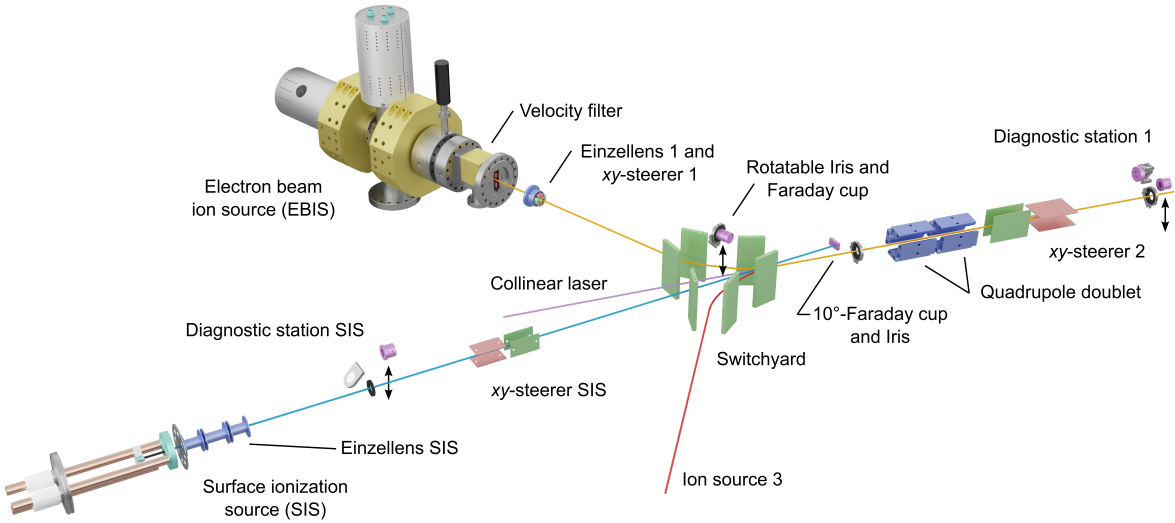


Figure 4.3: The source region of the COALA beamline up to the first diagnostic station used for beam alignment. Electrodes are colored based on their purpose, with cyan indicating those that can be floated to change the potential energy of the ions, blue indicating beam shaping elements such as einzellenses and the quadrupole doublet, green and red indicating bending elements in the x - and y -direction, respectively, magenta indicating ion detectors and yellow indicating magnets.

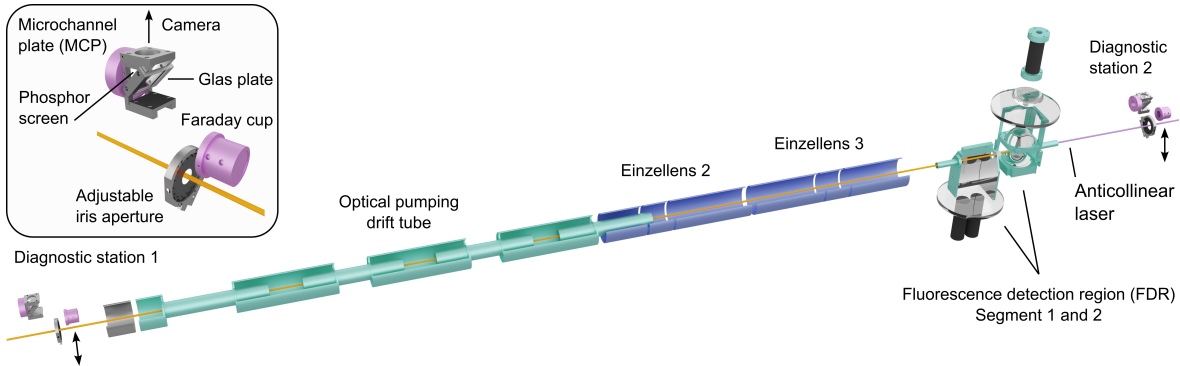


Figure 4.4: The laser spectroscopy region of the COALA beamline. Diagnostic stations are used to visualize the ion and laser beams at the start and end of the region. An optical pumping drift tube can be floated on a voltage U_{pump} . Two einzellenses can be used to focus the ion beam. The fluorescence detection region (FDR) is floated on a scan voltage U_{scan} and used to detect the fluorescence photons.

into the beamline and consists of a rotatable Faraday-cup behind a variable iris aperture. For more details about the switchyard, see [63]. The first ion optical elements after the switchyard are a quadrupole doublet to shape the ion beam and a second xy -steerer for beam alignment.

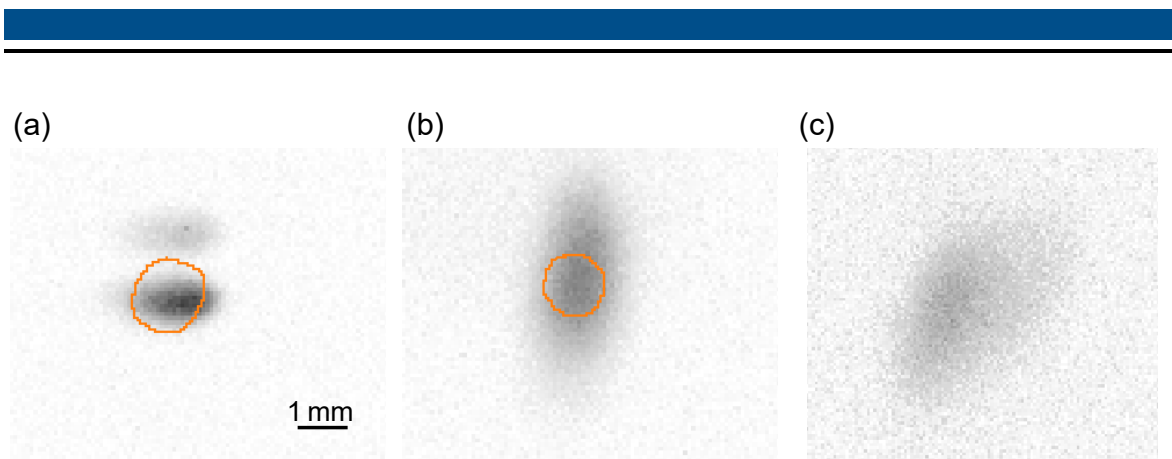


Figure 4.5: The ion beam on the microchannel plate detector (MCP) in continuous mode at (a) the first diagnostic station, (b) the second diagnostic station and (c) in pulsed mode at the second diagnostic station. The orange circles roughly correspond to the 4σ -width of the collinear laser beam and were drawn by hand during the experiment to superpose the ion and the laser beam. A second picture of the ion beam is located above the main spot in (a) and caused by a reflection from the second surface of the glass plate that guides the light towards the camera. The colors of the pictures were inverted for better visibility.

From here, the ions propagate 2.4 m without additional guiding to the fluorescence detection region (FDR), see Fig. 4.4.

Immediately behind the second xy -steerer as well as the FDR, beam diagnostic stations are located to investigate the shape and intensity of the ion beam as well as the positions of the ion and laser beams. One of the diagnostic stations is shown in the inset plot of Fig. 4.4. Each of the stations consists of the following elements in beam propagation order: A microchannel plate detector (MCP), a phosphor screen, a 45° beam splitter, a variable iris aperture and a Faraday-cup. A camera on a vacuum viewport mounted above the beam splitter records and transmits the ion and the laser beam spots on the phosphor screen. The ion beam spot is generated indirectly by the electrons emitted after ion impact from the MCP, which are accelerated towards the screen using a high voltage of 3.6 kV. In collinear geometry, the laser beam passes through the MCP and becomes also visible on the phosphor screen. This is used for ion-laser-beam alignment which is one of the main purposes of the diagnostic stations. In anticollinear geometry, however, the laser beam has to first pass the 45° beam splitter before it hits the phosphor screen. This leads to a parallel displacement of the beam and the spot can therefore not be used for beam alignment. A detailed description of the beam alignment procedure is given in Sec. 4.4.2. In Fig. 4.5, the ion beam is shown for continuous (a & b) and pulsed operation (c). Contrary to the continuous beam, the pulsed ion beam enlarges significantly over the 5 m distance from the EBIS to the MCP detector. Therefore, an additional einzellens between the first diagnostic station and the FDR was used to refocus the pulsed beam. Unfavorably, this also causes the ion beam to deflect due to a slight misalignment of that lens, significantly increasing the uncertainty of the ion-laser beam angle as the iris apertures cannot serve as reference points anymore.

4.3 Fluorescence detection region

In the fluorescence detection region (FDR), the ions are brought in resonance with the collinear or anticollinear laser beam by floating it on a voltage between -500 and 500 V. Photomultiplier tubes (PMT, Sens-Tech P25PC with UV glass) with an active diameter of 22 mm are used to detect the scattered fluorescence photons. The FDR is optimized for high detection efficiency of signal photons while suppressing unwanted photons from the laser or the environment. A computer-generated image of the FDR is shown in Fig. 4.6(a).

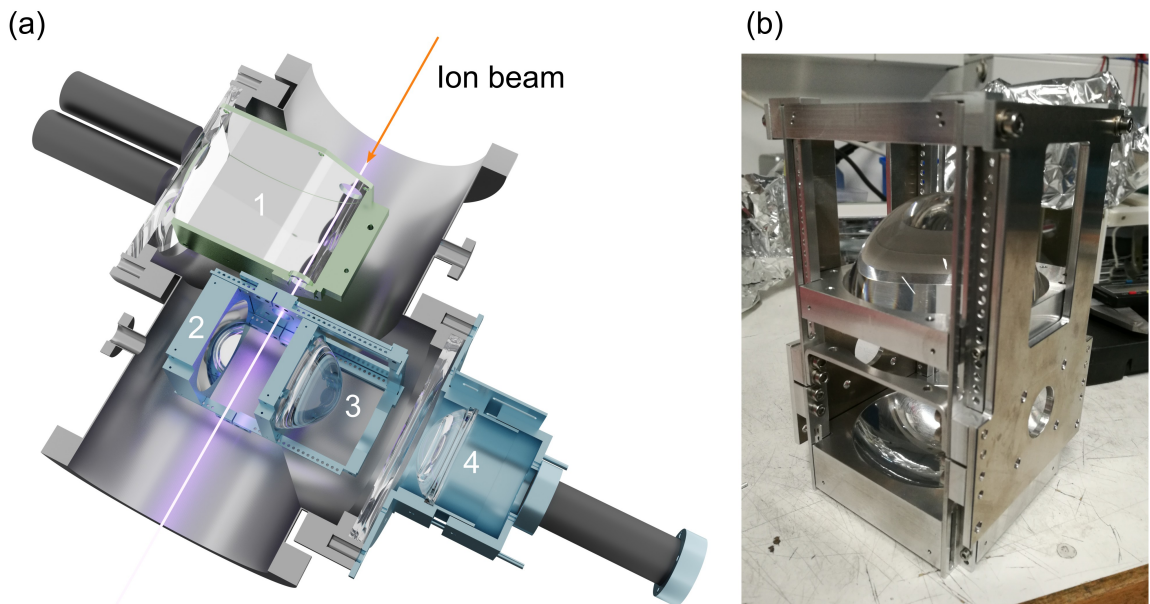


Figure 4.6: (a) Computer-generated image of the fluorescence detection region (FDR) in the (elliptical-mirror + lens)-configuration without mounting parts for better visibility. In this view, the ions enter from the top-right and pass the elliptical mirror (1) in the first FDR segment before they enter the lens-based segment that consists of a concave spherical mirror (2) as well as an aspherical (3) and a spherical lens (4). All optics have diameters of 75 mm. (b) Picture of the inner part of the new lens system. The rectangular hole was covered with low reflective, low outgassing MetalVelvet™ foil from Acktar Ltd.

The FDR of COALA comprises two consecutive, easily exchangeable segments. Within this work, three different types of segments were used. Two elliptically shaped mirrors were developed and characterized within [156, 157] and are designed to maximize the geometric detection efficiency. The elliptical mirrors have different surface properties. One version features a hand-polished bare aluminum surface which has a high reflectivity into the deep-UV. However, this version is limited by its surface smoothness. The other version is made up of MIRO® sheets (ALANOD GmbH & Co. KG), which are bent into an elliptical shape, have smooth surfaces, but drop in reflectivity towards smaller wavelengths. Both mirror systems have high fluorescence light collection efficiency but also high laser background count rates.

A new lens-based segment has been designed and built within this work to complement the elliptical mirror system. The properties of the lens system and a comparison of both systems is given in the following section.

4.3.1 Lens-based FDR

Assembly The new lens-based FDR comprises two plano-convex UV-fused silica lenses and a concave aluminum mirror. Both, the first lens and the mirror are situated inside the vacuum and designed to efficiently collimate the light emitted in their focal points towards the vacuum viewport. The outer lens concentrates the collimated light onto the photo cathode of the PMT. The optics have a standard diameter of 75 mm. The hand-polished reflective surface of the mirror has a curvature radius of 45 mm and is positioned at the same distance from the beam axis. It was manufactured by the mechanical workshop of the Institut for nuclear physics at TU Darmstadt. The custom made inner lens (EKSMA optics) has an aspheric surface to correct for the spherical aperture. It has an effective focal length of 60 mm at 588 nm, corresponding to a back focal length of 31.7 mm from the flat surface, and a center thickness of 41.3 mm. The aspheric lens equation and the corresponding parameters in units of mm describing the curved surface are given by

$$f(x) = \frac{x^2}{r + \sqrt{r^2 - (1+k)x^2}} + a_4x^4 + a_6x^6 + a_8x^8 + a_{10}x^{10}, \quad (4.2)$$

$$r = 27.5, \quad k = -1.099,$$

$$\{a_4, \dots, a_{10}\} = \{3.24294 \cdot 10^{-6}, 1.22320 \cdot 10^{-9}, -3.30436 \cdot 10^{-13}, 3.90447 \cdot 10^{-16}\}.$$

The outer spherical lens has a curvature radius of 41.4 mm, a center thickness of 29.9 mm and an effective focal length of 90.3 mm (LA4384 from Thorlabs). The lens-based FDR segment can be optimized for different wavelengths by continuously adjusting the distance z_{lens} between the inner lens and the beam axis as well as the distance between the PMT and the outer lens. The latter is changed by varying the position z_{PMT} of the PMT with respect to the beam axis.

Configuration space The lens-based FDR segment was planned and simulated with the ray-tracing program *FRED* (Photon Engineering) to test its geometric efficiency. The geometric efficiency used to characterize the FDR is defined in the raytracing simulations as

$$\text{Geometric efficiency} := \frac{\text{Photonic power impinging active PMT surface}}{\text{Photonic power emitted from the source volume}} \quad (4.3)$$

In Fig. 4.7, the geometric efficiency of the segment is plotted against the two available degrees of freedom for the wavelengths 408 nm, 227.6 nm and 190 nm. The first two wavelengths were chosen since they were used in the experiments described in this work, whereas the latter is both, the transition wavelength of helium-like N^{5+} and close to the end of the transmittance curve of UV-fused silica. The simulations neglect internal absorption and scattering of the



Figure 4.7: Geometric efficiency in dependence of the distance of the inner lens (x -axis) and the photomultiplier tube (PMT) (y -axis) relative to the beam axis for the wavelengths (a) 408 nm (b) 227.6 nm and (c) 190 nm determined using raytracing simulations. The dashed vertical and horizontal lines mark the back focal length of the inner lens and the focus point of the outer lens, respectively. The red dots mark the configuration that was used in the measurements presented in this work for the respective wavelength. The displayed x -ticks are the available discrete positions on the lens positioning rail.

lenses. Although this leads to a slight overestimation of the geometric efficiency in the case of 190-nm light, it simplifies the interpretation of the simulations since the internal transmittances of the lenses strongly depend on the purity of the fused silica and already varies for the optics used within this work. The reflectivity of the aluminum mirror was estimated based on reflectivity measurements in [157] and by comparing the fluorescence spectra recorded with the elliptical mirror and the lens-based system. For the aforementioned wavelengths, reflectivities of 80 %, 60 % and 50 % were assumed, respectively. Parts of the FDR segment which are not part of the optical system were not included in the simulations since those would add additional assumptions about the optical properties of the used materials but also increase the simulation time. The light source in the simulation was defined as a cylindrical volume with a length of 80 mm, corresponding to the length of each FDR segment used at COALA, and a radius of 0.7 mm which is the usual size of the laser beam, see also Sec. 4.4.3. A total number of 50 000 rays were created per $(z_{\text{lens}}, z_{\text{PMT}})$ value at random positions inside the cylindrical volume according to a uniform distribution. The initial propagation directions of the rays were randomly generated according to an isotropic distribution at their points of origin.

The results of the simulations show quite a large tolerance regarding the positioning of the variable elements. The inner lens can deviate up to 4 mm from the optimal position to still get 90 % of the maximum geometric efficiency. The optimal position corresponds to the focal length of the lens, as expected. The efficiency is even more insensitive to the position of the

PMT relative to the outer lens due to the large active surface of the PMT compared to the size of the focal point of the lens. Deviations of 10 mm from the optimal position still yield 90 % of the maximum efficiency. The optimal position of the PMT is substantially off from the focus point of the outer lens. This can be explained with light that is not perfectly collimated by the inner lens and, therefore, falls off in intensity with increasing distance from the outer lens. The geometric efficiency slightly increases towards shorter wavelength due to the increasing numerical aperture of the inner lens. The position of the inner lens was set very close to the simulated optimum for 227.6 nm in the experiment as indicated by the red dot in Fig. 4.7(b). For measurements with Sr^+ at 408 nm, the lens position was not changed.

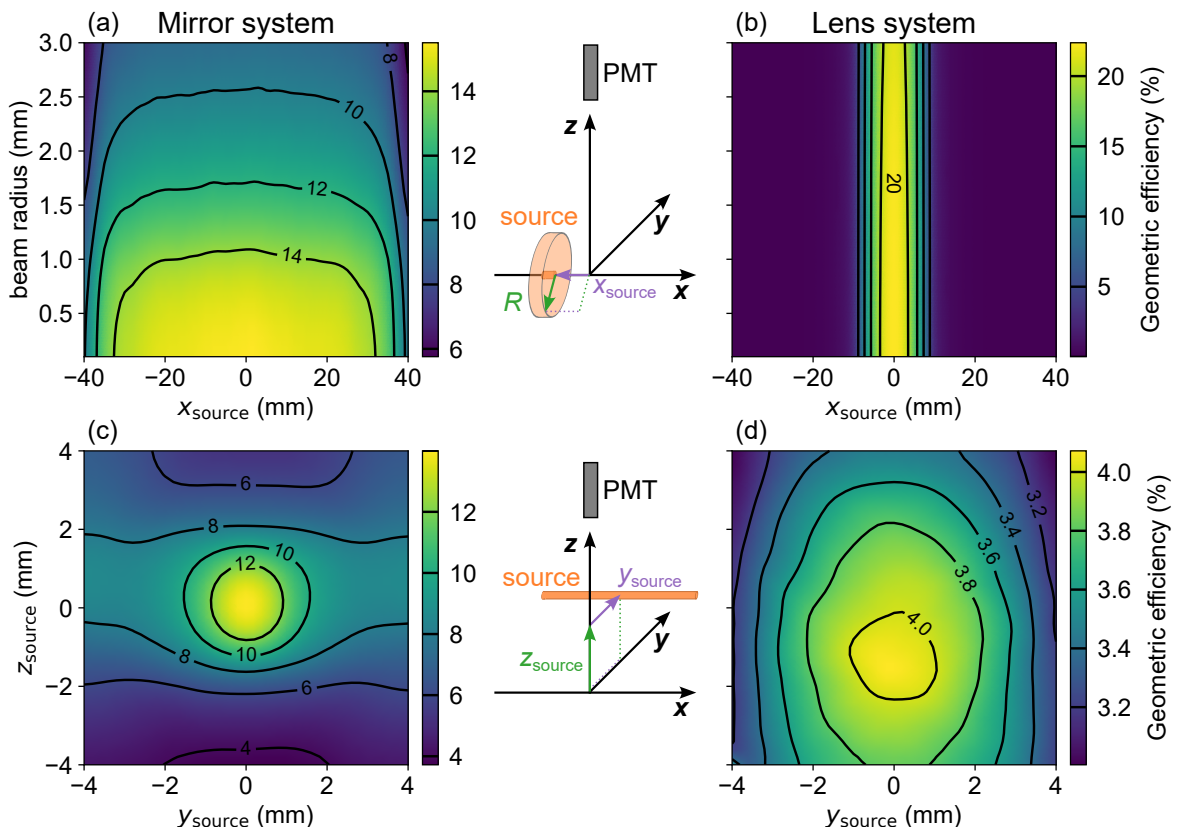


Figure 4.8: Geometric efficiency in dependence of the emission position along the beam axis and the source radius for the elliptical mirror system (a) and the lens-based system (b). (c & d) show the geometric efficiency in dependence of transversal shifts of the source, for elliptical mirror and lens-based system, respectively. The z -axis coincides with the optical axis of the lens system. The setup of the simulation is indicated in the coordinate systems in the center. Light rays are emitted randomly from uniformly distributed positions inside a cylindrical volume and into isotropically distributed directions with respect to their points of origin. This simulation was performed for a wavelength of 227.6 nm.

Spatial tolerance Additional simulations were performed to test and compare the stability of the geometric efficiency of both the elliptical mirror and the lens-based system against the variation of experimental parameters at a wavelength of 227.6 nm. Figure 4.8 illustrates the variation of the cylindrical source radius, the emission position along the beam axis as well as its transversal position. To determine the emission position, the cylindrical light source was divided into 1-mm sections. The elliptical mirror exhibits a geometric efficiency of approximately 15 % almost along the entire covered beam axis but drops in efficiency to 10 % for larger beam radii above 2 mm. The lens system shows a constant efficiency of more than 20 % for beam radii below 3 mm. However, it drops to 10 % at a distance from the focal point of the lens of 7 mm on the beam axis. Figure 4.8(c-d) shows a comparable concentric efficiency pattern for both FDR segments when the light source is shifted off-axis. However, the lens system is less sensitive to these shifts.

Solid angle of detection The emission pattern of a fluorescing atomic system is in general not isotropic, in fact, it can even correspond to the classical dipole radiation pattern, completely suppressing photon emission towards the oscillation direction of the laser field. Therefore, it is of interest to specify the emission-angle-dependent geometric efficiency of the FDR. For a quantitative analysis of quantum interference effects which can appear in fluorescence spectra

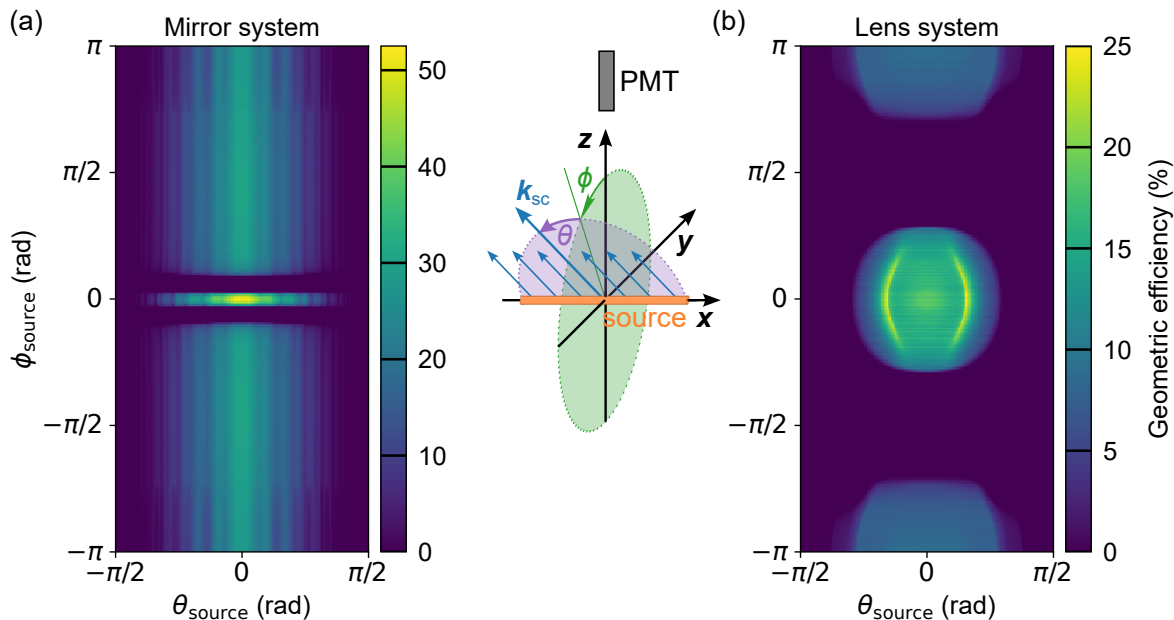


Figure 4.9: Geometric efficiency in dependence of the emission angle from a cylindrical fluorescence source for (a) the elliptical mirror and (b) the lens-based segment. The coordinate system and parameterization of the angles used in the graphs is shown in the center. For a specific pair of angles (θ, ϕ) , light rays are emitted randomly from uniformly distributed positions inside the source volume into the direction k_{sc} .

with close lying intermediate excited atomic states it is essential to predict the asymmetric fluorescence spectrum. Results of raytracing simulations performed with 227.6 nm light by iterating through the emission angles (θ, ϕ) in discrete steps are shown in Fig. 4.9. The light is emitted from randomly distributed positions inside a cylindrical source volume that emulates the ion beam, as depicted in the coordinate system in Fig. 4.9. The resulting angular detection patterns clearly show the unique geometries of the two distinct segments. In either case, a brighter central spot originates from emitted light which is reaching the PMT directly without being reflected by a mirror surface. This spot is increased in the elliptical-mirror segment in θ due to the flat mirrors orthogonal to the beam axis and in the lens-based segment in θ and ϕ due to the large inner condenser lens. The elliptically curved mirror surfaces extend the central pattern in ϕ , covering a large portion of the full solid angle. The concave mirror in the lens-based segment reflects light emitted from the focal point of the lens back into its origin, essentially copying the lens system with reduced efficiency.

Signal-to-noise ratio The maximum geometric efficiencies of both FDR segments can be compared directly to the signal ratio between experimental spectra. While a 1 to 7 times higher signal rate was found experimentally for the elliptical mirror at 227.6 nm, the lens-system excels

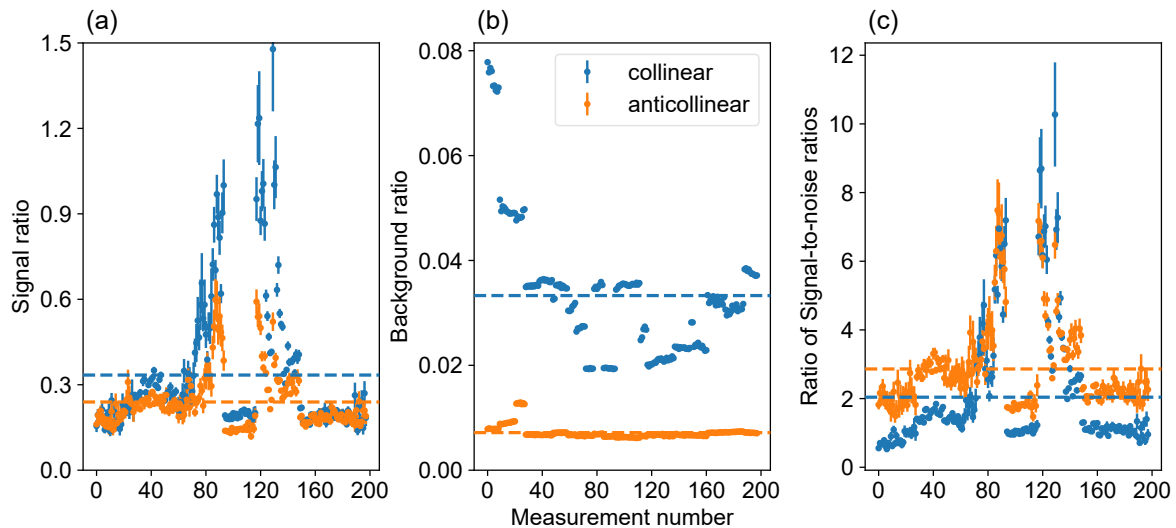


Figure 4.10: Comparison of the lens-based and the elliptical-mirror segments of the FDR. Plotted is the ratio (lens/mirror) of the following important parameters: (a) signal, (b) laser background, and (c) signal-to-noise ratio. The data is taken from the $^{13}\text{C}^{4+}$ measurements described in Sec. 5.2.2 when both segments were in use simultaneously. The colors indicate collinear (blue) and anticollinear (orange) measurements. The plotted error bars are only the statistical uncertainties of the fits and do not necessarily represent the actual variations during any given series of measurements. The horizontal lines indicate the unweighted mean values of the data.

at suppressing laser background light. Typical off-resonance count rates with a laser power of 0.5 mW were 400 kHz and 10 kHz in collinear and 150 kHz and 1 kHz in anticollinear geometry, respectively. This is also confirmed by straylight simulations which yield a straylight detection efficiency of 3.8 % for the elliptical-mirror and 0.028 % for the lens-system. A comparison of the ratio between lens-based and elliptical-mirror segment for the signal, background as well as the signal-to-noise ratio for collinear and anticollinear geometry is given in Fig. 4.10. The shown data includes all non-modulated (see Sec. 5.1.2) measurements with $^{13}\text{C}^{4+}$ that were recorded with the lens-based system in place and for which both segments passed the filtering in the analysis process, as described in Sec. 5.2.2. In 90 % of the measurements, the fluorescence spectra recorded with the lens-based segment showed a better signal-to-noise ratio than those recorded with the elliptical-mirror segment.

Conclusion The lens-based FDR segment was characterized using raytracing simulations and extensively tested in the course of the measurements with $^{13}\text{C}^{4+}$. While the total geometric efficiency to detect fluorescence light from a collinear beam is generally lower for the lens-based system compared with the elliptical mirror system, the strong laser background suppression yields a higher signal-to-noise ratio for 227.6 nm light. The property to achieve similar signal-to-noise ratios as the elliptical mirror system for two orders of magnitude lower count rates at the same laser power is essential to prevent saturation of the PMTs in experiments where a large laser power cannot be avoided. The uv-fused silica lenses and available degrees of freedom ensure optimal detection efficiency from 190 nm to the near-infrared. The system has a tolerance of several mm regarding ion/laser-beam position and size such that elaborate adjustment procedures are not required. The sensitivity to the angular emission pattern of photons from the ion beam enables an investigation and a utilization of quantum interference (QI) effects which are almost completely suppressed in the elliptical mirror system. The sensitivity to QI effects is demonstrated with the fluorescence spectrum of $^{87}\text{Sr}^+$ in Sec. A.1.

4.4 Laser setup

The experiments described in the next chapter require two frequency-stabilized laser beams with well-known frequencies. If collinear laser spectroscopy is performed, the laser beam position is additionally stabilized. This section outlines the laser setup from production until alignment with the ion beam.

4.4.1 Laser beam production

The laser setup is depicted in Fig. 4.11. Two continuous-wave laser beams, to be used in collinear and anticollinear geometry, were generated using solid-state Ti:sapphire lasers (Matisse 2 TS from Sirah Lasertechnik) that are optically pumped by frequency-doubled, diode-pumped Nd:YVO₄ lasers (Millenia eV from MKS-Spectra-Physics). The pump lasers provide up to 20 W and 25 W of continuous-wave light at a wavelength of 532 nm. The Ti:sapphire lasers can be set to arbitrary wavelengths between 662 nm and 1050 nm by altering their resonators which consist of multiple frequency-selective elements. Optical reference cavities are used for

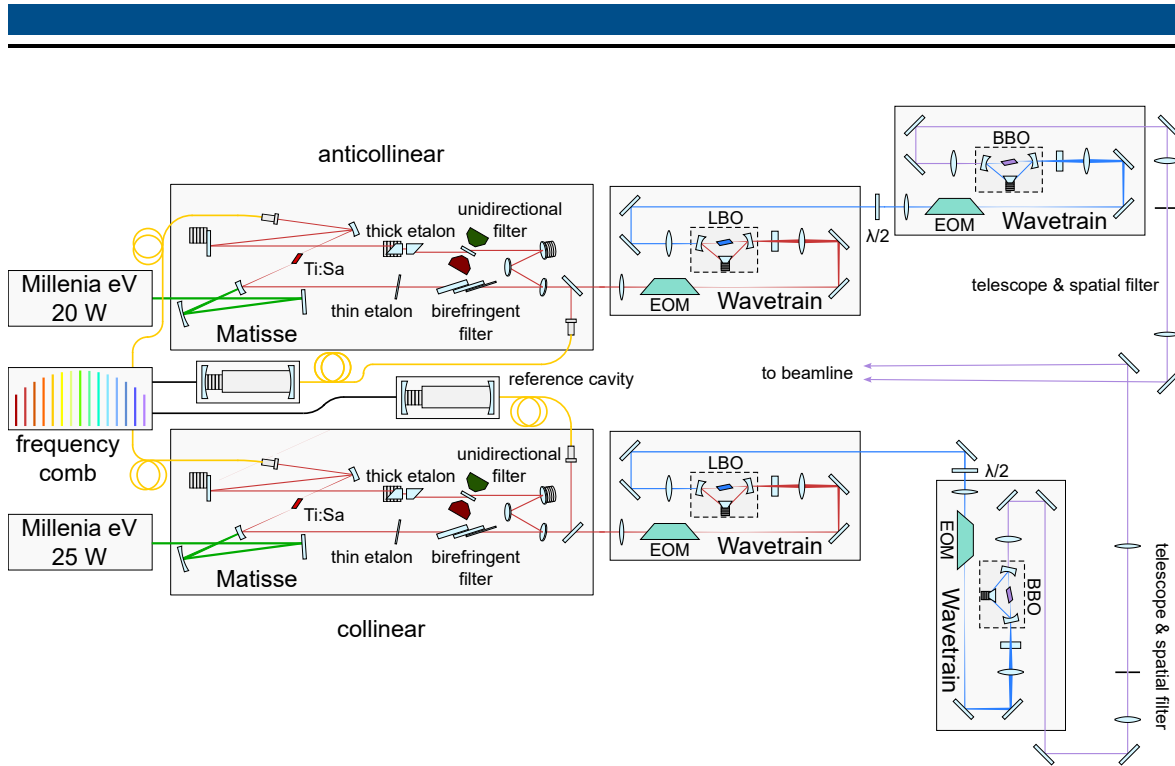


Figure 4.11: Sketch of the laser setup in the laser laboratory. Two identical setups are used to produce laser light that is used in collinear and anticollinear geometry. For each case, the laser light produced by an Nd:YVO₄ (532 nm) pumped Ti:sapphire laser is frequency-doubled twice and sent to the beamline laboratory. The frequencies are measured and stabilized using a frequency comb. The sketch was drawn based on the manufacturer drawings and [153].

long-term frequency stability. For the measurements with ¹³C⁴⁺, the Ti:sapphire lasers were operated between 906 nm and 914 nm. The infrared light was then frequency-doubled twice using a lithium triborate crystal (LBO) and a beta barium borate crystal (BBO) to wavelengths between 226.5 nm and 228.5 nm (Wavetrain 2 from Sirah Lasertechnik). A telescope composed of lenses with focal lengths of 75 mm and 200 mm was used together with a 35-μm-pinhole to produce a Gaussian beam profile with a diameter below 1 mm at the beamline. For the collinear beam, the first telescope was used to enlarge the laser beam due to the approximately three times longer beam path. Then a second telescope, located directly in front of the beamline and consisting of two identical lenses with focal lengths of 50 mm, was used to refocus the beam into the beamline [158].

The laser frequencies were simultaneously measured and stabilized with a frequency comb (FC1500 from Menlo Systems). For this, a sample of the infrared light from each Ti:sapphire laser was coupled into the frequency comb and mixed with the pulsed light of the comb laser. Measured with fast photodiodes, the difference frequency of the mixed light gives rise to a beat signal for each spectroscopy laser which was stabilized to 60 MHz by controlling the resonator length of the reference cavity used for short-term stabilization of the Ti:sapphire laser. To obtain the absolute frequencies of the lasers, the frequency of the comb mode that produces

the 60 MHz signal needs to be determined. For this, the laser frequencies were measured in parallel with a wavelength meter (WSU30 from HighFinesse) to an accuracy of 30 MHz which allows an unambiguous assignment of the beat signal to the correct comb mode. Using this stabilization method, a standard deviation ranging from 0.2 MHz to 1 MHz was achieved for the stabilized quadrupled frequency.

4.4.2 Laser beam position stabilization

The long path of the collinear laser beam leads to a trembling motion at the position of the FDR due to air movement and vibrating optical elements. This causes unwanted structures in the laser background of the fluorescence spectrum [63], see also Fig. 5.4(a). A reduction of this effect is particularly important for the measurements with $^{13}\text{C}^{4+}$ due to its hyperfine structure splitting which causes the smallest resonance signals to be a factor of three smaller compared with the smallest resonance in $^{12}\text{C}^{4+}$. A laser beam position stabilization system (MRC-systems) has been set up to reduce this effect and to counteract a drift of the laser beam [159]. The setup of the laser beams in front of the entrance windows to the beamline are shown in Fig. 4.12.

A comparison of the stability of the laser beam on the second detector with and without the second stabilization stage active is shown in Fig. 4.13. The stabilization system returns the position coordinates and the intensity of the laser beam as voltages which can be transformed into length units with

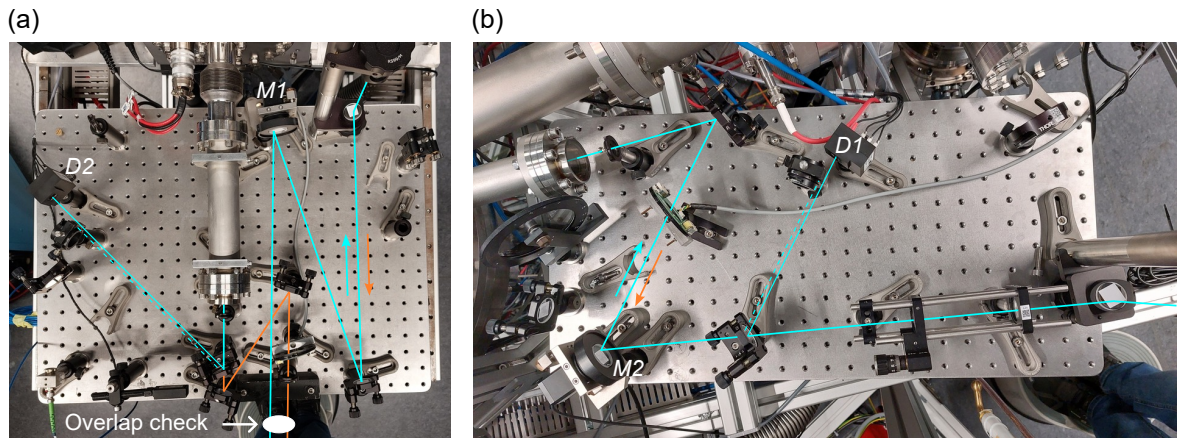


Figure 4.12: The path of the collinear (cyan) and anticollinear (orange) laser beam in the beamline laboratory. (a) The site of the coupling window for the anticollinear laser beam located next to the laser laboratory. The piezo-actuated mirror $M1$ is used to stabilize the collinear laser beam to detector $D1$ located in (b), the site of the collinear coupling window. The second piezo-actuated mirror $M2$ is used for the stabilization to detector $D2$. Both laser beams follow the complete path and were superposed by eye at the marked position where both beams enter and leave the beamline area.

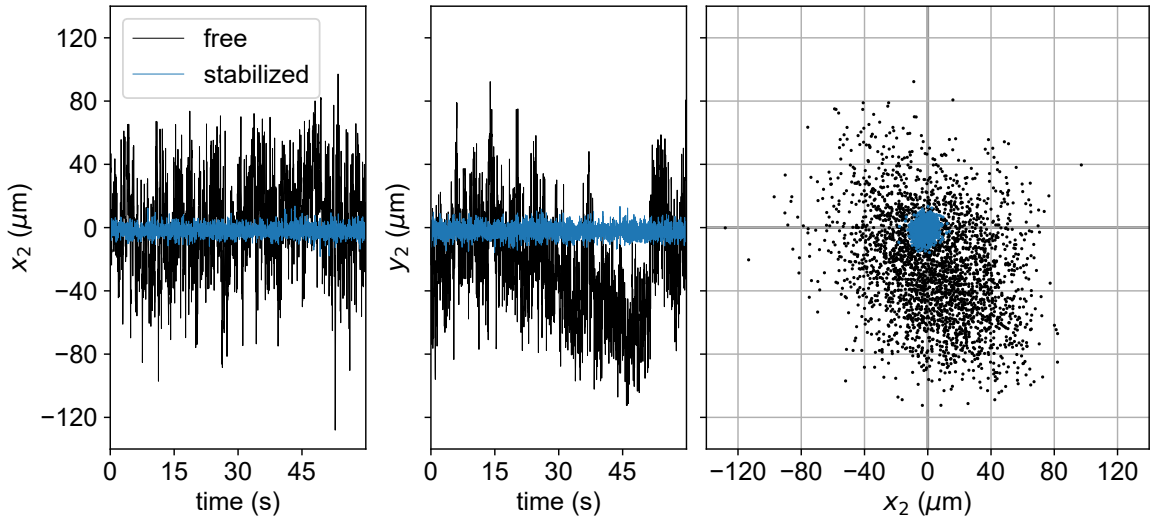


Figure 4.13: The position of the collinear laser beam on the second detector of the position stabilization system during one minute of recording time. Enabling the second stabilization stage significantly reduces the scattering of the data and eliminates all slow drifts.

$$r_{x/y} = \frac{w}{\pi I} U_{x/y}, \quad (4.4)$$

where w is the 2σ -width of the beam profile at the detector that can be calculated from the results in Sec. 4.4.3, U is the position in volts and I is the intensity in volts. The results show a significant improvement in stability when the second stage is active, reducing the standard deviation of the position of the collinear laser beam on the second detector from $34 \mu\text{m}$ to $3.7 \mu\text{m}$. In addition to the reduction of the fast trembling motion of the laser beam, slow changes on a time scale of seconds, as visible in the y -coordinates in Fig. 4.13, are eliminated completely.

4.4.3 Laser- and ion-beam alignment

Well aligned ion and laser beams are required to achieve the targeted precision. The sizes of the cross sections as well as the positions and angles of the laser beams in the FDR need to be matched. The size of the cross section of a laser beam is the most challenging to adjust as already small translations of the focusing lens lead to large changes in the beamline and can also lead to positional variations. However, its effect on transition frequency measurements is smaller and once set, it is also sturdier than the location of the beam. The cross sections of the laser beams have been measured with a beam profiler (Thorlabs BC106N-UV) and adjusted to be of the same size at the position of the FDR before the start of the measurement campaign. In Fig. 4.14, the laser beam radii are plotted as functions of the position in the beamline. The uncertainties

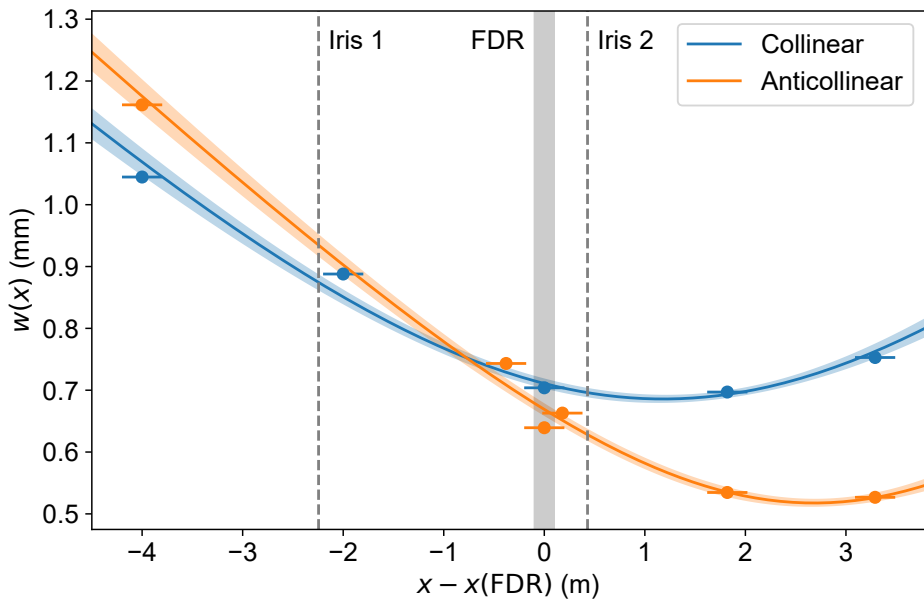


Figure 4.14: The radii w ($= 2\sigma$ of a Gaussian) of the collinear and anticollinear laser beams along their paths as set up before the measurements. The beam profiles were measured with a CCD-camera and adjusted to have approximately the same size inside the FDR. The positions of the FDR and the variable iris apertures are marked in grey.

in the plot are only statistical uncertainties from the beam profile measurements. At the FDR, the laser beams have sizes of 0.706(8) mm in collinear and 0.670(12) mm in anticollinear geometry. The divergences of the beams are comparable. However, the collinear laser beam deviated from a perfect Gaussian beam, exhibiting an M^2 value of 1.5(1). A repetition of the beam profile measurements after the ^{13}C measurement campaign indicates that unsuccessful efforts undertaken to fix the beam profile changed the focus of the collinear laser beam at some point such that the beam diameter at the FDR was then 0.470(2) mm. However, this has a minor influence on the determination of transition frequencies. Although the laser beam profile contributes to the main systematic uncertainty which originates from the spatial distribution of ion velocities, it is only a second order effect as a linear relation between the velocity and the position of an ion in the beam leads to no systematic shift for symmetric laser beam profiles. A detailed discussion of this contribution is given in Sec. 5.2.3.

The locations of the laser beams are not as stable as the focuses of the beams due to spatial drifts of the pump lasers, in particular after cold starts. However, the optimal alignment can be restored quickly. The following alignment procedure was repeated at the beginning of each measurement day for all $^{13}\text{C}^{4+}$ measurements shown in this work, excluding necessary preceding steps in the laser laboratory:

1. Optimize the laser power of the collinear laser beam through the beamline using maximally closed iris apertures.

2. Optimize the laser background of the collinear laser beam by translating and tilting the beam and setting the size of all iris apertures in collinear geometry. The laser power is monitored and kept at the maximum.
3. Center the spot of the collinear laser beam on the detectors of the beam stabilization system.
4. Adjust the position of the anticollinear beam to that of the collinear beam at its entrance to and exit from the beamline laboratory (beam path of 14 m).
5. Optimize the size of all iris apertures in anticollinear geometry for minimal background counts at the PMTs.
6. Adjust the positions of the ion beam on the two MCP-detectors (beam path of 2.6 m) using the *xy*-steerers before and after the switchyard.
7. *(Optional)* Float the FDR to the resonance position and optimize the count rate using the *xy*-steerers before and after the switchyard.

5 Collinear laser spectroscopy in $^{13}\text{C}^{4+}$

The frequencies of the $1s2s\,{}^3\text{S}_1 \rightarrow 1s2p\,{}^3\text{P}_{0,1,2}$ electronic transitions in helium-like $^{13}\text{C}^{4+}$ were measured with collinear laser spectroscopy (CLS). The isotope shift, the hyperfine structure constants and the shift of the nuclear charge radius relative to ^{12}C were determined. This chapter outlines the complete process, from data collection to the determination of the nuclear charge radius of ^{13}C .

5.1 Fluorescence spectra of $^{13}\text{C}^{4+}$

Spectroscopy data is taken with the Python/Labview software program *Tilda*, which is based on a field programmable gate array (FPGA) [126]. An 18-bit digital-to-analog converter (DAC) is controlled by the FPGA to produce a low voltage ranging from -10 to 10 V which is amplified by a factor of $50.293(1)$ before being applied to the fluorescence detection region (FDR). The modified ion velocity changes the frequency of the laser in the rest-frame of the ions, as explained in Sec. 2.3.2. At each voltage step, signal pulses from the photomultiplier tubes (PMT) were counted during a dwell time of 1 ms. After a scan, consisting typically of 61 steps, the scan is repeated in opposite direction. The number of required scans per measurement

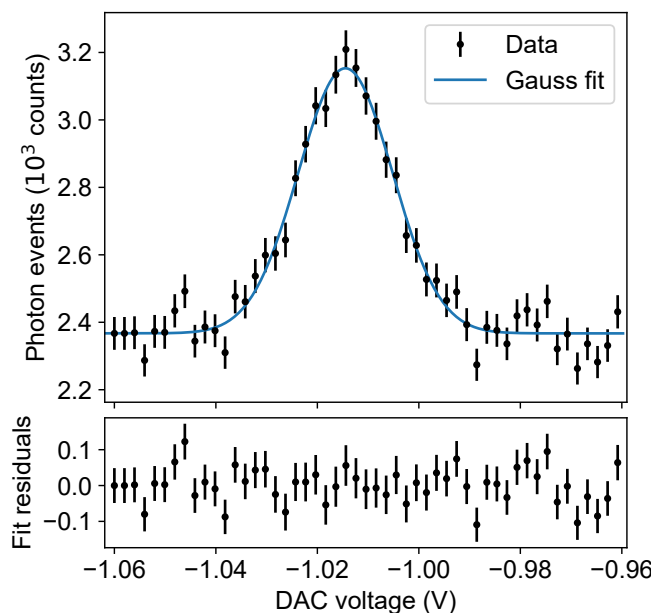


Figure 5.1: Standard fluorescence spectrum of the $F = 3/2 \rightarrow F' = 1/2$ component in the $1s2s\,{}^3\text{S}_1 \rightarrow 1s2p\,{}^3\text{P}_0$ transition of $^{13}\text{C}^{4+}$ recorded with the digital-to-analog converter (DAC) of *Tilda*. The x-axis shows the voltage output of the DAC which is amplified by a factor of $50.293(1)$. A Gaussian was fitted to the data. The residuals show the difference between the data and the fit.

varied between 1 000 and 10 000 depending on the transition strength and the laser geometry. The final fluorescence spectrum is obtained by summing up the photon events assigned to the same scan voltage. A standard fluorescence spectrum in dependence of the DAC voltage is depicted in Fig. 5.1. To extract a resonance frequency, it is necessary to calculate the Doppler shift from the acceleration voltage of the ions. Section 5.1.1 describes how the scan voltage that is applied to the FDR is calibrated.

5.1.1 Calibration of the Doppler shift

When passing the FDR, the ions may experience a potential that can deviate from the applied scan voltage, *e.g.*, due to contact voltages relative to the ion source or field penetration into the FDR. As shown in Eq. (2.62), the knowledge of the exact ion velocity and hence,

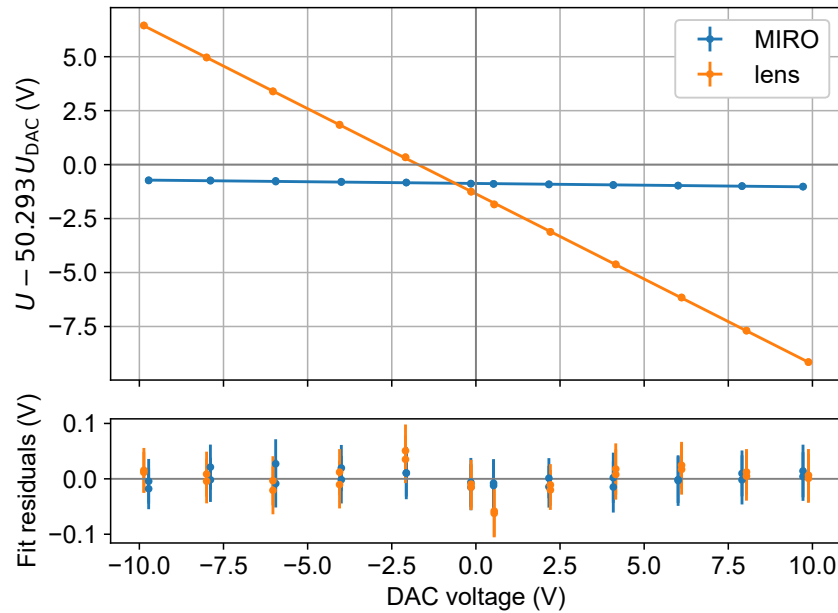


Figure 5.2: Calibration of the voltage potential in the FDR. The vertical axis displays the voltage determined from spectroscopic measurements relative to the expected total acceleration voltage for the elliptical mirror system with MIRO® sheets (blue) and the lens system (orange). The horizontal axis displays the DAC-voltages at which the resonances appeared. Note that the vertical axis offsets stem from contact voltages and the unknown initial potential in the ion source. The linear fit was carried out using the algorithm described in [140] and considers the uncertainties of both axes. The final voltage amplification factors of the two systems are 50.277(1) for the MIRO® and 49.504(1) for the lens system. The deviations from the amplification factor measured directly with a voltmeter of 50.293(1) originate from electric field penetrations, see text.

the acceleration voltage, is not required in the collinear-anticollinear approach. However, when performing Doppler-tuning, knowing the potential difference between collinear and anticollinear measurements is substantial to ensure $\beta_c = \beta_a$. To determine the true FDR potential for calculating the Doppler shift, an effective amplification factor of the voltage amplifier was determined for the different segments of the FDR. For this, frequency measurements of a single transition in $^{169}\text{Tm}^+$, produced in a surface ionization source, have been carried out at different DAC voltages by adjusting the laser frequency [160]. By comparing the shift of the resonance peak in voltage space with the laser frequency change, the voltage amplification factor can be corrected. In order to calculate the actual voltage potential spectroscopically, the absolute transition frequency was determined using quasi-simultaneous (anti-) collinear laser spectroscopy beforehand.

There are three distinct geometries used in the FDR as detailed in Sec. 4.3: A hand-polished elliptic aluminium mirror with a metal mesh closing its open side, an elliptic mirror of aluminium MIRO® sheets but without a metal mesh [156, 157], and a lens system. The hand-polished mirror with the mesh was not calibrated, as it constitutes a full metal housing and, hence, does not distort the voltage potential. The lens system includes a metal-mesh directly in front of the dielectric lens but the sides of the mounting scaffold were left open during the measurements, causing a significant field penetration. Figure 5.2 displays the results of the scan potential calibration. While the amplification factor in the mirror system deviates only slightly from the expected value, the lens system exhibits a noticeable difference. Nonetheless, this should not pose a problem as long as the correct amplification factor is known. The corresponding systematic uncertainty contribution can be calculated by using the uncertainties of the determined amplification factors of 50.277(1) (MIRO®) and 49.504(1) (lens) and the maximum distance between the collinear and anticollinear peak in the amplified-voltage space, which was $\delta U = 0.3$ V. This implies that any systematic error arising from this effect cannot exceed 2 kHz.

5.1.2 Background-free laser spectroscopy

The motion of the laser beam affects the background rate and generates structures in the count rate. When fitted, these lead to shifts in the determined resonance centers, which cannot be accounted for in the lineshape model. The collinear geometry is predominantly affected due to the 16-m long beam path through air. To reduce the motion of the laser beam, a beam position stabilization system was installed, as described in Sec. 4.4.2. Additionally, small dwell times of only 1 ms were used to average out the laser background. However, these methods were not always sufficient to eliminate the background structures completely. As a solution, a measurement scheme was developed that inherently produces a flat laser background [159, 161]. Examples of fluorescence spectra taken with the usual method and the special measurement scheme are shown in Fig. 5.3.

For the background-free spectra, a function generator was used to produce a square-wave potential modulating the ground potential of the voltage amplifier that applies the scan voltage to the FDR. By splitting each photo-multiplier tube (PMT) into two channels which are gated using a TTL-signal synchronized to the modulated ground potential, the fluorescence spectrum is simultaneously recorded at two different scan voltages. If the fluctuations in the laser



Figure 5.3: The three types of spectra used within this work. (a) shows a standard fluorescence spectrum with no voltage modulation which was used for most of the measurements. (b) shows a background-free fluorescence spectrum produced with a square-wave potential alternating between 0 V and 4 V corresponding to a frequency change of 0.6 GHz. (c) shows a background-free dispersion fluorescence spectrum with a square-wave potential alternating between -0.25 V and 0.25 V. For the dispersion spectra, the derivative of a Gaussian was used as the fit model. The spectra shown here were recorded using the collinear laser geometry.

background are slower than the modulation frequency of the square-wave potential, the laser background will always be identical in the two channels of each PMT. Thus, by subtracting the signals from each other, any background structures can be removed. For the measurements conducted within this work to determine the transition frequencies of $^{13}\text{C}^{4+}$, a modulation frequency of 769 Hz was chosen which corresponds to a period of 1.3 ms. Even though the period is longer than the dwell time, any beat averages out after the minimum number of 1 000 voltage scan cycles.

The two voltages that define the square wave can be chosen arbitrarily to produce a background-free spectrum. Two distinct cases were used within this work. In the first case, one voltage is set to zero, which produces a typical resonance spectrum and the second voltage is set sufficiently high to not produce any signal events in the given scan range. This yields a normal, but background-free resonance as shown in Fig. 5.3(b). In the second case, both voltages are equally shifted from zero by only a small amplitude of 0.25 V but with opposite signs. This yields a dispersion spectrum as visible in Fig. 5.3(c) since it corresponds essentially to an experimentally taken difference quotient. The chosen voltage amplitude is small enough to justify fitting the derivative of a Gaussian. The resonance position is determined by using the central zeropoint of the derivative. Note that spectra recorded with the voltage modulation

lose a factor of two in signal-to-noise ratio (SNR) since half of the signal and background are discarded (first factor of $\sqrt{2}$) and the subtraction increases the noise (second factor of $\sqrt{2}$). Fits to all three types of spectra show similar and featureless scattering of the residuals.

5.1.3 Test of saturation spectroscopy

The new background-free laser spectroscopy technique introduced in Sec. 5.1.2 enables the use of large dwell times by eliminating fluctuations in the laser background. This is essential if the laser frequency needs to be scanned directly as the used Ti:sapphire laser takes about 200 ms to set the next frequency value. Directly scanning the laser frequency enables the utilization of saturation spectroscopy to potentially improve the precision of the extracted resonance frequencies of C^{4+} . A first attempt of performing collinear saturation spectroscopy was undertaken with ^{12}C prior to the measurements with ^{13}C presented in this work [159].

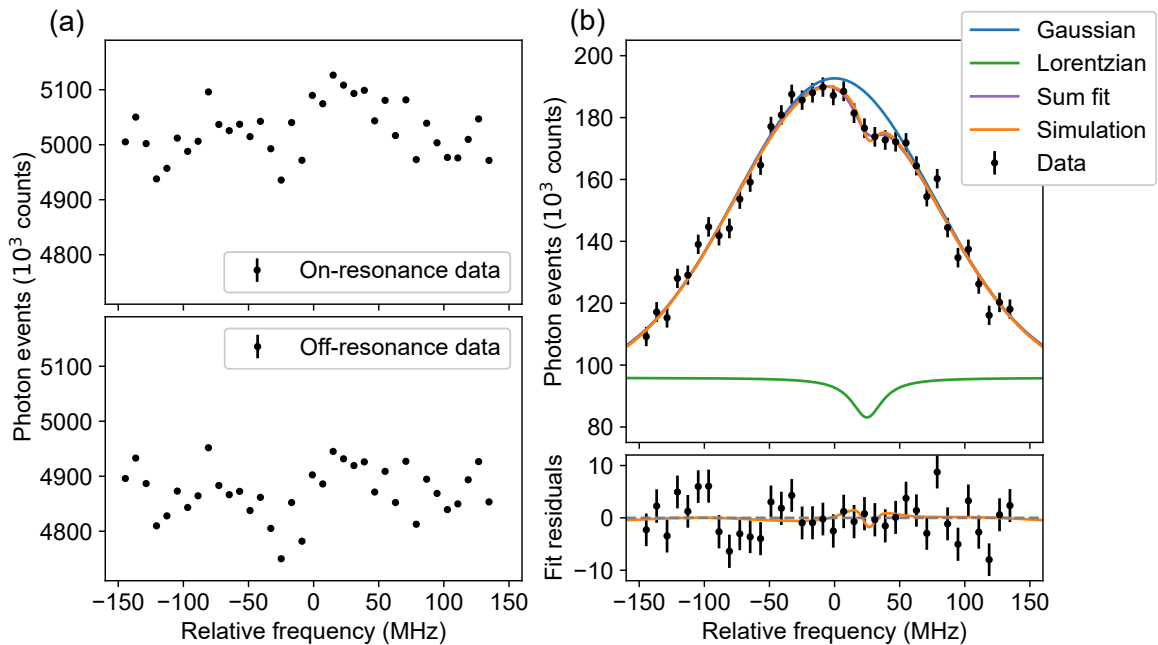


Figure 5.4: Fluorescence spectrum from saturation spectroscopy. (a) The raw on-resonance and off-resonance signals. The scattering of the data is larger than the signal height due to the long dwell time required in a direct laser-frequency scan. (b) The data resulting from subtracting the off-resonance from the on-resonance data. A pump dip appears at the velocity class saturated by the anticollinear pump laser. The difference of a Gaussian (blue) and a small Lorentzian (green) to account for the pump dip is fitted to the data to give the full shape (purple). Additionally, the solution of the rate equations for Gauss distributed velocities is fitted with free pump laser power, pump dip position, y -axis offset and signal scale (orange). The residuals show the data and the simulation fit relative to the sum fit.

To saturate the $^3S_1 \rightarrow ^3P_2$ transition in ^{12}C for a single velocity class, the anticollinear pump laser was operated at the maximal available power of 2 mW inside the beamline and stabilized to a fixed frequency. The second, collinear scan laser was used at a power of 1.1 mW to scan the fluorescence spectrum. Due to the fast decay of the population in the 3P_2 state back to the 3S_1 state, probing the saturated transition requires the simultaneous presence of the pump and scan laser. Consequently, the laser background here is much higher than in conventional fluorescence spectra. When combined with a long dwell time of 1 s, this results in significant scattering of the number of photon events from the laser background, rendering the spectrum useless if the background is not subtracted. This is demonstrated in Fig. 5.4(a). By subtracting the off-resonance recorded background as described in Sec. 5.1.2, a clear spectrum with a small pump dip emerges, see Fig. 5.4(b).

To extract the transition frequency from the spectrum, the position of the pump dip must be determined. This can be achieved by fitting a Gaussian, with a subtracted Lorentzian to describe the pump dip in the data. The laser frequency at which the collinear scan laser is in resonance with the same velocity class as the anticollinear pump laser can be extracted from the position of the Lorentzian. The spectrum presented was recorded for approximately thirty minutes. The position of the pump dip has a statistical uncertainty of 4.8 MHz, which is three times larger than the uncertainty of the position of the main peak. The fitted full width at half maximum (FWHM) of the pump dip is 29(20) MHz, which is consistent with an expected saturation-broadened natural linewidth of approximately 17 MHz and 6 times narrower than the main peak ($\sqrt{8 \ln(2)}\sigma = 179(6)$ MHz). However, the low dip intensity causes the relatively large statistical uncertainty of the dip position.

Alternatively, the rate equations can be solved with variable parameters and fitted to the data to have a better approximation of the real lineshape. The result of fitting the solution of the rate equations for Gauss distributed velocities using the pump laser power, pump dip position, y -axis offset and signal scale as free parameters is shown in Fig. 5.4(b) and was performed with the *qspec* package described in chapter 3. The solution slightly deviates from the fit of a sum of Gaussian and Lorentzian, as can be seen in the fit residuals. The pump-dip position shifts by 1.2(3) MHz while its uncertainty estimated by the fit routine remains similar. The fitted laser power of 1.54(48) mW is consistent with the measured value of 2 mW but has a large uncertainty. It should be noted that the convergence of the fit is quite unstable and depends to some degree on the start parameters of the fit. The Gauss distribution had to be fixed in order for the fit to converge properly. These issues are consequences of the weak pump dip but also of the missing baseline which was not measured to increase the number of data points in the pump dip while decreasing the measurement time. Yet, also the resolution of the pump dip still poses a problem.

Thus, the extended measurement time per spectrum, challenging laser power requirements, and resulting low pump dip statistics render the use of saturation spectroscopy in C^{4+} impractical with the given experimental setup. However, increasing the depth of the pump dip by operating the pump laser at a higher laser power may result in reduced scattering of transition frequencies caused by interactions with different velocity classes, which is presently the primary contribution to the systematic uncertainty [63, 64]. A detailed analysis of the systematic uncertainties is given in Sec. 5.2.3. In the case in which an operation of the EBIS in pulsed mode is inevitable, less stringent requirements would already lead to an improvement in precision of the extracted

transition frequency due to the up to ten times larger Doppler width of the corresponding spectra. Measurements recorded in the pulsed operation mode are presented in Sec. 5.6. Within this work, an attempt was made to utilize optical population transfer between the two hyperfine structure ground states in $^{13}\text{C}^{4+}$ as the ions pass the pumping drift tube in front of the FDR to induce a pump dip. However, the branching ratios are distributed in a way that either a large pump dip would occur in a resonance peak of a weak transition or a small pump dip would occur in a peak of a strong transition. In both cases, it is likely that the relative amount of ions with the appropriate velocity and flight path to be both pumped and probed was too small to observe a pump dip.

5.2 Determination of transition frequencies

The resonance frequencies of the $1s2s\,{}^3\text{S}_1 \rightarrow 1s2p\,{}^3\text{P}_{0,1,2}$ transitions have been determined from the recorded fluorescence spectra. Due to the hyperfine structure splitting in $^{13}\text{C}^{4+}$, there are nine distinct resonance frequencies. Each pair of collinear (c) and anticollinear (a) resonance spectra yields a single rest-frame frequency value. At least 21 measurement pairs were taken for each transition to minimize statistical fluctuations. Spectra were recorded in the order ac-ca to compensate for linear drifts in the kinetic energy of the ions. The final resonance frequencies are compiled in Tab. 5.1.

Table 5.1: Measured resonance frequencies of the ${}^3\text{S}_J \rightarrow {}^3\text{P}_{J'}$ transitions in $^{13}\text{C}^{4+}$. Results for the two segments of the FDR are given relative to the final results and only with their statistical uncertainty which is the error of the weighted mean. The final results are derived from both segments and their uncertainties including statistical and systematic contributions, see text. All values are given in MHz.

$(J, F) \rightarrow (J', F')$	$\nu_{(J,F) \rightarrow (J',F')}$		
	Segment 1	Segment 2	Final
$(1, 1/2) \rightarrow (0, 1/2)$	-0.2 (0.7)	0.1 (0.5)	1 316 147 920.6 (1.9)
$(1, 3/2) \rightarrow (0, 1/2)$	-0.1 (0.3)	0.1 (0.3)	1 316 084 566.3 (1.8)
$(1, 1/2) \rightarrow (1, 1/2)$	2.4 (1.1)	-1.0 (0.7)	1 315 749 143.7 (1.9)
$(1, 1/2) \rightarrow (1, 3/2)$	0.2 (1.0)	-0.1 (0.8)	1 315 781 189.1 (2.0)
$(1, 3/2) \rightarrow (1, 1/2)$	-0.1 (0.8)	0.1 (0.8)	1 315 685 791.2 (2.0)
$(1, 3/2) \rightarrow (1, 3/2)$	-0.4 (0.2)	0.3 (0.2)	1 315 717 838.5 (1.8)
$(1, 1/2) \rightarrow (2, 3/2)$	0.4 (0.6)	-0.1 (0.2)	1 319 813 468.4 (1.8)
$(1, 3/2) \rightarrow (2, 3/2)$	0.3 (0.8)	-0.1 (0.4)	1 319 750 116.8 (1.8)
$(1, 3/2) \rightarrow (2, 5/2)$	0.1 (0.1)	0.0 (0.1)	1 319 798 680.5 (1.8)

5.2.1 Fitting fluorescence spectra

The fluorescence spectra are fitted using the least-square optimization function `optimize.leastsq` provided by the `scipy` Python package [135]. Since the natural linewidth of the measured transition is only 9 MHz [97] while the full width at half maximum of the resonances is about 150 MHz due to residual Doppler-broadening, the Lorentzian part is neglected and either a Gaussian of the form

$$f(x, [x_0, \sigma, a, y_0]) = a \exp \left[-\frac{(x - x_0)^2}{2\sigma^2} \right] + y_0, \quad (5.1)$$

or in the case of dispersion spectra, the derivative of a Gaussian

$$g(x, [x_0, \sigma, a, y_0]) = a \frac{(x - x_0)}{\sigma} \exp \left[-\frac{(x - x_0)^2}{2\sigma^2} \right] + y_0, \quad (5.2)$$

is used to fit the data. In both cases, a y -axis offset is used to account for non-zero baselines and the parameter a is given in units of the y -axis. The uncertainties of the fit results are scaled to yield $\chi^2_{\text{red}} = 1$. In Fig. 5.3 examples of fits to the three types of recorded spectra are shown. The fits to the data were performed in the frequency space of the rest-frame of the ions. Therefore, the parameter x_0 yields the position of a resonance as a frequency value. To determine the Doppler shift, the acceleration voltage without the scan voltage is required. Since the starting potential of the ions is not known accurately, the acceleration voltage was determined in the analysis process to fulfill the conditions that it stays constant during the recording of a collinear-anticollinear pair and that the determined rest-frame resonance frequencies agree within 1 MHz. The two resonance positions are then used with Eq. (2.66) to get the electronic transition frequency. Note that this process of determining the acceleration voltage is not required to have sufficient accuracy in the determination of transition frequencies, however, it was used as a uniform criterion to determine the actual acceleration voltage.

5.2.2 Selection criteria of measurements

Not all recorded spectra were used to determine the transition frequencies due to insufficient statistics or a non-constant laser background which lead to inconclusive or wrong fits. The discarded spectra primarily come from the first segment of the FDR, which was always equipped with an elliptical mirror with significant more laser background compared to the lens system, see Fig. 4.10. Additionally, the weaker transitions and the measurements using a modulated scan voltage often yielded a very poor SNR and also had to be rejected. Hence, to filter reliable spectra, four conditions were defined which need to be fulfilled. The definitions are based on the statistics of all measurements across all transitions, as resonance peaks should only vary in height. Since a single transition frequency measurement requires one collinearly and one antecollinearly recorded spectrum, both are rejected even if only one does not fulfill the conditions. The four boundary conditions and their numerical values are depicted in the histograms shown in Fig. 5.5. It should be noted that defining useful objective criteria



Figure 5.5: Statistics of the observables used to filter reliable fluorescence spectra. Both the unfiltered (grey) and the filtered (orange) data is shown. Some of the far outliers in the unfiltered cases extend beyond the bounds of the histogram. (a) shows the full width at half maximum (FWHM) of the Gaussian fits, (b) shows the χ^2_{red} of the Gaussian fits, (c) shows the χ^2_{red} of fits of a constant to each spectrum and (d) shows the ratio of the χ^2_{red} of constant fits and Gaussian fits.

to discard samples of a statistical distribution inevitably also leads to the rejection of some useful data. However, this does not introduce any systematic shift as the desired observable to be extracted from the data, which is the x -axis position of the maximum of the Gaussian peak, is statistically independent from the chosen selection criteria. The individual transition frequencies of the nine transitions in $^{13}\text{C}^{4+}$ vary within their statistical uncertainties depending on the chosen criteria. The center-of-gravity frequency of the entire fine-structure, which is used to determine the differential mean-square nuclear charge radius, shifts by less than 0.2 MHz. The alternatives to the objective criteria would be to manually select useful spectra or to include all spectra. The former would be a subjective choice which could lead to a systematic shift. The latter would mean to include measurement that do not show a clear resonance signal. Some examples of barely rejected fluorescence spectra are shown in Fig. 5.6.

The first chosen criterion is based on the peak width. The most common full width at half maximum (FWHM) was determined by fitting a Gaussian to the histogram depicted in Fig. 5.5(a) and is about 154 MHz. To be considered valid, the measurement should be within the 3σ -range of the fitted Gaussian. The fit was chosen over statistical estimators such as the standard deviation or percentiles because it is more robust against statistical outliers and thus, describes

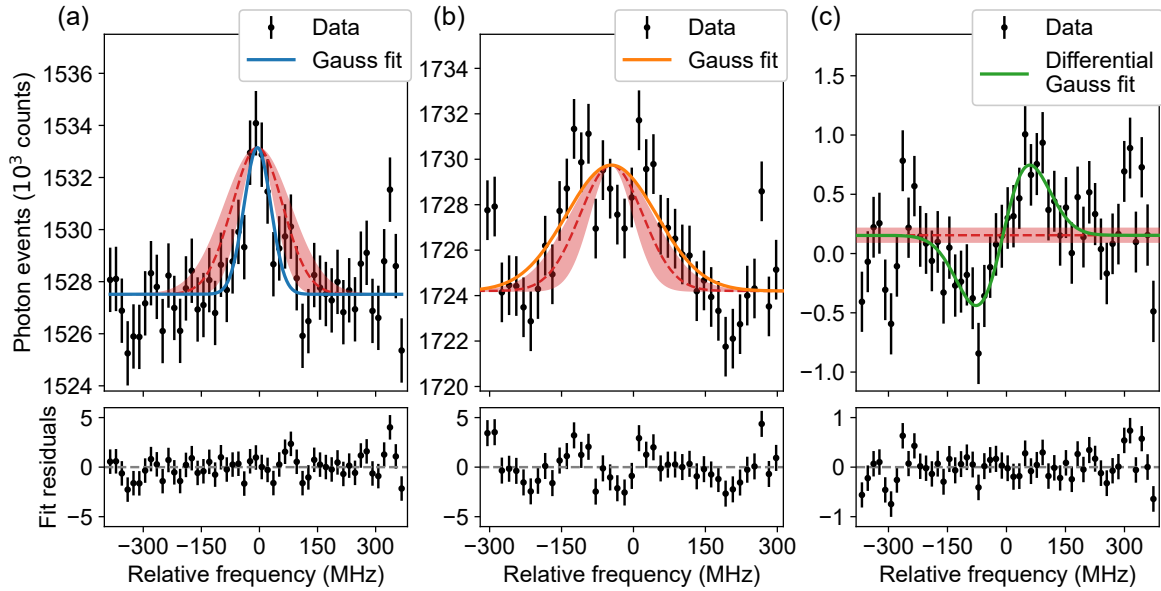


Figure 5.6: Fluorescence spectra of $^{13}\text{C}^{4+}$ that are barely rejected by different selection criteria. (a & b) With $\sigma = 34.5$ MHz and 93.9 MHz, the Gaussian fits have a smaller and a larger peak width than the minimum and maximum accepted value, respectively. The tolerated range is indicated in red. (c) The differential Gaussian fit is rejected due to a ratio $\chi^2_{\text{const}}/\chi^2_{\text{Gauss}} = 1.7 < 2$. The constant fit and its 1σ uncertainty is indicated in red.

the distribution in the proximity of the mean much better, which is more likely to contain meaningful spectra. The second criterion shown in Fig. 5.5(b), is $\chi^2_{\text{red}} \leq 3$ for the Gauss fits to the fluorescence spectra, which corresponds to the 99.73-percentile for the subset of spectra recorded with the second FDR segment. Here, the percentiles instead of a fit to the histogram were used due to the asymmetric distribution and the fact that it contains far less outliers. The latter is also the reason why the criterion was defined using only data from the second FDR segment. A constant function of the form

$$c(x, y_0) = y_0 \quad (5.3)$$

was fitted to each fluorescence spectrum to check the significance of the peak. The resulting distribution of the χ^2_{red} is depicted in Fig. 5.5(c). The minimum accepted value corresponds to the 4.5-percentile of the χ^2_{red} of the constant fits. As illustrated in Fig. 5.5(d), the final condition requires the ratio of the χ^2_{red} of constant fits and Gaussian fits to exceed two. This number was chosen arbitrarily and raises the significance of the peak in accepted measurements.

5.2.3 Systematic uncertainties

The systematic uncertainties in collinear laser spectroscopy measurements with C^{4+} have been discussed in detail in [63]. The systematic measurements that are discussed therein were not repeated within this work due to the consistent behavior of the experiment throughout the measurement campaign. In this section, the systematic contributions found in [63] are revisited and applied to the slightly altered experimental conditions underlying this work. Where useful, additional considerations about the systematic contributions are given. A summary of all considered systematic uncertainties is given in Tab. 5.2.

Table 5.2: Summary of all systematic uncertainties of the transition frequency measurements in $^{13}\text{C}^{4+}$. The total systematic uncertainty is given by the geometric sum of all individual uncertainties.

Contribution	Symbol	Uncertainty (MHz)
Spatial velocity distribution	$\Delta\nu_{\text{spatial}}$	1.72
Laser- and ion-beam alignment	$\Delta\nu_{\text{angle}}$	0.09
Photon recoils	$\Delta\nu_{\text{rec}}$	0.41
Laser polarization	$\Delta\nu_{\text{pol}}$	0.24
Absolute voltage	$\Delta\nu_U$	0.00
Amplification factor	$\Delta\nu_{\delta U}$	0.00
Total systematic uncertainty	$\Delta\nu$	1.79

Spatial velocity distribution In the previous measurements with $^{12}\text{C}^{4+}$, the dominant contribution to the systematic uncertainty was identified to originate from an inhomogeneous distribution of the ion velocities in the ion-beam cross section. This is a consequence of bending the ion beam electrostatically by 60° . In combination with a misalignment between the collinear and anticollinear laser beam, this leads to different velocities being addressed by the two lasers ($\beta_c \neq \beta_a$) and, therefore, to a systematic frequency shift as Eq. (2.66) is no longer applicable. Other potential systematic errors, mostly experimentally indistinguishable from this contribution, were estimated to be significantly smaller. A systematic shift of 8.6 MHz was measured when misaligning the two laser beams by 1 mm at the entrances to the beamline. This corresponded to an angle of 0.38 mrad and a horizontal displacement of approximately 0.55 mm between the laser beams at the position of the FDR [63]. The artificial misalignment in the systematic measurement was roughly a factor of five larger than the achieved precision in overlapping the laser beams. Thus, based on experimental conditions, the spatial systematic uncertainty was estimated to be $\Delta\nu_{\text{spatial}} = 8.6 \text{ MHz}/5 = 1.7 \text{ MHz}$, which was also confirmed by ion-optical simulations in [63]. Note that the theoretical contribution of the changed Doppler shift due to the angle between the laser beams is small compared to this experimental value as discussed in the next paragraph. Hence, the main contribution to this frequency shift can be ascribed to addressing different velocities in the ion beam with the two lasers caused

by a parallel shift of the two laser beams. Contrary to a misalignment of the angle, which always leads to a positive frequency shift in the anticollinear case, the effect of a displacement changes sign when moving from left to right. Thus, frequency shifts due to the laser beam overlap should be randomly distributed variables that are symmetrically centered around zero, corresponding to perfect alignment. Note that this still holds true if the laser beams differ in size but are symmetric in the direction in which the ion velocities change. Therefore, this systematic uncertainty should be referred to as an enhanced statistical uncertainty. As such, it should depend on the number of measurement series since the laser alignment was readjusted at the start of each series. In the following, its applicability to the measurements carried out within this work is discussed and residual systematic contributions are estimated.

Laser- and ion-beam alignment The alignment procedure of the laser beams, explained in Sec. 4.4.3, was slightly changed within this work compared to the previous measurements with $^{12}\text{C}^{4+}$ due to the new beam stabilization system. Nonetheless, the two laser beams were manually superposed across a distance of approximately 14 m. A displacement of less than 0.5 mm between the incoming and outgoing collinear and anticollinear beams was ensured, including drifts of the laser beams during a measurement series. This conservative estimation corresponds to an angle of 0.07 mrad which closely approximates the angle used to derive the systematic uncertainty for the beam overlap of 1.7 MHz. Given that the laser-beam diameters as well as the ion beam size are comparable to those of the previous experiment, this value remains a valid assumption.

To determine the error caused by angles between the ion and the laser beams in Eq. (2.66), the alignment of all three beams has to be considered. The largest potential error occurs when there is an angle between the ion beam and one of the laser beams α_{IL} and the angle between the two laser beams α_{LL} leads to an even larger tilt between the second laser and the ion beam. The deviation between the experimentally determined transition frequency and the actual resonance frequency is given by [63]

$$\Delta\nu_{\text{angle}} = \nu_0 \left| 1 - \gamma \sqrt{(1 + \beta \cos(\alpha_{IL} + \alpha_{LL}))(1 - \beta \cos(\alpha_{IL}))} \right|. \quad (5.4)$$

Before each measurement series, the ion beam was aligned with the spots of the collinear laser beam on the two available MCP detectors, which are located 2.6 m apart from each other. The average diameter of the collinear laser beam in this region of the beamline is about 0.8 mm, see Fig. 4.14, and the maximum observed drift of the ion beam on either of the two detectors during a measurement series was one laser beam diameter. Hence, $\alpha_{IL} < 0.62$ mrad, resulting in a maximum error of $\Delta\nu_{\text{angle}} = 0.09$ MHz, which is well below the estimated total uncertainty.

Photon recoils During the absorption process of a photon, its momentum $h\nu/c$ is transferred to that of the atom. Consequently, the photon energy required to excite an atomic transition is larger than the actual transition energy. This mismatch is already considered in Eq. (2.66) used to calculate rest-frame transition frequencies and does not add any systematic uncertainty. However, the momentum transfer also changes the velocity of the ion, *i.e.*, every time the atom

decays back to the ground state spontaneously, it emits a photon isotropically with respect to the laser beam axis and, hence, on average keeps the momentum of the absorbed photon. Since the photons of the collinear and anticollinear laser propagate in opposite directions, the mean atom velocities in the two cases diverge. This introduces an error in Eq. (2.66) if more than one excitation occurs. Multiple photon absorption consistently yields a higher transition frequency. In prior experiments, this systematic error was estimated using the maximum scattering rate if the laser is perfectly in resonance [63, 151]. However, this approach overestimates the uncertainty since the resonance center contributes much less to the determined transition frequency than the flanks of the peak.

For this work, the mechanical process of photon absorption was simulated with the *simulate* module of the *qspec* package. Using the Monte-Carlo solver for the master equation that was introduced in Sec. 2.4.4, the expected number of photon momentum transfers and the influence on the transition frequency for different laser intensities can be calculated. In Tab. 5.3, the results of the simulations are summarized for the highest used laser intensities and also compared to the simpler approach of estimating the mean number of photon momentum transfers via $\bar{n} = \Gamma_{sc}t$. Here Γ_{sc} is the scattering rate in resonance and $t = 0.29 \mu\text{s}$ is the interaction time, *i.e.*, the time-of-flight of the 12.5 kV beam of $^{13}\text{C}^{4+}$ ions ($E_{\text{kin}} = 50 \text{ keV}$) through the FDR [63]. In the simulations, the influence on the determined frequency can be estimated in two ways, either using the mean number of simulated photon momentum transfers via $\Delta\nu_{\text{rec}} = 2\bar{n}\delta\nu_{\text{rec}}$ or by fitting a Gaussian to the simulated fluorescence spectrum. In the first case, \bar{n} is determined on the simulated velocity distribution in longitudinal direction through $\bar{n}_{\text{sim}} = \delta v_x/v_{\text{rec}}$. Results of all three determinations are compared in Tab. 5.3.

The interpretation of the results requires some caution. The frequency shifts determined from the Gauss fits directly correspond to experimental center frequencies, hence, $\delta\nu_{\text{rec}}$ needs to be subtracted to get the actual frequency offset due to multiple photon momentum transfers.

Table 5.3: Results of the photon recoil simulations. The saturation parameters are calculated using the center intensity of a Gaussian laser beam $I = 1169 \mu\text{W/mm}^2$ given the maximum used laser power $P = 0.9 \text{ mW}$ and the laser beam diameter $w_0 = 0.7 \text{ mm}$. The simulations yield a change in velocity for every simulated atom that occupies the ^3P state. The mean velocity change δv_x is divided by $v_{\text{rec}} = 0.135 \text{ m/s}$ to obtain \bar{n}_{sim} . The frequency change caused by a single photon momentum absorption is $2\delta\nu_{\text{rec}} = 0.6 \text{ MHz}$. Uncertainties in the simulation results are approximate estimates derived from running the Monte-Carlo simulations multiple times.

Transition	Saturation	\bar{n}_{calc}	\bar{n}_{sim}	$\Delta\nu_{\text{rec}}$ (MHz)					
				I/I_0	$\Gamma_{sc}t$	$\delta v_x/v_{\text{rec}}$	$2\bar{n}_{\text{calc}}\delta\nu_{\text{rec}}$	$2\bar{n}_{\text{sim}}\delta\nu_{\text{rec}}$	Gauss fit ^a
$(J, F) \rightarrow (J', F')$									
$(1, 1/2) \rightarrow (0, 1/2)$	0.13	0.95	0.14(1)	0.56	0.08(1)	0.01(1)			
$(1, 3/2) \rightarrow (1, 3/2)$	0.39	2.30	0.65(1)	1.36	0.38(1)	0.18(1)			
$(1, 3/2) \rightarrow (2, 5/2)$	0.65	3.22	1.45(2)	1.92	0.86(2)	0.41(2)			

^a $\Delta\nu_{\text{rec}} = \nu_{\text{fit}} - \delta\nu_{\text{rec}}$, see text.

This correction is already applied for the value listed in Tab. 5.3. The other method, which was also used in [63, 151], yields frequency offsets based on mean numbers of momentum transfers. Since only atoms in the 3P states contribute to the fluorescence spectrum at a given time, only those atoms were considered. Here, the subtraction of $\delta\nu_{\text{rec}}$ is not required because the atom momenta are calculated for the time when the atoms were still in the 3S_1 state, as described in Fig. 2.3. The results show that the error introduced by fitting a Gaussian to a Doppler-broadened spectrum is much smaller than the estimated error when using the scattering rate in resonance. The upper limit of the frequency shift $\Delta\nu_{\text{rec}} = 0.41$ MHz due to the finite photon momentum determined with the fit method is still well below the total systematic uncertainty of 1.8 MHz. Additionally, it is worth noting that the frequency shift is particularly large in the closed ${}^3S_1, F = 3/2 \rightarrow {}^3P_2, F' = 5/2$ transition while in all other transitions, multiple photon momentum transfers are suppressed due to the optical population transfer.

Laser polarization A non-linear laser polarization induces a shift in the determined transition frequencies depending on the magnetic field vector inside the FDR. The upper limit of this effect is given by a magnetic field vector aligned with the beam axis and completely circularly polarized light. The only considerable magnetic field present in the FDR is that of the earth with a magnetic flux density of approximately 50 μT . In ${}^{13}\text{C}^{4+}$, the ${}^3S_1, F = 1/2 \rightarrow {}^3P_1, F' = 1/2$ transition undergoes the largest shift between ± 1.6 MHz, depending on the handedness of the circularly polarized light. However, the magnetic field is not parallel to the beam axis. According to the International Geomagnetic Reference Field (IGRF) model, the B -field in Darmstadt is given by [162]

$$\mathbf{B}_{\text{IGRF}} = 16.915\mathbf{e}_x - 11.054\mathbf{e}_y + 44.545\mathbf{e}_z, \quad (5.5)$$

where \mathbf{e}_x is the unit vector of the beam axis in collinear direction, \mathbf{e}_z faces upwards, orthogonal to the floor and \mathbf{e}_y completes the orthonormal basis, see also the coordinate system in Fig. 3.4. In 2018, the magnetic field at the beamline has also been measured using a Hall probe. The resulting B -field vector is

$$\mathbf{B}_{\text{exp}} = 14.6(2.1)\mathbf{e}_x - 3.9(3.3)\mathbf{e}_y + 33.8(2.1)\mathbf{e}_z. \quad (5.6)$$

The orientation of the vector agrees well with that of the theoretical vector, being tilted by only $7.5(4.9)^\circ$. However, the absolute value of the magnetic flux density, with $37.0(2.1)$ μT , is only about 75 % of the theoretical value, which might be due to shielding material in the building structure. In the following, the larger theoretical field vector is used for the worst-case estimation of potential systematic errors.

In either case, the maximum shift no longer appears with circularly polarized light but with a mixture of linearly and circularly polarized light. This increases the demand on the linearity of the polarization. No polarizing beam splitter or linear polarizer was used in front of the beamline due to the limited available laser power and because the laser light coming from

the second frequency-doubling stage is inherently linearly polarized in the z -direction. Hence, if the laser beam only is reflected in the xy -plane or into the z -axis, the linear polarization will be preserved. The ratio of linearly to circularly polarized light was tested using a linear polarizer. A maximum value of 6.5 % of circularly polarized light was found in front of the beamline, including both the collinear and anticollinear site. This corresponds to a maximum shift in the above mentioned transition of $\Delta\nu_{\text{pol}} = 0.24$ MHz which is negligible compared to the total systematic uncertainty of 1.8 MHz. Additionally, systematic transition frequency measurements with different polarizations have been performed within [63]. There, no polarization-dependent frequency shift was detected exceeding the scattering of the data.

5.2.4 Derivation of the final transition frequencies

The final frequency values ν_0 of the $1s2s\ ^3S_1 \rightarrow 1s2p\ ^3P_{0,1,2}$ transitions are given by the mean of all filtered measurements \mathcal{M} including both segments of the FDR \mathcal{F} weighted by their fit

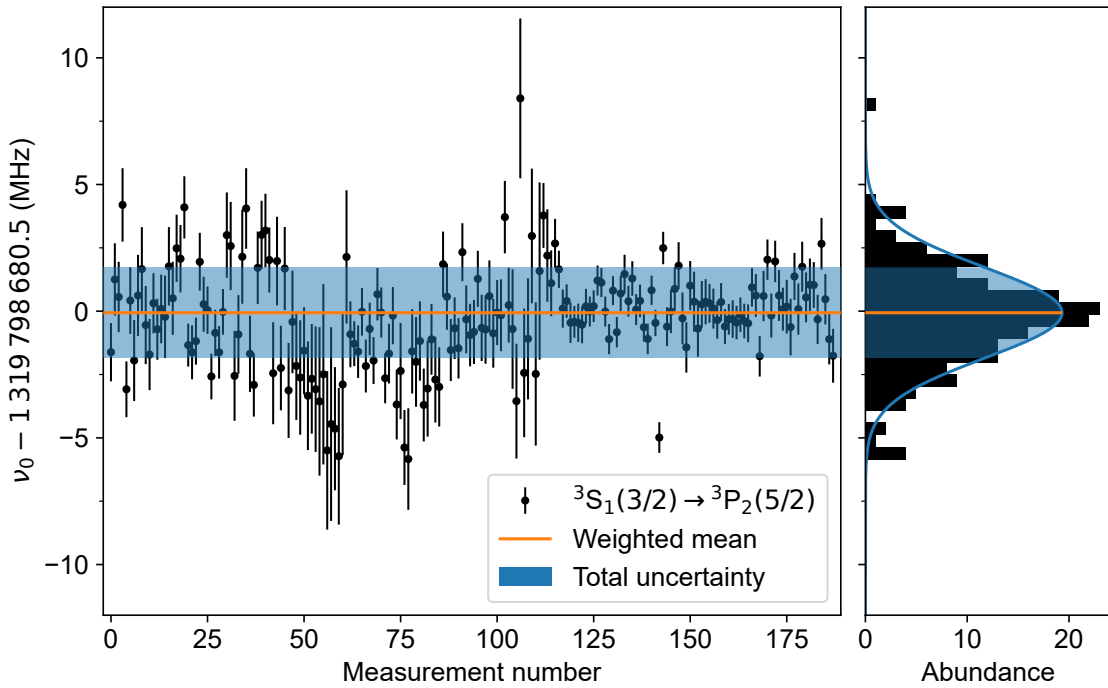


Figure 5.7: Statistics of the $1s2s\ ^3S_1, F = 3/2 \rightarrow 1s2p\ ^3P_2, F' = 5/2$ transition frequencies measured with the lens segment of the FDR. The total 1σ uncertainty range is shown in blue. The Gaussian plotted on the right is fitted to the histogram by only varying its amplitude. The measurements are well within the total 1σ uncertainty range. Single measurements systematically deviate from the mean value which can be explained either by a drifting ion energy as in measurement 142 or by misaligned laser beams.

uncertainties σ_{ij} such that

$$\nu_0 = \sum_{i \in \mathcal{F}} \sum_{j \in \mathcal{M}} \frac{\nu_{ij}}{\sigma_{ij}^2} / \sum_{i \in \mathcal{F}} \sum_{j \in \mathcal{M}} \frac{1}{\sigma_{ij}^2}. \quad (5.7)$$

The results from both FDR segments are correlated to some extend as the same experimental conditions apply with only minor differences in laser and ion beam size. Consequently, the additional results from the second segment cannot be used to decrease the uncertainty of the combined results. Instead, the final statistical uncertainty of a transition is determined by taking the minimum of the standard errors of their weighted means

$$\sigma_{\text{stat}} = \min_{i \in \mathcal{F}} \sqrt{\frac{1}{\sum_{j \in \mathcal{M}} \sigma_{ij}^{-2}}}. \quad (5.8)$$

This only covers statistical uncertainties given by the fit but does not account for scattering of the transition frequencies due to changing experimental conditions. As discussed in Sec. 5.2.3, the systematic uncertainty mainly consists of statistical fluctuations observed in the resonance positions which the fit does not account for. Hence, the statistical and systematic uncertainties can be combined into a single total uncertainty by using the geometric sum

$$\sigma_0 = \sqrt{\sigma_{\text{stat}}^2 + \sigma_{\text{sys}}^2}. \quad (5.9)$$

The resulting final transition frequencies and their uncertainties are summarized in Tab. 5.1. As an illustration, Fig. 5.7 displays the individual frequencies of the $1s2s\ ^3S_1, F = 3/2 \rightarrow 1s2p\ ^3P_2, F' = 5/2$ transition as determined from the fits. The observed scattering of the data for this transition, whose statistical uncertainty is negligible, demonstrates good agreement with the total uncertainty.

5.3 Hyperfine structure of $^{13}\text{C}^{4+}$

The precisely determined absolute transition frequencies listed in Tab. 5.1 enable an investigation of the hyperfine structure, *i.e.*, the hyperfine A parameter and the center-of-gravity frequency. The latter can then be used to determine isotope shifts of the $^3S_1 \rightarrow ^3P_{0,1,2}$ transitions between $^{12,13}\text{C}^{4+}$. These parameters can be determined by fitting the standard HFS formula (Eq. (2.16)) to the nine resonance frequencies. Alternatively, the center of gravity can be deduced by calculating the mean of the individual transitions weighted by the Racah intensities as defined in Eq. (2.48). The results are compiled in Tab. 5.4 and both approaches are in good agreement.

Due to hyperfine-induced mixing of the $^3P_{0,1,2}$ and the 1P_1 states, the determined center-of-gravity frequencies deviate from a hypothetical transition frequency of $^{13}\text{C}^{4+}$ with a vanishing

Table 5.4: Center-of-gravity frequencies determined with different methods. The mean of all ${}^3S_1 \rightarrow {}^3P$ transitions weighted by the Racah intensities (last row, first numeric column) is used in the further analysis to determine the nuclear charge radius. In case of the fit methods, only the hyperfine structure was fitted. The center-of-gravity frequency of all transitions was determined by using the fine-structure weights as in the weighted mean column.

Transition	weighted mean	standard fit	hyperfine-induced fit	
${}^3S_1 \rightarrow {}^3P_0$	1 316 105 684.4 (1.4)	1 316 105 684.7 (1.3)	0.3	1 316 103 946.9 (1.3) -1737.5
${}^3S_1 \rightarrow {}^3P_1$	1 315 728 273.3 (1.1)	1 315 728 273.0 (1.0)	-0.3	1 315 728 925.4 (1.0) 652.1
${}^3S_1 \rightarrow {}^3P_2$	1 319 800 372.2 (1.2)	1 319 800 372.3 (1.2)	0.1	1 319 800 329.2 (1.2) -43.0
${}^3S \rightarrow {}^3P$	1 318 032 485.0 (0.8)	1 318 032 485.0 (0.8)	0.0	1 318 032 485.5 (0.8) 0.5

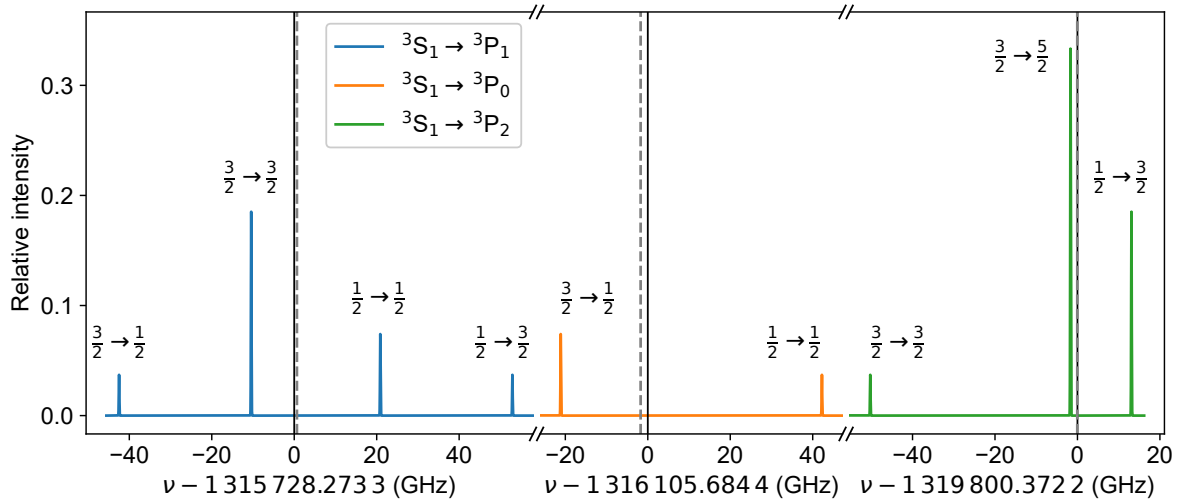


Figure 5.8: Hyperfine structure (HFS) spectrum of the $1s2s {}^3S_1 \rightarrow 1s2p {}^3P_{0,1,2}$ transitions in ${}^{13}\text{C}^{4+}$ based on the experimentally determined frequencies listed in Tab. 5.1. The shown peak heights correspond to the theoretical transition strengths used in Eq. (2.48) to determine the center of gravity of the HFS spectrum. The grey dashed lines mark the theoretical fine-structure transition frequencies if hyperfine-induced mixing is considered and are shifted by up to 1.7 GHz from the center-of-gravity frequencies.

magnetic moment. By fitting Eq. (2.18) with off-diagonal elements that consider hyperfine-induced mixing to the nine resonance frequencies, corrected values of the three center-of-gravity frequencies were determined. For the fit, the off-diagonal elements as well as $\langle 11 || \mathbf{T}^{(1)} || 11 \rangle$ of the $\mathbf{T}^{(1)}$ matrix were fixed to the theoretically determined values compiled in Tab. 2.3 so that only the two diagonal elements $\langle 31 || \mathbf{T}^{(1)} || 31 \rangle$ and $\langle 32 || \mathbf{T}^{(1)} || 32 \rangle$ were kept as free fit parameters. The resulting frequencies are depicted as grey lines in Fig. 5.8. By computing the weighted

Table 5.5: Hyperfine structure parameters determined from fits of Eq. (2.16) and Eq. (2.18) to the transition frequencies listed in Tab. 5.1. All values are given in MHz.

HFS-parameter	standard fit	hyperfine-induced fit
$A(^3S_1)$	42 234.8 (0.9)	42 234.8 (0.9)
$A(^3P_1)$	21 364.3 (1.3)	–
$A(^3P_2)$	19 425.6 (0.9)	–

mean of these hyperfine center frequencies based on Eq. (2.48), the center of gravity of the entire fine structure was obtained. This value deviates by only 0.5 MHz from the value obtained by taking the weighted mean of all nine transitions. This deviation is consistent with the combined 1σ uncertainty of 1.1 MHz of both analysis methods. No deviation is found when not considering mixing with the 1P_1 state. However, the center-of-gravity frequencies of the individual fine-structure transitions deviate -1.74 GHz in case of the 3P_0 state, 0.65 GHz in the 3P_1 state and only -43 MHz in the 3P_2 state since it is separated by 4.1 THz from the 3P_1 state while the $^3P_{0,1}$ states lie within 0.4 THz. The signs and the ratio of the shifts of the $^3P_{0,1}$ states can be explained with their energetic order and by counting the contributing F' quantum numbers: Neglecting the mixing with the 3P_2 state, only one of the two 3P_1 states, *i.e.* $F' = 1/2$, mixes with the single 3P_0 , $F' = 1/2$ state. Hence, the average transition to the 3P_1 and the 3P_0 states shifts approximately with the ratio 1 : -2 . Deviations thereof are due to the mixing of the 3P_1 with the 3P_2 state as well as the HFS splitting which changes the distance between the transitions and thus the mixing contributions of the individual states. For $F' = 1/2$, an admixture of 0.4359 % of the 3P_1 in the 3P_0 state and vice versa was found. For $F' = 3/2$ and the $^3P_{1,2}$ states, the admixture is only 0.0027 %. The shifts caused by hyperfine-induced mixing can serve as interesting benchmark values for theory, similar to the fine-structure splitting in $^{12}\text{C}^{4+}$ [64] or the splitting of the 3S_1 state in ^3He [163].

HFS parameters were determined from the fits of the HFS formulas to the transition frequencies. In case of the hyperfine-induced-mixing model, only the ground state A -parameter can be extracted directly since the A -parameters of the 3P states are not well-defined anymore. However, the fitted diagonal elements of the $\mathbf{T}^{(1)}$ matrix can be compared to the theoretical values. The final HFS parameters are listed in Tab. 5.5. Both HFS models excellently agree in the extracted splitting of the 3S_1 ground state. Combined with existing experimental results in ^3He [164], $^{6,7}\text{Li}^+$ [165] and $^{11}\text{B}^{3+}$ [147, 166], all splittings are consistent with an empirical scaling law of $\Delta E_{\text{HFS}} \propto Z^{3.04}$ within 10 MHz. The $\mathbf{T}^{(1)}$ matrix elements determined from the fit of the hyperfine-induced mixing model in units of $\frac{e^2}{4\pi\varepsilon_0} \frac{1}{4\pi a_0^2} \frac{1}{m_{\text{pc}}} = 13\,074.70$ MHz are

$$\langle 31 || \mathbf{T}^{(1)} || 31 \rangle = 2.704\,36 (17), \quad \langle 32 || \mathbf{T}^{(1)} || 32 \rangle = 5.805\,91 (28).$$

These agree within 1σ and 2σ , respectively, with the theoretical predictions from [99] listed in Tab. 2.3, which suggests that also the fixed off-diagonal elements are reasonable predictions that

can be used to derive the fine-structure transition frequencies. Note that fitting to the resonance frequencies in all cases yields a χ^2_{red} of only 0.36 which means that the systematic uncertainties of the resonance frequencies are larger than the actual recorded statistical scattering, hinting at a conservative uncertainty estimation.

5.4 Nuclear charge radius of ^{13}C

The rms nuclear charge radius $R_{\text{C}}^{13} = \sqrt{\langle r^2 \rangle^{13}}$ of ^{13}C has been determined relative to the well-known nuclear charge radius R_{C}^{12} of ^{12}C [34–37, 39, 64]. For this, the isotope shifts $\delta\nu^{12,13} := \nu^{13} - \nu^{12}$ were obtained from the center-of-gravity frequencies of the $1s2s\,{}^3\text{S}_1 \rightarrow 1s2p\,{}^3\text{P}_{0,1,2}$ transitions. Table 5.6 lists the isotope shifts derived from the weighted mean approach described in Sec. 5.3 and experimentally determined literature values from S. Ozawa *et al.* [167]. These values are systematically lower than the values determined within this work but also have more than three orders of magnitude larger uncertainties of a few GHz. Furthermore, Tab. II and Fig. 3 of [167], which include the isotope shift values and the resonance signals, respectively, suggest a negative isotope shift if assuming the definition used in this work. However, Tab. II and Fig. 3 are inconsistent with more precise transition frequencies of $^{12}\text{C}^{4+}$ given in Tab. I of [167] that agree well with the new precise results from [63, 64]. Since no explicit definition of the isotope shift is given in [167] and theoretically, the dominating positive mass shift implies a positive isotope shift, the therein listed values are assumed to be taken with inverted signs. Table 5.6 also includes the field shift constant F and the mass shift $\delta\nu_{\text{M}}$ required to calculate the differential mean-square nuclear charge radius $\delta\langle r^2 \rangle^{12,13}$ using Eq. (2.47). These were determined through nonrelativistic QED atomic structure calculations, with terms up

Table 5.6: Isotope shifts $\delta\nu^{12,13} := \nu^{13} - \nu^{12}$ of the $1s2s\,{}^3\text{S}_1 \rightarrow 1s2p\,{}^3\text{P}_{0,1,2}$ transitions between $^{12}\text{C}^{4+}$ and $^{13}\text{C}^{4+}$. The transition frequencies of $^{12}\text{C}^{4+}$ to calculate the isotope shifts are taken from [63, 64]. The literature values are taken from S. Ozawa *et al.* [167] assuming an isotope shift definition with inverted sign in this reference, see text. The field-shift constant F and mass shift are theoretical values calculated by V. A. Yerokhin and K. Pachucki [168] and used together with the isotope shifts to calculate the field shift contribution.

Transition	This work	S. Ozawa <i>et al.</i>
${}^3\text{S}_1 \rightarrow {}^3\text{P}_0$	53 465.1 (2.3) MHz	45.6 (6.6) GHz
${}^3\text{S}_1 \rightarrow {}^3\text{P}_1$	51 080.5 (2.0) MHz	48.0 (6.0) GHz
${}^3\text{S}_1 \rightarrow {}^3\text{P}_2$	51 800.8 (2.1) MHz	40.5 (4.8) GHz
${}^3\text{S} \rightarrow {}^3\text{P}$	51 745.6 (1.4) MHz	
mass shift	51 719.29 (25) MHz	
field shift	26.3 (1.4) MHz	
F	-211.5 MHz/fm ²	

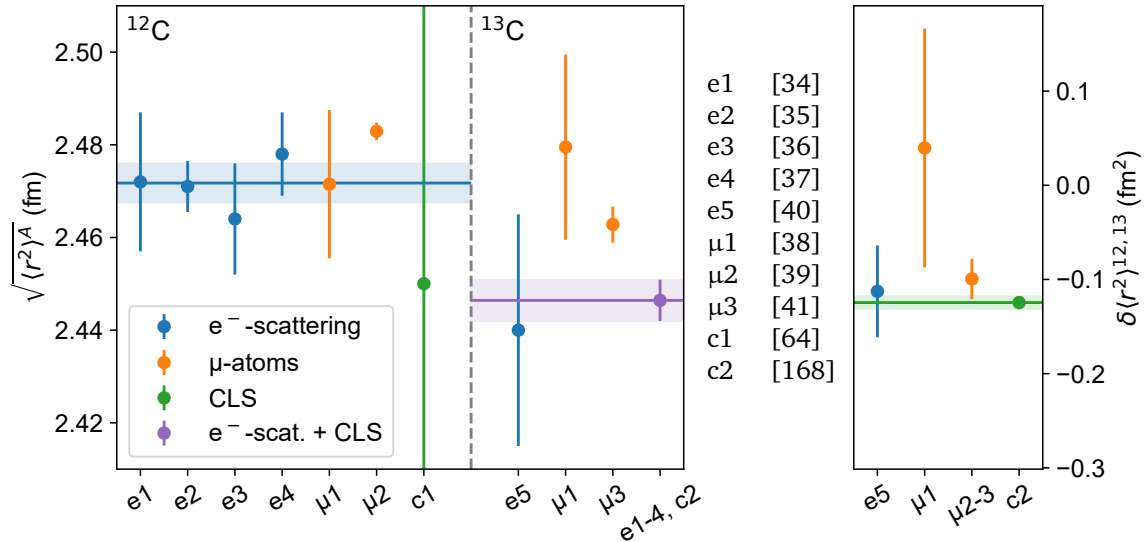


Figure 5.9: Comparison of experimentally determined absolute and relative nuclear charge radii of $^{12,13}\text{C}$ determined with elastic electron scattering (e^- -scattering, blue), muonic atom spectroscopy (μ -atoms, orange) and CLS (green). Results from CLS and e^- -scattering were combined to get an improved R_{C}^{13} (purple). The differential mean-square nuclear charge radii from e^- -scattering and μ -atoms are differences of absolute radii while the CLS result is determined directly from the isotope shift and *ab initio* atomic structure calculations using Eq. (2.47). The *x*-axis labels refer to the references contributing to the data. The label c2 refers to the result from this work [168].

to the order of ma^6 , by V. A. Yerokhin and K. Pachucki and will be published in [168]. The isotope shift parameters are specifically calculated for the difference in the center-of-gravity frequencies of the entire fine structure. R_{C}^{13} serves as an additional benchmark value for nuclear structure calculations as well as experimental results from muonic atom spectroscopy (μ -atoms). Experimentally determined absolute and differential mean-square nuclear charge radii of $^{12,13}\text{C}$ from literature and this work are plotted in Fig. 5.9 and listed in Tab. 5.7. Results from nuclear structure calculations are discussed in Sec. 5.5.

For R_{C}^{12} , several consistent results from elastic electron-scattering (e^- -scattering) measurements by different groups exist [34–37]. In the analyses of the latest two measurements, dispersion corrections are considered [35, 37]. Note that the authors of [37] recognize a difference in the applied corrections that could not be traced back due to a lag of information about the analysis in [35]. However, the results agree within 0.7σ . Results from μ -atoms can be found in [38, 39]. While the result from [38] agrees with all other charge radii for ^{12}C , the precise result from [39] predicts a nuclear charge radius that is 2.4σ larger than the weighted mean of the e^- -scattering results. R_{C}^{12} was also determined all-optically by combining CLS measurements [63, 64] and *ab initio* atomic structure calculations [65]. The result agrees well with those from the other approaches, however, currently has a two orders of magnitude larger uncertainty

Table 5.7: Absolute and relative nuclear charge radii of $^{12,13}\text{C}$ determined with elastic electron scattering (e^- -scattering), muonic atom spectroscopy (μ -atoms) and CLS. The last e^- -scattering value is the weighted mean and its standard error of all e^- -scattering results. Combined results are given relative to the weighted mean of the e^- -scattering results.

Method	R_{C}^{12} (fm)	Ref.	R_{C}^{13} (fm)	Ref.	$\delta\langle r^2 \rangle^{12,13}$ (fm 2)	Ref.
e^- -scattering	2.472 (15)	[34]				
	2.471 0 (55)	[35]				
	2.464 (12)	[36]				
	2.478 (9)	[37]				
	2.471 7 (42)	[34–37]	2.440 (25)	[40]	–0.113 (49)	[40]
μ -atoms	2.472 (16)	[38]	2.480 (20)	[38]	0.04 (13)	[38]
	2.482 9 (19)	[39]	2.462 8 (39)	[41]	–0.099 (21)	[39, 41]
CLS + e^- -scattering	2.45 (12)	[64]	2.42 (12)	[64, 168]	–0.124 5 (66)	[168]
			2.446 4 (45)	[34–37, 168]		

due to the limiting precision of the calculations.

R_{C}^{13} is far less precisely known and from e^- -scattering only a single value with comparable precision exists [40]. Results from independent measurements described in [169] with $R_{\text{C}}^{12} = 2.395(28)$ fm and $R_{\text{C}}^{13} = 2.384(47)$ fm significantly deviate from the other e^- -scattering results that came later. Hence, they are not considered in the further discussion. The nuclear charge radii determined with μ -atoms can be found in [38, 41] and are again larger than the e^- -scattering results. However, they still agree with the given uncertainty. Using the experimentally determined isotope shift and the atomic factors listed in Tab. 5.6, the differential mean-square nuclear charge radius $\delta\langle r^2 \rangle^{12,13}$ was determined. The value agrees well with the combined results from e^- -scattering that, however, have much larger uncertainties than the present result. Both $\delta\langle r^2 \rangle^{12,13}$ derived from μ -atoms deviate by 1σ from the CLS result. An improved value for the absolute nuclear charge radius R_{C}^{13} was determined by combining the weighted mean of R_{C}^{12} from e^- -scattering with the CLS results for $\delta\langle r^2 \rangle^{12,13}$ from this work using

$$R_{\text{C}}^{13} = \sqrt{\langle r^2 \rangle^{12} + \delta\langle r^2 \rangle^{12,13}}. \quad (5.10)$$

The e^- -scattering results were chosen as the reference for R_{C}^{13} to be as model-independent as possible. A small model-dependence in the e^- -scattering results cannot be ruled out completely but is expected to be smaller than that in μ -atoms. The contributing $\delta\langle r^2 \rangle^{12,13}$ from CLS is completely model-independent since it only depends on direct transition frequency measurements and well tested *ab initio* atomic structure calculations. The uncertainty is on par with the more precise result from μ -atoms and mainly limited by the uncertainty ΔR_{C}^{12} from e^- -scattering. The R_{C}^{13} determined within this work significantly deviates by -2.8σ from the precise μ -atoms result. This is a strong indication that the model-independence claimed in [41] is not sufficiently fulfilled. Although much better agreement is achieved if only the

latest results from e^- -scattering [37] are used, the radii determined with μ -atoms remain to be too large. In the near future, new x-ray spectroscopy measurements with light μ -atoms are planned which are promising to elucidate the discrepancies between the different experimental methods [170].

5.5 Nuclear structure calculations

In-medium similarity renormalization group (IMSRG) *ab initio* nuclear structure calculations were performed by M. Heinz *et. al.* to test their applicability in light nuclei [168]. Table 5.8 lists the results determined with the NN+3N interactions 1.8/2.0_{EM} [171] and $\Delta N^2 LO_{GO}$ [172, 173].¹ 1.8/2.0_{EM} includes free-space NN interactions up to N³LO and 3N interactions at N²LO, compare the Feynman diagrams in Tab. 2.2. The free parameters were fitted to NN scattering data as well as properties of ^{2,3}H and ⁴He. The interaction is regularized and renormalized in the NN interactions with a soft resolution scale of $\lambda_{NN} = 1.8 \text{ fm}^{-1}$ (355 MeV) and in the 3N interactions using a regulator function with cutoff momentum $\Lambda_{3N} = 2.0 \text{ fm}^{-1}$ (394 MeV). $\Delta N^2 LO_{GO}$ includes both free-space NN and 3N interactions up to N²LO with cutoff momenta $\lambda_{NN} = \Lambda_{3N} = 2.0 \text{ fm}^{-1}$ (394 MeV). In the construction of the chiral effective field theory, Δ resonances are considered explicitly. This introduces additional diagrams to the power counting expansion as the nucleons can be in an excited state after a pion-exchange. The free parameters are fitted to NN scattering data, properties of nuclei with $A \leq 4$ and nuclear matter properties, compare also [173].

The nuclear structure of ^{12,13}C was computed using the IMSRG with the 1.8/2.0_{EM} and $\Delta N^2 LO_{GO}$ interactions as inputs to determine their mean-square nuclear charge radii. Calculations at the effective two-body level (IMSRG(2)), where the last term $W(s)$ in the expansion defined by Eq. (2.6) is omitted, are performed routinely and are possible up to the nuclei ¹³²Sn or ²⁰⁸Pb at relatively low computational cost. The IMSRG(3), performed at the effective three-body level, is significantly more expensive and the nuclei of ¹²C and ¹⁶O are on the verge of what is currently possible. For this work, IMSRG(3) was only used with the 1.8/2.0_{EM} interaction. Uncertainties are given only for directly determined differential radii and in all cases include general model space and solver uncertainties of 0.005 fm and an additional 10 % uncertainty for the Hamiltonian. An additional uncertainty of 0.005 fm is ascribed to the extended model space in the effective three-body calculations. The uncertainties are only estimations of the precision within the given IMSRG approximation but do not cover the uncertainty introduced by approximating in the first place. More details about the interactions and many-body calculations can be found in the respective references [171–173] and in the review article [91].

The IMSRG results mostly underestimate the absolute nuclear charge radii and give too large differences between ^{12,13}C. A similar behavior for the absolute radii is found for (valence-space) IMSRG calculations across the nuclear chart [174] and ascribed to overly attractive soft NN-potentials at low resolution scales (cutoff momenta) λ_{NN} when many-body contributions are omitted [6, 175]. In other words, the nuclear saturation density is overestimated as nuclei exhibit smaller radii. Accordingly, when effective three-body interactions are included,

¹EM: D. R. Entem & R. Machleidt, GO: Gothenburg–Oak Ridge.

Table 5.8: Absolute and relative nuclear charge radii of $^{12,13}\text{C}$ determined using Eq. (2.8) with different in-medium similarity renormalization group (IMSRG) calculations at the effective two- and three-body level for the $1.8/2.0_{\text{EM}}$ and the $\Delta\text{N}^2\text{LO}_{\text{GO}}$ interaction, see text. The listed experimental values are derived from the combined elastic electron scattering results for ^{12}C and the differential radius determined within this work [168]. All values are given in fm.

Interaction	IMSRG approx.	R_{C}^{12}	R_{C}^{13}	$R_{\text{C}}^{13} - R_{\text{C}}^{12}$
$1.8/2.0_{\text{EM}}$	IMSRG(2)	2.428	2.373	-0.055(11)
$\Delta\text{N}^2\text{LO}_{\text{GO}}$	IMSRG(2)	2.418	2.372	-0.046(9)
$1.8/2.0_{\text{EM}}$	IMSRG(3)	2.530	2.419	-0.111(21)
Experiment	—	2.4717(42)	2.4464(45)	-0.0253(14)

$1.8/2.0_{\text{EM}}$ yields larger values for the radii of $^{12,13}\text{C}$ such that the radius of ^{12}C gets overestimated and for ^{13}C , the experimental result is almost reached. The larger increase of the radius of ^{12}C by 0.1 fm compared with 0.05 fm for ^{13}C is most likely a consequence of the more challenging structure of ^{12}C and the need for higher-order many-body contributions in ^{12}C . However, also odd-even staggering may play an important role here. See, for example, [123] for a comparison of odd-even staggering in Cu isotopes determined from collinear resonance ionization spectroscopy and valence-space IMSRG calculations using the $1.8/2.0_{\text{EM}}$ interaction. The $\Delta\text{N}^2\text{LO}_{\text{GO}}$ interaction yields similar absolute radii as the two-body $1.8/2.0_{\text{EM}}$, however, predicts the differential radius closest to the experimental result, agreeing within two theoretical uncertainty ranges. This suggests that the finite size of a nucleon, which changes upon the excitation of a Δ resonance, is important to describe the emergence of the nuclear size of the C isotopes. However, a clear statement is not possible at the current level of accuracy and given the challenging structure of $^{12,13}\text{C}$.

In conclusion, the remaining discrepancies between theory and the experiment can be ascribed to the complex structures of the $^{12,13}\text{C}$ nuclei. As in other light nuclei, α -clustering of nucleons increases the difficulty for the theoretical description as these deviate significantly from a shell-model viewpoint. Hence, better agreement with experiment is achieved in heavier nuclei using valence-space IMSRG. The change of the absolute nuclear charge radius with the inclusion of effective three-body operators shows that the light nuclei require higher order many-body contributions to be accurately described. However, with 12 and 13 nucleons, the two stable C isotopes are challenging for IMSRG(3) calculations and close to the current computational limits. Reducing the computational cost of IMSRG(3) calculations is a main research effort and progress is expected in the near future. Also the development of new interactions are promising ventures. For example, the $\Delta\text{N}^2\text{LO}_{\text{GO}}$ interaction is just getting established as a standard and will be improved further.

5.6 Transition frequencies from pulsed operation

Another interesting application of the EBIS that was skipped in the above discussion, is to charge breed radioactive isotopes produced at accelerator facilities. However, these cannot be fed into the EBIS as a gas but have to be injected into the trap as a pulsed beam. This inevitably requires the EBIS to be operated in pulsed mode. Therefore, it is important to test the feasibility of the determination of transition frequencies in pulsed operation and compare the results with those from continuous operation. Frequency measurements of the $1s2s\ ^3S_1, F = 3/2 \rightarrow 1s2p\ ^3P_2, F' = 5/2$ transition in pulsed mode have been conducted within this work. To produce a pulsed beam, the EBIS trap potential was set to a high voltage of $U_A = 12.5$ kV and the wall potential U_B in beamline direction was switched between U_A (open) and $U_A + 90$ V (closed) for 1 ms and 15 ms intervals, respectively. An electron current of 84 mA and a gas pressure of $6 \cdot 10^{-8}$ mbar was chosen similar to the measurements in continuous operation. The emittance of the ions in the pulsed mode is much larger than in the continuous mode due to the higher temperature and space charge effects in the propagating ion pulse. This leads to a large divergence of the pulse at the position of the FDR. Therefore, the ion pulse was refocused into the FDR to increase the laser-ion beam overlap using an einzellens located directly in front of the FDR, see Fig. 4.4. A typical spectrum in pulsed mode recorded with the

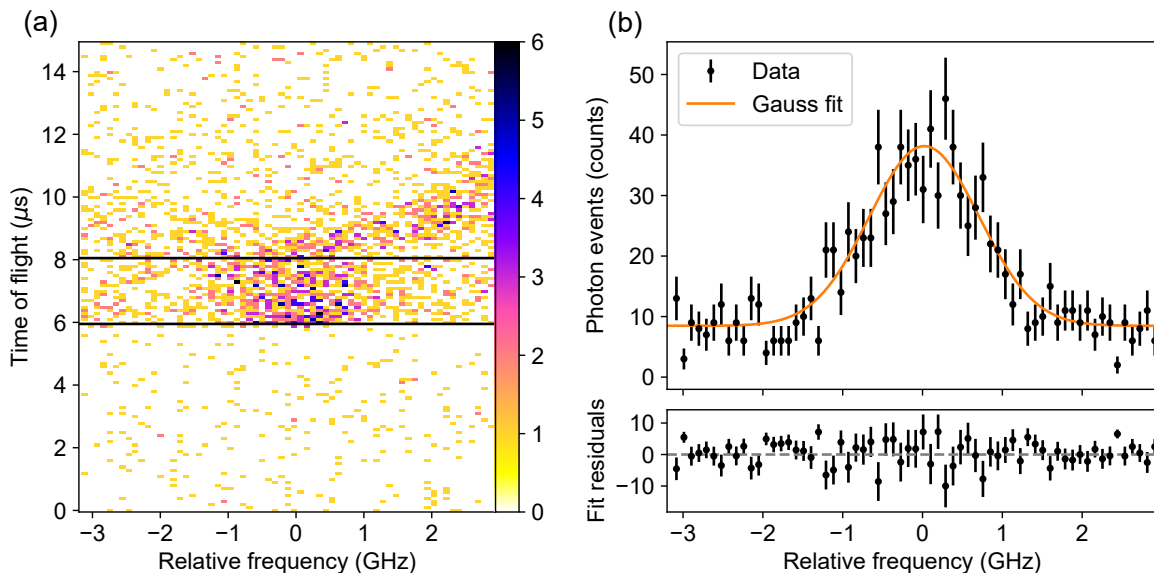


Figure 5.10: Resonance signal of the $1s2s\ ^3S_1, F = 3/2 \rightarrow 1s2p\ ^3P_2, F' = 5/2$ transition in pulsed operation recorded with the lens-based FDR. (a) The time-resolved fluorescence spectrum. The ion pulse reaches the FDR where it is excited by the anticollinear laser beam at a flight time of 6 μ s after the wall potential of the EBIS was opened. A time window of 2 μ s is used to select the ions which contribute to the projected fluorescence spectrum. (b) The projected fluorescence spectrum summed over all selected flight times. A Gaussian is fitted to the data.

new lens-based FDR is shown in Fig. 5.10.

The ion pulse released from the EBIS has a time width of $2 \mu\text{s}$ plus a slower tail of ions which are decelerated by propagating through the falling wall potential. This slow tail is cut off

Table 5.9: Transition frequencies and their statistical uncertainties of the $1s2s\ 3S_1, F = 3/2 \rightarrow 1s2p\ 3P_2, F' = 5/2$ transition determined from the pulsed and continuous spectra. The systematic uncertainty σ_{sys} of 1.8 MHz in continuous mode derived from the theoretical considerations described in Sec. 5.2.3 should be added to the statistical uncertainties according to Eq. (5.9). All values are given in MHz.

EBIS mode	FDR segment	mean	weighted mean	# data
continuous	1	mirror	1 319 798 680.69 (43)	1 319 798 680.51 (15)
continuous	2	lens / mirror	1 319 798 680.23 (15)	1 319 798 680.44 (7)
pulsed	1	mirror	1 319 798 676.5 (4.7)	1 319 798 676.7 (3.4)
pulsed	2	lens	1 319 798 682.8 (6.3)	1 319 798 681.6 (6.1)

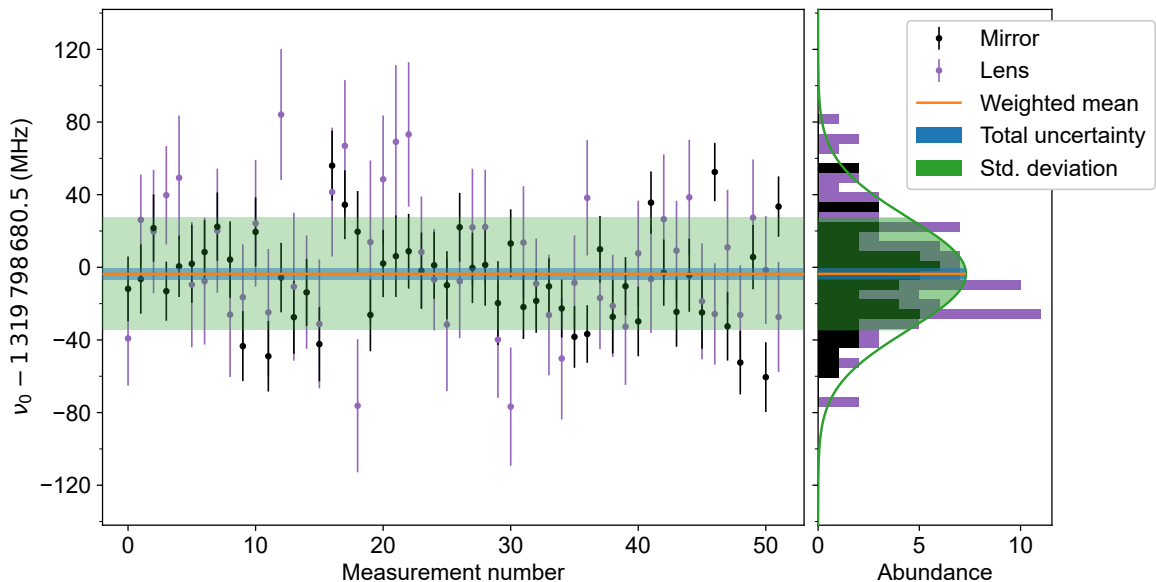


Figure 5.11: Absolute frequencies of the $1s2s\ 3S_1, F = 3/2 \rightarrow 1s2p\ 3P_2, F' = 5/2$ transition determined from the pulsed relative to the final value determined from the continuous operation mode of the EBIS. The value of the continuous mode lies within the 1.2σ -uncertainty region of the combined statistical and systematic uncertainty (blue) of all frequencies from pulsed operation. The standard deviation of the data (green) is plotted to show the dominance of the statistical over the systematic uncertainty. The Gaussian on the right is fitted to the histogram by only varying its amplitude.

from the spectra used to determine the transition frequency. The FWHM of the resonance signal is 1.6 GHz which aligns with the previous findings presented in [63]. The statistics of all measurements and a comparison of results between the pulsed and continuous mode are summarized in Tab. 5.9. The measured transition frequencies of both FDR segments are shown in Fig. 5.11.

The transition frequencies determined from the measurements in pulsed operation agree well with the precise results from continuous operation. The statistical uncertainty is significantly larger in pulsed mode. However, test measurements in [63] showed that the FWHM can be reduced by a factor of 3 by lowering the electron current to 25 mA without reducing the SNR. This can improve the statistical uncertainty and shows that a reduction to the limiting systematic uncertainty of 1.8 MHz in continuous operation at least for this strong transition would be possible. Moreover, the scattering of the determined transition frequencies agrees well with the given fit uncertainties as indicated by the agreement between the uncertainties of the weighted and standard mean. This suggests that the systematic uncertainty in pulsed is not much larger than in continuous operation.

6 Conclusion and outlook

The $1s2s\ ^3S_1 \rightarrow 1s2p\ ^3P_{0,1,2}$ transition frequencies in helium-like $^{13}\text{C}^{4+}$ were determined using quasi-simultaneous collinear-anticollinear laser spectroscopy (CLS). The measurements were carried out at the Collinear Apparatus for Laser Spectroscopy and Applied Science (COALA) located in the Institute for Nuclear Physics at the Technical University of Darmstadt. A continuous beam of $^{13}\text{C}^{4+}$ ions in the metastable 3S_1 state that has a lifetime of only 21 ms was produced in an electron beam ion source (EBIS) and overlapped with two narrow-band continuous-wave lasers. A precision-level of 2 MHz, or 10^{-9} in relative precision, for absolute frequencies in the UV-regime was achieved as in previous measurements of $^{12}\text{C}^{4+}$ [63, 64]. The precision is currently limited by the main systematic uncertainty arising from the interaction of two not perfectly aligned laser beams with ions that have position-correlated momenta due to electrostatic 60°-bending. A small statistical uncertainty in the weakest transitions of the hyperfine structure spectrum of $^{13}\text{C}^{4+}$ was ensured by installing a beam position stabilization for the collinear laser beam whose movement previously caused unwanted time-dependent laser background. Additionally, a background-free measurement scheme was implemented enabling collinear saturation spectroscopy, which could potentially eliminate the dominant systematic uncertainty. However, in the case of C^{4+} , the method was limited by statistics due to the available laser power. The determination of absolute transition frequencies from resonance signals produced in the pulsed operation mode of the EBIS, that have up to 10-times larger peak widths, was demonstrated to reach statistical uncertainties that are on par with the limiting systematic uncertainty.

To improve the data analysis process in collinear laser spectroscopy and determine realistic uncertainties of effects such as photon recoils, the Zeeman effect or quantum interference, the Python package *qspec* was developed within this work. A framework to create modular lineshape models and an object-oriented simulator of laser-atom interactions was introduced. The lineshape models can be combined to address arbitrary compositions of isotopes or isomers across multiple data sets with shared parameters which freely can be constraint as functions of other parameters, by hard bounds or by expectation values with uncertainties. Compared with the well-established *satlas2* package [66, 67], a performance improvement that increases linearly with the number of fitted data sets was shown. The simulation module of *qspec* offers a user-friendly interface to coherently simulate the dynamics of laser-atom interactions that is as easy as drawing a level scheme. Many useful applications requiring knowledge about the electronic state population in an atom can be thought of, such as saturation spectroscopy, driving Raman transitions [148], polarizing ion beams in storage rings [146, 147] or even simulating quantum computers [149]. In this work, quantum interference effects in $^{87}\text{Sr}^+$ were investigated, see App. A.1, and systematic shifts caused by photon recoils and the Zeeman effect were simulated.

The absolute transition frequencies of $^{13}\text{C}^{4+}$ that are accurately determined with the above described efforts depict a hyperfine structure consistent with strong hyperfine-induced mixing. The $^3\text{P}_{0,1}$ states contain admixtures of 0.4359 % of each other while the $^3\text{P}_{1,2}$ states contain 0.0027 % admixtures. The influence of mixing with the $^1\text{P}_1$ state is negligible at the 2-MHz precision level. The experimentally determined hyperfine structure splittings can be used as benchmark values for non-relativistic quantum electrodynamics (NRQED) calculations. Here, NRQED calculations up to the order ma^6 were used to determine the differential mean-square nuclear charge radius $\delta\langle r^2 \rangle^{12,13}$. For this, the isotope shift of the center-of-gravity frequency of all $1s2s\,^3\text{S}_1 \rightarrow 1s2p\,^3\text{P}_{0,1,2}$ transitions, which is unaffected by the hyperfine-induced mixing, was determined by combining the results of this work with the results for $^{12}\text{C}^{4+}$ from [63, 64]. Subtracting the hypothetical isotope shift of point-like nuclei and dividing by the field-shift factor, both determined with NRQED calculations by V. Yerokhin *et. al.* [168], yields

$$\delta\langle r^2 \rangle^{12,13} = \langle r^2 \rangle^{13} - \langle r^2 \rangle^{12} = -0.1245(66) \text{ fm}^2$$

$$\delta R_{\text{C}}^{12,13} = R_{\text{C}}^{13} - R_{\text{C}}^{12} = -0.0253(14) \text{ fm}.$$

These values have three-times smaller uncertainties than the previous most precise result from muonic atom spectroscopy and predict a 1σ larger charge radius difference between $^{12,13}\text{C}$. Although this deviation is still within statistics, the simultaneous over-estimation of the absolute radii of ^{12}C and ^{13}C by muonic atom spectroscopy compared with elastic electron scattering hints at a systematic shift of the muonic results. New measurements with light μ -atoms, planned in the near future, are promising to resolve these discrepancies [170]. The experimentally determined nuclear charge radii were compared to in-medium similarity renormalization group (IMSRG) *ab initio* chiral effective field theory calculations provided by M. Heinz *et. al.* [168]. An agreement with absolute radii at the 3 % level was demonstrated with theoretical radii that are generally too small. The differential radius $\delta R_{\text{C}}^{12,13}$ is generally overestimated in absolute terms and was best reproduced with the novel $\Delta\text{N}^2\text{LO}_{\text{GO}}$ interaction that explicitly considers Δ excitation of nucleons upon pion exchange. The inclusion of effective three-body contributions brings the absolute nuclear charge radii closer to the experimental value while the difference between $^{12,13}\text{C}$ increases further. The uncertainty introduced with the truncation of the IMSRG flow equation at the three-body level will be investigated in the near future.

Measurements of the $1s2s\,^3\text{S}_1 \rightarrow 1s2p\,^3\text{P}_{0,1,2}$ transitions in $^{14}\text{C}^{4+}$, whose radius is only known to the precision of the electron scattering results in ^{13}C , are currently planned at COALA and will help to improve the IMSRG results. More precisely, knowing both $\delta R_{\text{C}}^{12,13}$ and $\delta R_{\text{C}}^{12,14}$ as well as the absolute nuclear charge radii in $^{12-14}\text{C}$ will clarify the predictive power of the IMSRG calculations as $\delta R_{\text{C}}^{12,14}$ will not be affected by odd-even staggering. Furthermore, the fine-structure splittings in ^{14}C will serve as an independent benchmark for atomic structure theory and can be compared to those in ^{12}C [64]. Based on the successful tests of CLS with C^{4+} from the EBIS, the stable $^{10,11}\text{B}$ isotopes will be addressed at COALA to provide absolute reference radii for the search of the proton halo in ^8B , which is planned at the Argonne National Lab (ANL). Apart from the interest of nuclear theory in the halo nucleus, atomic theory especially

benefits from the measurements in the two stable isotopes as in both, helium- and lithium-like $B^{3+,2+}$, electronic transitions in the optical regime are available. The $1s2s\ ^3S_1 \rightarrow 1s2p\ ^3P_{0,1,2}$ transitions in B^{3+} will be used to determine the absolute nuclear charge radii as in $^{12}C^{4+}$ [64], which at the current state will provide the most precisely determined experimental radii in B . Simultaneously, the differential radii between $^{10,11}B$ will be determined from both B^{3+} and the $2s\ ^2S_{1/2} \rightarrow 2p\ ^2P_{1/2,3/2}$ transitions in B^{2+} , as for $^{13}C^{4+}$ in this work, to show the validity of the *ab initio* differential mass shift calculations. Beyond that, helium-like N^{5+} can be investigated. Here, the transitions have wavelengths around 190 nm which constitutes a technical challenge for the laser beam production and transport and also necessitates the use of lens-based fluorescence detection segments, such as the one constructed and commissioned within this work.

A Appendix

A.1 Quantum interference tests in $^{87}\text{Sr}^+$

To test the angle selectivity of the lens-based fluorescence detection region (FDR) segment and the simulation module of the *qspec* package, the hyperfine structure spectrum of the $5s\ ^2\text{S}_{1/2} \rightarrow 5p\ ^2\text{P}_{3/2}$ transition in $^{87}\text{Sr}^+$ was measured for different laser polarizations. A level scheme of $^{87}\text{Sr}^+$ is depicted in Fig. A.1. The polarization can be imagined as a reference axis for the unpolarized ion beam. Photons scattered through resonant excitation are emitted according to a rotational symmetric angular distribution with respect to the polarization axis. Therefore, the selection of a solid angle with the FDR influences the peak heights in a fluorescence spectrum. However, it can also lead to asymmetric peaks in the presence of quantum interference (QI) effects when multiple excited states overlap within their natural linewidths [133]. Additionally, the interaction of the laser with the ions leads to population transfer between the electronic states of the ions, also altering the peak heights. The occurrence of both effects in the hyperfine structure of $^{87}\text{Sr}^+$ can be used to test the theoretical description of the photon scattering rate.

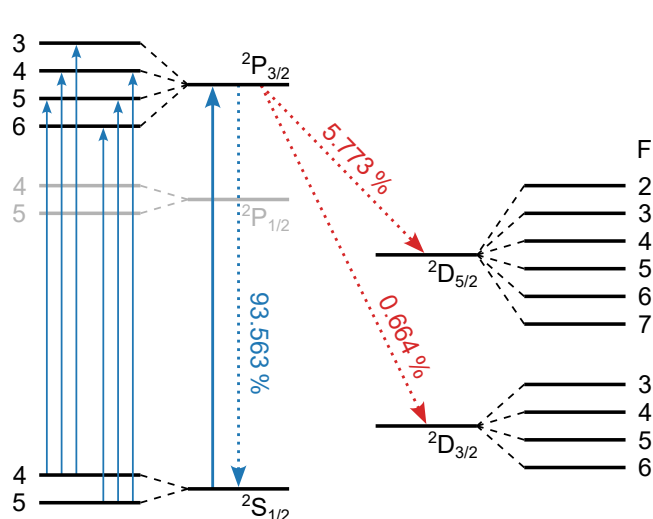


Figure A.1: Level scheme of the $5s\ ^2\text{S}_{1/2}$, $5p\ ^2\text{P}_{1/2,3/2}$ and $4d\ ^2\text{D}_{3/2,5/2}$ states in $^{87}\text{Sr}^+$ and the laser-driven $5s\ ^2\text{S}_{1/2} \rightarrow 5p\ ^2\text{P}_{3/2}$ transition. The $^2\text{P}_{1/2}$ state does not contribute to the population dynamics induced by the interaction with the laser. Population in the $^2\text{P}_{3/2}$ state decays into the $^2\text{S}_{1/2}$ and the $^2\text{D}_{3/2,5/2}$ states. The six transitions corresponding to the visible resonance signals in the fluorescence spectrum of $^{87}\text{Sr}^+$ are shown in blue from left to right.

Experimental setup The continuous beam of Sr^+ ions was produced in the surface ionization source situated at the 10° port of the switchyard of COALA. The production of the laser beam is explained in Sec. 4.4 for measurements with C^{4+} . For Sr^+ , the frequency-doubled 408 nm light behind the first doubling stage was coupled into a polarization-maintaining single-mode fiber to transport the linearly polarized continuous-wave laser beam to the beamline. There, a set consisting of a $\lambda/4$, $\lambda/2$ plate and a linear polarizer was used in that order to control the angle of the linearly polarized light. The $\lambda/4$ plate was only used to optimize the power through the linear polarizer in case the laser beam is not completely linearly polarized after the fiber port. The measurements were performed in anticollinear geometry. In the first test, the laser

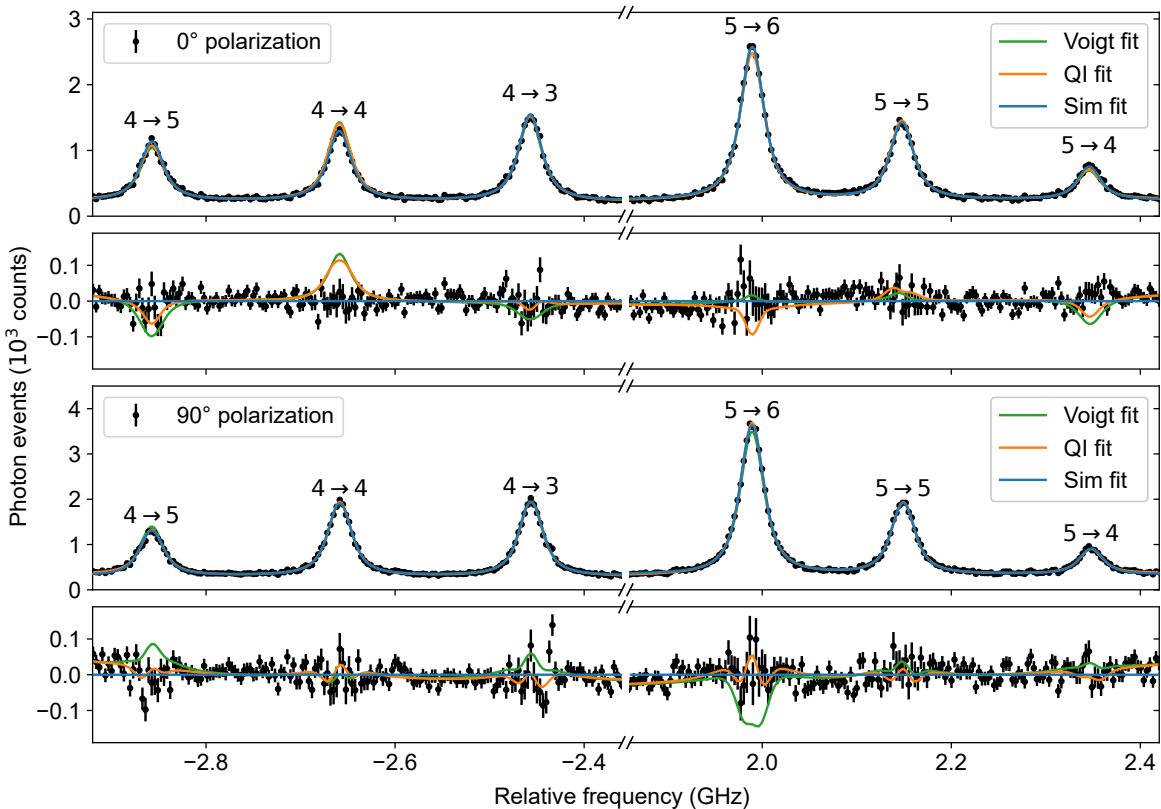


Figure A.2: Hyperfine structure spectrum of the $5s\ 2S_{1/2} \rightarrow 5p\ 2P_{3/2}$ transition in $^{87}\text{Sr}^+$ with a polarization angle of 0° and 90° with respect to the PMTs direction in the FDR recorded with the lens-based FDR segment. A perturbative quantum interference model (orange) and two models that are linear combinations of Voigt profiles, one with Racah coefficients as peak heights (green) and one with peak heights derived from solving the master equation (blue), were fitted to the data. The residuals show the difference between the data points and the Sim fit. For the fits with the other models, also the difference to the Sim fit is depicted, which results in smooth curves that emphasize the differences between the fit models.

power was set to a low value of only $7(1) \mu\text{W}$ to prevent optical population transfer into the metastable $4d^2\text{D}_{3/2,5/2}$ states and the second ground state of the hyperfine structure.

Fit models Figure A.2 shows the hyperfine structure spectrum of the $5s^2\text{S}_{1/2} \rightarrow 5p^2\text{P}_{3/2}$ transition in $^{87}\text{Sr}^+$ with a polarization angle of 0° and 90° relative to the vertical direction which is the optical axis of the lens-based FDR segment. In $^{87}\text{Sr}^+$, no sign of quantum interference was found as fitting a sum of symmetric Voigt profiles yields reasonable agreement with the data. This is expected for the achievable signal-to-noise ratio and the given separation of the excited states. Therefore, here only the emergence of the peak heights was investigated using different fit models. The first model is a sum of Voigt profiles whose peak heights correspond to the theoretical intensities, *i.e.*, the weights also used in Eq. (2.48). Hence, the relative peak heights are completely fixed. The second model considers QI effects using the perturbative approach for the scattering rate described by Eq. (2.90) that is only valid for laser intensities $I \ll I_0$ and when the population of the internal states of the ion are in equilibrium. Here, the

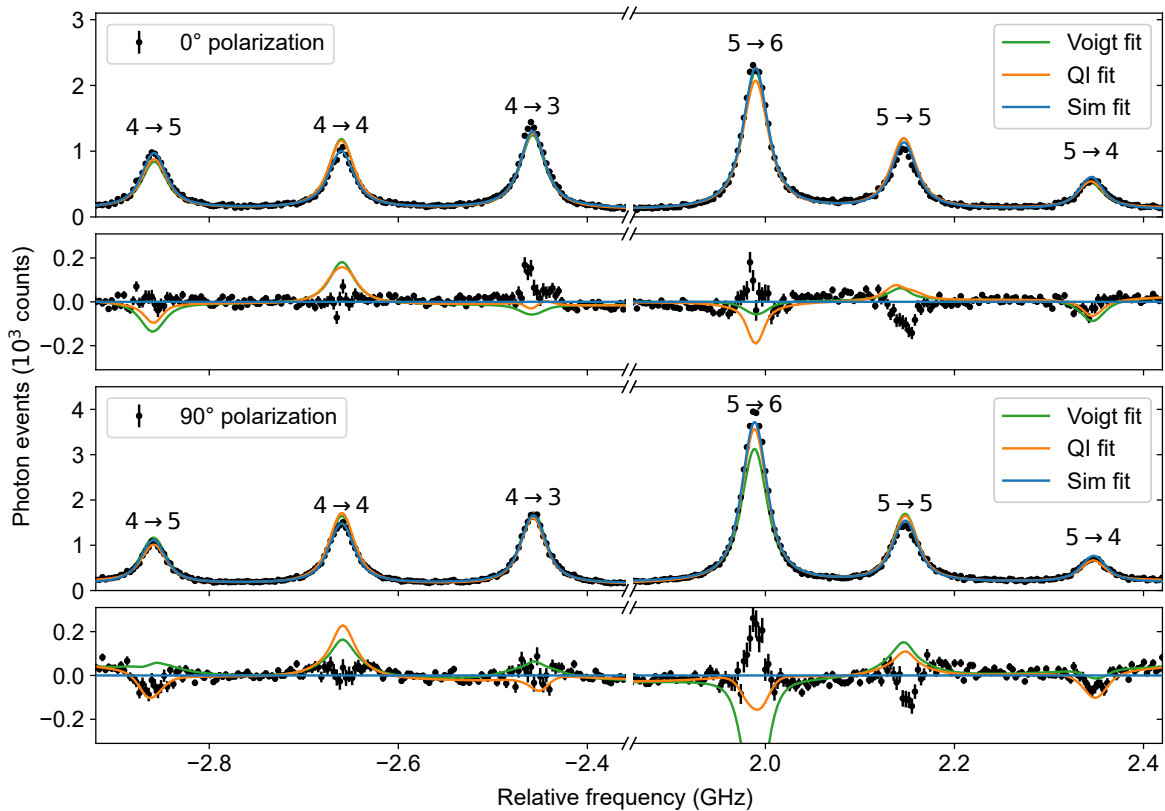


Figure A.3: The same hyperfine structure spectrum as in Fig. A.2 but with $50 \mu\text{W}$ laser power and an extra aperture with a diameter of 20 mm in front of the outer lens in the lens-based FDR segment in order to narrow down the solid angle and thus enhance the sensitivity to quantum interference effects.

relative peak heights are determined by a single fit parameter $p(\mathbf{q}, \mathbf{k}_{\text{sc}})$ that encapsulates the detector geometry. The Voigt profile is generated through a numerical convolution integral of the QI Lorentzians with a Gaussian kernel.

The aforementioned Voigt model with fixed intensities and the QI model are simultaneously fitted to the isotopes $^{86,88}\text{Sr}$ which are just outside the shown frequency range in Fig. A.2. Hence, the scattering rate slightly increases at the borders of the plot. The QI model only has a single Gaussian width parameter σ for all isotopes which is introduced with the numerical convolution. The third model is a sum of Voigt profiles whose peak heights are simulated using the master equation solver of `qspec.simulate` and the differential scattering rate from Eq. (2.89). In this model, the peak heights are governed by two parameters, one for the detector geometry and one for the laser power that controls the rate of the optical population transfer. For the parameter of the detector geometry, the angle between the linear polarization vector and the z -axis, which points towards the PMT, was chosen. The actual detection geometry was not taken into account explicitly. However, this parameter covers the complete value range of the geometry parameter $p(\mathbf{q}, \mathbf{k}_{\text{sc}})$ such that for any detector geometry, there exists a polarization angle so that the lineshape of the differential scattering rate is equal to that integrated over the angle-dependent geometric efficiency. The geometric efficiency for both FDR segments is plotted in Fig. 4.9. The large number of m_F states in the relevant $^2\text{S}_{1/2}$, $^2\text{P}_{1/2,3/2}$ and $^2\text{D}_{3/2,5/2}$ levels in $^{87}\text{Sr}^+$, corresponding to $160^2 = 25\,600$ density matrix elements, requires two simplifications to achieve reasonable computing times. The interaction time of 1 μs passed at the position of the lens-based FDR segment is reduced to 0.2 μs in the simulation. As a consequence, the fitted laser power gets larger to compensate for the shorter interaction time. This is only a valid simplification for small laser powers when the population in the excited state is still proportional to the laser power. Additionally, the scattering rate was only calculated for a single point in time and not integrated over a finite interaction region. In reality, the mirror and the lens systems collect light emitted from the ion beam over a distance of 80

Table A.1: Agreement χ^2_{red} of four different models fitted to the hyperfine structure spectrum of the $5s\,^2\text{S}_{1/2} \rightarrow 5p\,^2\text{P}_{3/2}$ transition in $^{87}\text{Sr}^+$. The Free, Voigt and Sim fits all use sum of Voigt profiles with differently calculated amplitudes. The QI fit considers quantum interference effects (QI) and is numerically convoluted with a Gaussian. For details about the models, see text.

FDR segment	Laser power (μW)	Polarization	Free fit	Voigt fit	QI fit	Sim fit
mirror	7(1)	0°	1.29	1.47	1.41	1.46
mirror	7(1)	90°	1.32	1.80	1.80	1.47
lens	7(1)	0°	1.20	1.97	1.76	1.29
lens	7(1)	90°	1.17	1.73	1.20	1.38
mirror	50(3)	0°	3.22	16.99	15.89	7.62
mirror	50(3)	90°	5.83	64.40	50.29	8.89
lens	50(3)	0°	1.92	4.62	4.28	2.30
lens	50(3)	90°	1.85	6.96	3.60	2.57

and 20 mm, respectively, as shown in Fig. 4.8. During the time-of-flight over these distances, the population of the states changes such that the time-integrated scattering rate may not be reproducible with a scattering at a single point in time.

Fit results All three models approximately agree with the data but show slight deviations as can be seen from the residuals in Fig. A.2 and the χ^2_{red} listed in Tab. A.1. However, only the simulation model is able to correctly describe the peak height of the $F = 4 \rightarrow F' = 4$ resonance for 0° polarization. For this polarization, the peak height decreases due to both, the detection geometry of the FDR segment and optical population transfer. For 90° on the other hand, the angular contribution increases the peak height, counteracting the population transfer and leading to a better agreement with the perturbative QI model. A second measurement series was conducted with a larger laser power of 50(3) μW and a decreased angular detection range by adding a 20-mm aperture between the window of the vacuum viewport and the outer

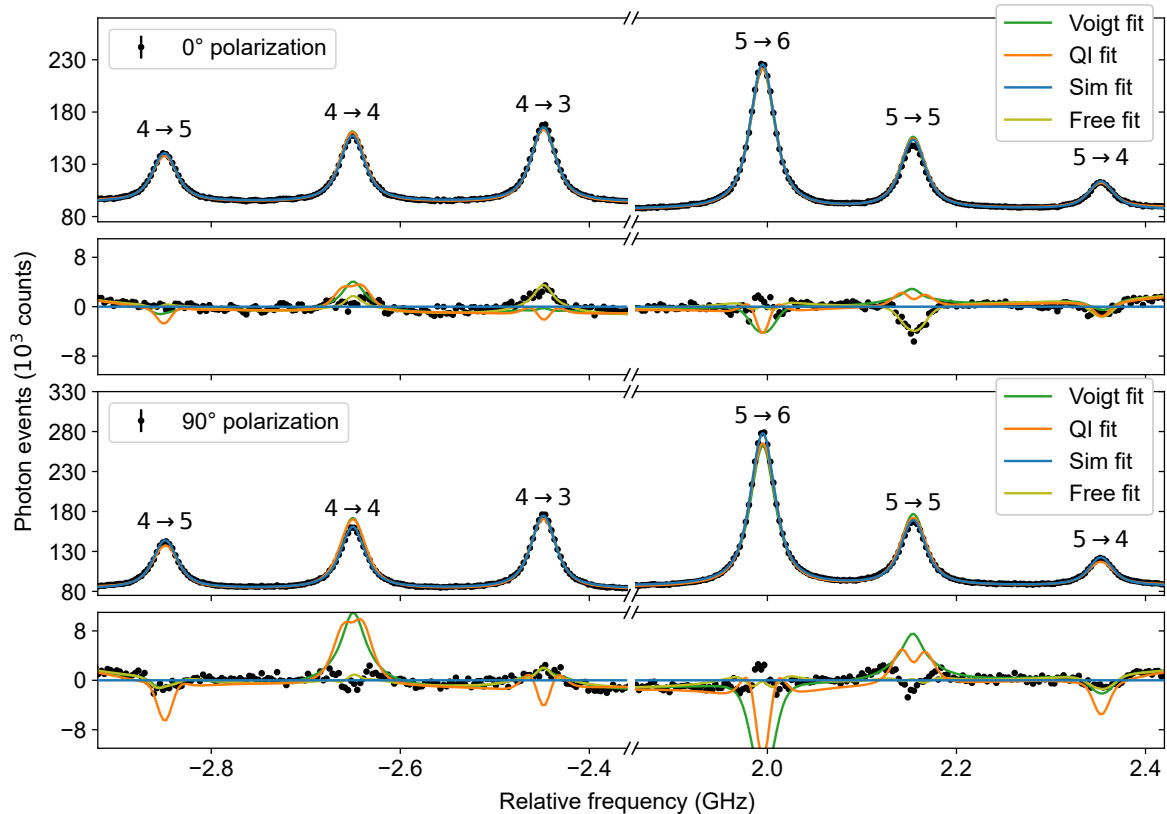


Figure A.4: Hyperfine structure spectrum of the $5s\ ^2S_{1/2} \rightarrow 5p\ ^2P_{3/2}$ transition in $^{87}\text{Sr}^+$ with a polarization angle of 0° and 90° recorded with the elliptical mirror FDR segment. The Voigt and the QI model show significant deviations from the experimental peak heights while the Sim model yields results that are close to those of a Voigt with free peak intensities (yellow).

lens of the lens-based FDR segment. This increases both, the optical population transfer and QI effects. The resulting spectra are shown in Fig. A.3. Indeed, a bigger difference can be seen between the two polarizations and the agreement of the two models that do not consider pumping effects compared with the simulation model. However, none of the models is able to describe the peak heights of the transitions from the $F = 5$ ground states correctly which seems to be originating mainly from an underestimation of the $5 \rightarrow 6$ transition. This transition is closed with respect to transferring population from the $F = 5$ to the $F = 4$ ground state and thus, is expected to get stronger relative to the other transitions over time.

In Fig. A.4, the fluorescence spectra recorded with the elliptical mirror segment for 0° and 90° polarization are shown. Here the optical population transfer is even stronger than in the lens-based segment, possibly owing to the longer interaction time of the ion with the laser during which fluorescence photons are detected. Therefore, the Voigt model with fixed relative intensities and the QI model significantly deviate from the data. However, the Sim model is still able to describe the data relatively well. To test how well the peaks are described by a Voigt profile, the Voigt model was additionally fitted with free peak intensities. While this model can describe the peak intensities slightly better than the Sim model, it slightly deviates from the experimental data in the same transitions, compare also the χ^2_{red} in Tab. A.1. This is a clear indication that a Voigt profile, which was used in all fit models, is not a sufficient description of the experimental lineshape. Hence, this could be the main origin of the discrepancy between the data and the Sim model, which only uses the solution of the master equation for the relative scattering rates at the resonance centers. Therefore, a fit of the master equation to the full spectrum would be desirable which, however, is currently not feasible with the complex system of $^{87}\text{Sr}^+$ in an acceptable computing time.

Polarization sensitivity Although optical population transfer is not considered in the perturbative QI model, it can still be used to test the sensitivity of the fluorescence signals of an FDR segment to the laser polarization. Figure A.5 shows the QI parameter $p(\mathbf{q}, \mathbf{k}_{\text{sc}})$ from Eq. (2.90) in dependence of the polarization angle for the elliptical mirror and the lens-based FDR segment. The function

$$f(x, a, b, c) = a \cos^2(x - c) + b \quad (\text{A.1})$$

was fitted to the data. While the elliptical mirror segment is almost completely insensitive to the polarization, owing to a 4π solid angle of detection, the lens-based segment clearly shows a polarization-dependence. The amplitude of the oscillation corresponds to $\sim 1/4$ of the maximum possible value when no aperture is used and to $\sim 1/2$ for the 20 mm aperture. A shift of the parameter $p(\mathbf{q}, \mathbf{k}_{\text{sc}})$ to smaller values is found that can be explained with optical population transfer, which also changes the peak heights of the fluorescence spectrum.

In conclusion, the test with $^{87}\text{Sr}^+$ shows that the simultaneous description of QI and optical population transfer effects with *qspec.simulate* can explain the emergence of the relative peak heights in hyperfine structure spectra. However, for the complex system of $^{87}\text{Sr}^+$, simplifications were required that may have lead to discrepancies to the experimental scattering rate when

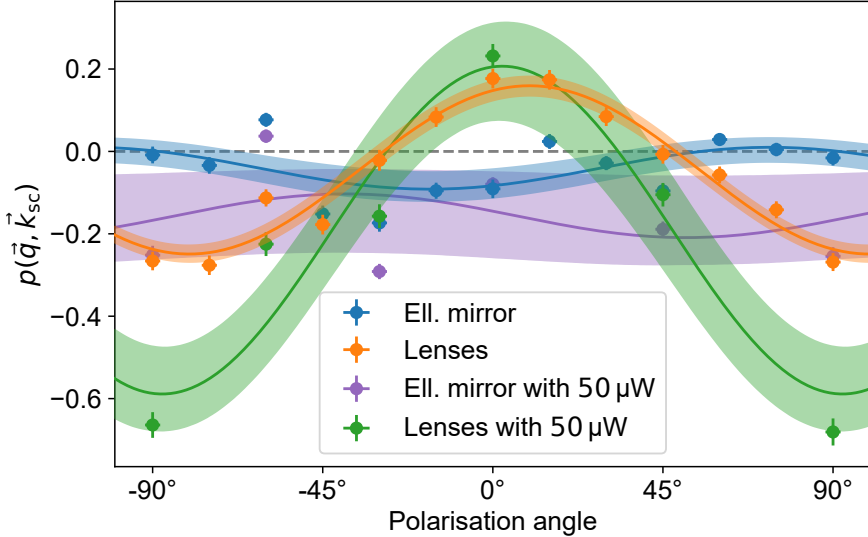


Figure A.5: The geometric parameter $p(q, \vec{k}_{sc})$ from Eq. (2.90) in dependence of the angle between the linearly polarized laser light and the optical axis of the lens-based FDR segment. The amplitude of the oscillation is a measure of the polarization sensitivity of an FDR segment. The shaded area shows the 1σ uncertainty region of the fit of Eq. (A.1) to the data. For the measurement with $50 \mu\text{W}$, the solid angle of detection of the lens-based FDR segment was reduced, increasing QI effects.

there is much population transfer. Therefore, additional tests are needed with a simpler system that preferably has a narrow hyperfine structure to amplify QI effects. One case could be the D_2 line in $^{6,7}\text{Li}$, which requires a charge exchange cell currently in development. The polarization sensitivity of the elliptical mirror and the lens-based FDR segments were tested by rotating the linear polarization vector of the incident laser beam. A polarization-sensitivity of the lens-based segment was found that is small enough to be able to ignore QI effects in most measurements but can be easily amplified by limiting the lens aperture in order to investigate or even utilize QI effects. It was suggested by different authors to use QI effects to unambiguously identify hyperfine structure peaks of different isotopes that are overlapping and that may not be resolved at all in a certain detector geometry [133, 176, 177]. A QI-sensitive FDR could be used, *e.g.*, in ^{26}Al , to improve the precision of the isomer shift between the $I = 0$ isomeric state and the $I = 5$ ground state, which was recently used to test the completeness of the quark-mixing Cabibbo-Kobayashi-Maskawa matrix of the Standard Model [144]. The *qspec* package developed within this work contains the necessary tools to intensively investigate this possibility.

Bibliography

- [1] M. G. Mayer, “On Closed Shells in Nuclei”, *Physical Review* **74**, 235 (1948).
- [2] O. Haxel, J. H. D. Jensen, and H. E. Suess, “On the “Magic Numbers” in Nuclear Structure”, *Physical Review* **75**, 1766 (1949).
- [3] S. Weinberg, “The making of the Standard Model”, *The European Physical Journal C* **34**, 5 (2004).
- [4] M. Riordan, “The discovery of quarks”, *Science* **256**, 1287 (1992).
- [5] S. Weinberg, “Phenomenological Lagrangians”, *Physica A: Statistical Mechanics and its Applications* **96**, 327 (1979).
- [6] K. Hebeler, “Three-nucleon forces: Implementation and applications to atomic nuclei and dense matter”, *Physics Reports* **890**, 1 (2021).
- [7] H. Hergert, “A Guided Tour of *ab initio* Nuclear Many-Body Theory”, *Frontiers in Physics* **8**, 379 (2020).
- [8] S. R. Stroberg, J. D. Holt, A. Schwenk, and J. Simonis, “*Ab initio* limits of atomic nuclei”, *Physical Review Letters* **126**, 022501 (2021).
- [9] R. Neugart, “Laser spectroscopy on mass-separated radioactive beams”, *Nuclear Instruments and Methods in Physics Research* **186**, 165 (1981).
- [10] E. W. Otten, “Nuclear Radii and Moments of Unstable Isotopes”, in *Treatise on heavy ion science*, edited by D. A. Bromley (Springer Boston, 1989), pp. 517–638.
- [11] K. Blaum, J. Dilling, and W. Nörtershäuser, “Precision atomic physics techniques for nuclear physics with radioactive beams”, *Physica Scripta* **T152**, 014017 (2013).
- [12] P. Campbell, I. D. Moore, and M. R. Pearson, “Laser spectroscopy for nuclear structure physics”, *Progress in Particle and Nuclear Physics* **86**, 127 (2016).
- [13] R. Neugart, J. Billowes, M. L. Bissell, K. Blaum, B. Cheal, K. T. Flanagan, G. Neyens, W. Nörtershäuser, and D. T. Yordanov, “Collinear laser spectroscopy at ISOLDE: new methods and highlights”, *Journal of Physics G* **44**, 064002 (2017).
- [14] J. A. Wheeler, “On the Mathematical Description of Light Nuclei by the Method of Resonating Group Structure”, *Physical Review* **52**, 1107 (1937).
- [15] C. F. v. Weizsäcker, “Neuere Modellvorstellungen über den Bau der Atomkerne”, *Naturwissenschaften* **26**, 209 (1938).
- [16] Y. Kanada-En’yo and H. Horiuchi, “Structure of Light Unstable Nuclei Studied with Antisymmetrized Molecular Dynamics”, *Progress of Theoretical Physics Supplement* **142**, 205 (2001).

[17] K. Ikeda, N. Takigawa, and H. Horiuchi, “The Systematic Structure-Change into the Molecule-like Structures in the Self-Conjugate $4n$ Nuclei”, *Progress of Theoretical Physics Supplement* **E68**, 464 (1968).

[18] W. von Oertzen, M. Freer, and Y. Kanada En’Yo, “Nuclear clusters and nuclear molecules”, *Physics Reports* **432**, 43 (2006).

[19] W. Nörtershäuser, T. Neff, R. Sánchez, and I. Sick, “Charge radii and ground state structure of lithium isotopes: Experiment and theory reexamined”, *Physical Review C* **84**, 024307 (2011).

[20] A. Krieger, W. Nörtershäuser, C. Geppert, K. Blaum, M. L. Bissell, N. Frömmgen, M. Hamm, K. Kreim, M. Kowalska, J. Krämer, *et al.*, “Frequency-comb referenced collinear laser spectroscopy of Be^+ for nuclear structure investigations and many-body QED tests”, *Applied Physics B* **123**, 15 (2017).

[21] B. Maaß, T. Hüther, K. König, J. Krämer, J. Krause, A. Lovato, P. Müller, K. Pachucki, M. Puchalski, R. Roth, *et al.*, “Nuclear Charge Radii of $^{10,11}\text{B}$ ”, *Physical Review Letters* **122**, 182501 (2019).

[22] T. Neff and H. Feldmeier, “Cluster structures within Fermionic Molecular Dynamics”, *Nuclear Physics A* **738**, 357 (2004).

[23] M. Chernykh, H. Feldmeier, T. Neff, P. von Neumann-Cosel, and A. Richter, “Structure of the Hoyle state in ^{12}C ”, *Physical Review Letters* **98**, 032501 (2007).

[24] E. Epelbaum, H. Krebs, T. A. Lähde, D. Lee, and U.-G. Meißner, “Structure and rotations of the Hoyle state”, *Physical Review Letters* **109**, 252501 (2012).

[25] T. Otsuka, T. Abe, T. Yoshida, Y. Tsunoda, N. Shimizu, N. Itagaki, Y. Utsuno, J. Vary, P. Maris, and H. Ueno, “ α -Clustering in atomic nuclei from first principles with statistical learning and the Hoyle state character”, *Nature Communications* **13**, 2234 (2022).

[26] D. Dell’Aquila, “Experimental studies of clustering in light nuclei: $^{11,12,13,16}\text{C}$ ”, *The European Physical Journal Plus* **135**, 165 (2020).

[27] M. Freer, A. H. Wuosmaa, R. R. Betts, D. J. Henderson, P. Wilt, R. W. Zurmühle, D. P. Balamuth, S. Barrow, D. Benton, Q. Li, *et al.*, “Limits for the 3α branching ratio of the decay of the 7.65 MeV, 0_2^+ state in ^{12}C ”, *Physical Review C* **49**, R1751 (1994).

[28] O. S. Kirsebom, M. Alcorta, M. J. G. Borge, M. Cubero, C. A. Diget, L. M. Fraile, B. R. Fulton, H. O. U. Fynbo, D. Galaviz, B. Jonson, *et al.*, “Improved limit on direct α decay of the Hoyle state”, *Physical Review Letters* **108**, 202501 (2012).

[29] S. Jin, L. F. Roberts, S. M. Austin, and H. Schatz, “Enhanced triple- α reaction reduces proton-rich nucleosynthesis in supernovae”, *Nature* **588**, 57 (2020).

[30] T. W. Bonner, A. A. Kraus, J. B. Marion, and J. P. Schiffer, “Neutrons and Gamma Rays from the Alpha-Particle Bombardment of Be^9 , B^{10} , B^{11} , C^{13} , and O^{18} ”, *Physical Review* **102**, 1348 (1956).

[31] R. B. Taylor, N. R. Fletcher, and R. H. Davis, “Elastic scattering of 4-20 MeV alpha particles by Be^9 ”, *Nuclear Physics* **65**, 318 (1965).

[32] H. D. Knox and R. O. Lane, “Structure of ^{13}C from an R -matrix analysis of $^{12}\text{C} + \text{n}$ scattering and reaction cross sections”, Nuclear Physics A **378**, 503 (1982).

[33] X. Aslanoglou, K. W. Kemper, P. C. Farina, and D. E. Trcka, “Location of major α strength in ^{13}C at 10.75 MeV”, Physical Review C **40**, 73 (1989).

[34] L. S. Cardman, J. W. Lightbody, S. Penner, S. P. Fivozinsky, X. K. Maruyama, W. P. Trower, and S. E. Williamson, “The charge distribution of ^{12}C ”, Physics Letters B **91**, 203 (1980).

[35] I. Sick, “Precise nuclear radii from electron scattering”, Physics Letters B **116**, 212 (1982).

[36] W. Reuter, G. Fricke, K. Merle, and H. Miska, “Nuclear charge distribution and rms radius of ^{12}C from absolute elastic electron scattering measurements”, Physical Review C **26**, 806 (1982).

[37] E. A. Offermann, L. S. Cardman, C. W. de Jager, H. Miska, C. de Vries, and H. de Vries, “Energy dependence of the form factor for elastic electron scattering from ^{12}C ”, Physical Review C **44**, 1096 (1991).

[38] L. A. Schaller, L. Schellenberg, T. Q. Phan, G. Piller, A. Ruetschi, and H. Schneuwly, “Nuclear charge radii of the carbon isotopes ^{12}C , ^{13}C and ^{14}C ”, Nuclear Physics A **379**, 523 (1982).

[39] W. Ruckstuhl, B. Aas, W. Beer, I. Beltrami, K. Bos, P. Goudsmit, H. J. Leisi, G. Strassner, A. Vacchi, F. de Boer, *et al.*, “Precision measurement of the 2p-1s transition in muonic ^{12}C : Search for new muon-nucleon interactions or accurate determination of the rms nuclear charge radius”, Nuclear Physics A **430**, 685 (1984).

[40] J. Heisenberg, J. S. McCarthy, and I. Sick, “Elastic electron scattering from ^{13}C ”, Nuclear Physics A **157**, 435 (1970).

[41] F. de Boer, B. Aas, P. Baertschi, W. Beer, I. Beltrami, K. Bos, P. Goudsmit, U. Kiebele, B. Jeckelmann, H. J. Leisi, *et al.*, “Precision measurement of the 2p-1s transition wavelength in muonic ^{13}C ”, Nuclear Physics A **444**, 589 (1985).

[42] I. Tanihata and B. Jonson, “Halo Nuclei”, in *Handbook of nuclear physics*, edited by I. Tanihata, H. Toki, and T. Kajino (Springer Nature Singapore, 2023), pp. 985–1026.

[43] I. Tanihata, H. Hamagaki, O. Hashimoto, Y. Shida, N. Yoshikawa, K. Sugimoto, O. Yamakawa, T. Kobayashi, and N. Takahashi, “Measurements of interaction cross sections and nuclear radii in the light p -shell region”, Physical Review Letters **55**, 2676 (1985).

[44] N. B. Shulgina, B. Jonson, and M. V. Zhukov, “ ^{11}Li structure from experimental data”, Nuclear Physics A **825**, 175 (2009).

[45] G. Ewald, W. Nörtershäuser, A. Dax, S. Götte, R. Kirchner, H.-J. Kluge, T. Kühl, R. Sanchez, A. Wojtaszek, B. A. Bushaw, *et al.*, “Nuclear charge radii of $^{8,9}\text{Li}$ determined by laser spectroscopy”, Physical Review Letters **93**, 113002 (2004).

[46] R. Sánchez, W. Nörtershäuser, G. Ewald, D. Albers, J. Behr, P. Bricault, B. A. Bushaw, A. Dax, J. Dilling, M. Dombsky, *et al.*, “Nuclear charge radii of $^{9,11}\text{Li}$: the influence of halo neutrons”, Physical Review Letters **96**, 033002 (2006).

[47] R. Neugart, D. L. Balabanski, K. Blaum, D. Borremans, P. Himpe, M. Kowalska, P. Lievens, S. Mallion, G. Neyens, N. Vermeulen, *et al.*, “Precision measurement of ^{11}Li moments: Influence of halo neutrons on the ^9Li core”, *Physical Review Letters* **101**, 132502 (2008).

[48] A. Krieger, K. Blaum, M. L. Bissell, N. Frömmgen, C. Geppert, M. Hammen, K. Kreim, M. Kowalska, J. Krämer, T. Neff, *et al.*, “Nuclear charge radius of ^{12}Be ”, *Physical Review Letters* **108**, 142501 (2012).

[49] M. Labiche, N. A. Orr, F. M. Marqués, J. C. Angélique, L. Axelsson, B. Benoit, U. C. Bergmann, M. J. Borge, W. N. Catford, S. P. Chappell, *et al.*, “Halo structure of ^{14}Be ”, *Physical Review Letters* **86**, 600 (2001).

[50] S. Takeuchi, S. Shimoura, T. Motobayashi, H. Akiyoshi, Y. Ando, N. Aoi, Z. Fü, T. Gomi, Y. Higurashi, M. Hirai, *et al.*, “Isobaric analog state of ^{14}Be ”, *Physics Letters B* **515**, 255 (2001).

[51] K. T. Schmitt, K. L. Jones, A. Bey, S. H. Ahn, D. W. Bardayan, J. C. Blackmon, S. M. Brown, K. Y. Chae, K. A. Chipps, J. A. Cizewski, *et al.*, “Halo Nucleus ^{11}Be : A Spectroscopic Study via Neutron Transfer”, *Physical Review Letters* **108**, 192701 (2012).

[52] T. Aumann, A. Navin, D. P. Balamuth, D. Bazin, B. Blank, B. A. Brown, J. E. Bush, J. A. Caggiano, B. Davids, T. Glasmacher, *et al.*, “One-Neutron Knockout from Individual Single-Particle States of ^{11}Be ”, *Physical Review Letters* **84**, 35 (2000).

[53] M. Schmidt, L. Platter, and H.-W. Hammer, “Neutron transfer reactions in halo effective field theory”, *Physical Review C* **99**, 054611 (2019).

[54] T. Minamisono, T. Ohtsubo, I. Minami, S. Fukuda, A. Kitagawa, M. Fukuda, K. Matsuta, Y. Nojiri, S. Takeda, H. Sagawa, *et al.*, “Proton halo of ^8B disclosed by its giant quadrupole moment”, *Physical Review Letters* **69**, 2058 (1992).

[55] T. Sumikama, T. Nagatomo, M. Ogura, T. Iwakoshi, Y. Nakashima, H. Fujiwara, K. Matsuta, T. Minamisono, M. Fukuda, and M. Mihara, “Electric quadrupole moment of the proton halo nucleus ^8B ”, *Physical Review C* **74**, 024327 (2006).

[56] W. Schwab, H. Geissel, H. Lenske, K.-H. Behr, A. Brnle, K. Burkard, H. Irnich, T. Kobayashi, G. Kraus, A. Magel, *et al.*, “Observation of a proton halo in ^8B ”, *Zeitschrift für Physik* **350**, 283 (1995).

[57] J. H. Kelley, S. M. Austin, A. Azhari, D. Bazin, J. A. Brown, H. Esbensen, M. Fauerbach, M. Hellström, S. E. Hirzebruch, R. A. Kryger, *et al.*, “Study of the Breakup Reaction $^8\text{B} \rightarrow ^7\text{Be} + p$: Absorption Effects and $E2$ Strength”, *Physical Review Letters* **77**, 5020 (1996).

[58] F. Negoita, C. Borcea, F. Carstoiu, M. Lewitowicz, M. G. Saint-Laurent, R. Anne, D. Bazin, J. M. Corre, P. Roussel-Chomaz, V. Borrel, *et al.*, “ ^8B proton halo via reaction and breakup cross section measurements”, *Physical Review C* **54**, 1787 (1996).

[59] M. H. Smedberg, T. Baumann, T. Aumann, L. Axelsson, U. Bergmann, M. Borge, D. Cortina-Gil, L. M. Fraile, H. Geissel, L. Grigorenko, *et al.*, “New results on the halo structure of ^8B ”, *Physics Letters B* **452**, 1 (1999).

[60] A. V. Dobrovolsky, G. A. Korolev, A. G. Inglessi, G. D. Alkhazov, G. Colò, I. Dillmann, P. Egelhof, A. Estradé, F. Farinon, H. Geissel, *et al.*, “Nuclear-matter distribution in the proton-rich nuclei ${}^7\text{Be}$ and ${}^8\text{B}$ from intermediate energy proton elastic scattering in inverse kinematics”, Nuclear Physics A **989**, 40 (2019).

[61] K. König, J. Krämer, C. Geppert, P. Ingram, B. Maaß, T. Ratajczyk, and W. Nörtershäuser, “A new Collinear Apparatus for Laser Spectroscopy and Applied Science (COALA)”, Review of Scientific Instruments **91**, 081301 (2020).

[62] P. Ingram, K. König, B. Maaß, P. Müller, and W. Nörtershäuser, “Collinear laser spectroscopy of highly charged ions produced with an electron-beam ion source”, Physical Review A **108**, 062809 (2023).

[63] P. Ingram, “High-precision laser spectroscopy of helium-like carbon ${}^{12}\text{C}^{4+}$ ”, Doctoral thesis (PhD thesis) (Technische Universität Darmstadt, 2023).

[64] P. Ingram, K. König, B. Maaß, P. Müller, and W. Nörtershäuser, “Collinear Laser Spectroscopy of ${}^2\text{S}_1 \rightarrow {}^2\text{P}_J$ transitions in helium-like ${}^{12}\text{C}^{4+}$ ”, Physical Review Letters **131**, 243001 (2023).

[65] V. A. Yerokhin, V. Patkóš, and K. Pachucki, “QED calculations of energy levels of heliumlike ions with $5 \leq Z \leq 30$ ”, Physical Review A **106**, 022815 (2022).

[66] W. Gins, R. P. de Groote, M. L. Bissell, C. Granados Buitrago, R. Ferrer, K. M. Lynch, G. Neyens, and S. Sels, “Analysis of counting data: Development of the SATLAS Python package”, Computer Physics Communications **222**, 286 (2018).

[67] W. Gins, B. van den Borne, R. P. de Groote, and G. Neyens, “SATLAS2: An update to the package for analysis of counting data”, Computer Physics Communications **297**, 109053 (2023).

[68] F. G. Kondev, M. Wang, W. J. Huang, S. Naimi, and G. Audi, “The NUBASE2020 evaluation of nuclear physics properties”, Chinese Physics C **45**, 030001 (2021).

[69] M. Wang, W. J. Huang, F. G. Kondev, G. Audi, and S. Naimi, “The AME 2020 atomic mass evaluation (II). Tables, graphs and references”, Chinese Physics C **45**, 030003 (2021).

[70] N. J. Stone, “Table of recommended nuclear magnetic dipole moments”, International Atomic Energy Agency (IAEA), 2019.

[71] E. Epelbaum, H.-W. Hammer, and U.-G. Meißner, “Modern theory of nuclear forces”, Reviews of Modern Physics **81**, 1773 (2009).

[72] H.-W. Hammer, S. König, and U. van Kolck, “Nuclear effective field theory: Status and perspectives”, Reviews of Modern Physics **92**, 025004 (2020).

[73] S. Dürr, Z. Fodor, J. Frison, C. Hoelbling, R. Hoffmann, S. D. Katz, S. Krieg, T. Kurth, L. Lellouch, T. Lippert, *et al.*, “Ab initio determination of light hadron masses”, Science **322**, 1224 (2008).

[74] S. Elhatisari, L. Bovermann, E. Epelbaum, D. Frame, F. Hildenbrand, M. Kim, Y. Kim, H. Krebs, T. A. Lähde, D. Lee, *et al.*, “Wave function matching for the quantum many-body problem”, arXiv.2210.17488 (2022).

[75] K. König, J. C. Berengut, A. Borschevsky, A. Brinson, B. A. Brown, A. Dockery, S. Elhatisari, E. Eliav, R. F. G. Ruiz, J. D. Holt, *et al.*, “Nuclear charge radii of silicon isotopes”, arXiv.2309.02037 (2023).

[76] R. B. Wiringa, R. A. Smith, and T. L. Ainsworth, “Nucleon-nucleon potentials with and without $\Delta(1232)$ degrees of freedom”, *Physical Review C* **29**, 1207 (1984).

[77] R. B. Wiringa, V. G. Stoks, and R. Schiavilla, “Accurate nucleon-nucleon potential with charge-independence breaking”, *Physical Review C* **51**, 38 (1995).

[78] S. C. Pieper, “The Illinois Extension to the Fujita-Miyazawa Three-Nucleon Force”, *AIP Conf. Proc.* **1011**, 143 (2008).

[79] R. L. Workman, V. D. Burkert, V. Crede, E. Klempert, U. Thoma, L. Tiator, K. Agashe, G. Aielli, B. C. Allanach, C. Amsler, *et al.*, “Review of Particle Physics”, *Progress of Theoretical and Experimental Physics* **2022**, 083C01 (2022).

[80] J. Goldstone, “Field theories with « Superconductor » solutions”, *Il Nuovo Cimento* **19**, 154 (1961).

[81] J. Goldstone, A. Salam, and S. Weinberg, “Broken Symmetries”, *Physical Review* **127**, 965 (1962).

[82] B. Povh, K. Rith, C. Scholz, F. Zetsche, and W. Rodejohann, *Particles and Nuclei*, (Springer Berlin Heidelberg, 2015).

[83] A. Faessler, “Interaction between two baryons and the six quark model”, *Progress in Particle and Nuclear Physics* **20**, 151 (1988).

[84] M. Albaladejo and J. A. Oller, “Size of the σ meson and its nature”, *Physical Review D* **86**, 034003 (2012).

[85] J. R. Peláez, “From controversy to precision on the sigma meson: A review on the status of the non-ordinary $f_0(500)$ resonance”, *Physics Reports* **658**, 1 (2016).

[86] N. Fettes and U.-G. Meißner, “Pion–nucleon scattering in an effective chiral field theory with explicit spin- fields”, *Nuclear Physics A* **679**, 629 (2001).

[87] U.-G. Meißner and A. Rusetsky, *Effective Field Theories*, (Cambridge University Press, 2022).

[88] S. K. Bogner, R. J. Furnstahl, and R. J. Perry, “Similarity renormalization group for nucleon-nucleon interactions”, *Physical Review C* **75**, 061001 (2007).

[89] S. K. Bogner, R. J. Furnstahl, and A. Schwenk, “From low-momentum interactions to nuclear structure”, *Progress in Particle and Nuclear Physics* **65**, 94 (2010).

[90] M. Heinz, A. Tichai, J. Hoppe, K. Hebeler, and A. Schwenk, “In-medium similarity renormalization group with three-body operators”, *Physical Review C* **103**, 044318 (2021).

[91] H. Hergert, S. K. Bogner, T. D. Morris, A. Schwenk, and K. Tsukiyama, “The In-Medium Similarity Renormalization Group: A novel *ab initio* method for nuclei”, *Physics Reports* **621**, 165 (2016).

[92] G. P. Kamuntavičius, “Root-mean-square radii of light atomic nuclei: Neutron skin”, *Physical Review C* **56**, 191 (1997).

[93] J. Hoppe, C. Drischler, K. Hebeler, A. Schwenk, and J. Simonis, “Probing chiral interactions up to next-to-next-to-next-to-leading order in medium-mass nuclei”, *Physical Review C* **100**, 024318 (2019).

[94] R. Pohl, A. Antognini, F. Nez, F. D. Amaro, F. Biraben, J. M. R. Cardoso, D. S. Covita, A. Dax, S. Dhawan, L. M. P. Fernandes, *et al.*, “The size of the proton”, *Nature* **466**, 213 (2010).

[95] A. Beyer, L. Maisenbacher, A. Matveev, R. Pohl, K. Khabarova, A. Grinin, T. Lamour, D. C. Yost, T. W. Hänsch, N. Kolachevsky, *et al.*, “The Rydberg constant and proton size from atomic hydrogen”, *Science* **358**, 79 (2017).

[96] A. Ong, J. C. Berengut, and V. V. Flambaum, “Effect of spin-orbit nuclear charge density corrections due to the anomalous magnetic moment on halonuclei”, *Physical Review C* **82**, 014320 (2010).

[97] A. Kramida, Y. Ralchenko, J. Reader, and NIST ASD Team, *NIST Atomic Spectra Database (ver. 5.10)*, National Institute of Standards and Technology, Gaithersburg, MD, 2022.

[98] M. K. Gaillard, J. Maxwell Irvine, E. Lohrmann, V. Lüth, A. Richter, and K. L. G. Heyde, *The Nuclear Shell Model*, (Springer Berlin Heidelberg, 1990).

[99] W. R. Johnson, K. T. Cheng, and D. R. Plante, “Hyperfine structure of 2^3P levels of heliumlike ions”, *Physical Review A* **55**, 2728 (1997).

[100] G. Drake, *Springer Handbook of Atomic, Molecular, and Optical Physics*, (Springer New York, 2006).

[101] V. V. Flambaum and A. J. Mansour, “Enhanced magnetic quadrupole moments in nuclei with octupole deformation and their CP -violating effects in molecules”, *Physical Review C* **105**, 065503 (2022).

[102] C. J. Ho, J. Lim, B. E. Sauer, and M. R. Tarbutt, “Measuring the nuclear magnetic quadrupole moment in heavy polar molecules”, *Frontiers in Physics* **11**, 1086980 (2023).

[103] J. E. Rosenthal and G. Breit, “The Isotope Shift in Hyperfine Structure”, *Physical Review* **41**, 459 (1932).

[104] M. F. Crawford and A. L. Schawlow, “Electron-Nuclear Potential Fields from Hyperfine Structure”, *Physical Review* **76**, 1310 (1949).

[105] E. C. Seltzer, “K X-Ray Isotope Shifts”, *Physical Review* **188**, 1916 (1969).

[106] A. Bohr and V. F. Weisskopf, “The Influence of Nuclear Structure on the Hyperfine Structure of Heavy Elements”, *Physical Review* **77**, 94 (1950).

[107] T. Beier, P. J. Mohr, H. Persson, and G. Soff, “Influence of nuclear size on QED corrections in hydrogenlike heavy ions”, *Physical Review A* **58**, 954 (1998).

[108] J. Ullmann, Z. Andelkovic, C. Brandau, A. Dax, W. Geithner, C. Geppert, C. Gorges, M. Hammen, V. Hannen, S. Kaufmann, *et al.*, “High precision hyperfine measurements in Bismuth challenge bound-state strong-field QED”, *Nature Communications* **8**, 15484 (2017).

[109] V. A. Yerokhin and K. Pachucki, “Theoretical energies of low-lying states of light helium-like ions”, *Physical Review A* **81**, 022507 (2010).

[110] K. Pachucki and V. A. Yerokhin, “Theory of the Helium Isotope Shift”, *Journal of Physical and Chemical Reference Data* **44**, 031206 (2015).

[111] K. Pachucki and V. A. Yerokhin, “Reexamination of the helium fine structure”, *Physical Review A* **79**, 062516 (2009).

[112] E. A. Hylleraas, “Neue Berechnung der Energie des Heliums im Grundzustande, sowie des tiefsten Terms von Ortho-Helium”, *Zeitschrift für Physik* **54**, 347 (1929).

[113] V. I. Korobov, “Coulomb three-body bound-state problem: Variational calculations of nonrelativistic energies”, *Physical Review A* **61**, 064503 (2000).

[114] V. I. Korobov, “Nonrelativistic ionization energy for the helium ground state”, *Physical Review A* **66**, 024501 (2002).

[115] T. W. Hänsch, “Nobel Lecture: Passion for precision”, *Reviews of Modern Physics* **78**, 1297 (2006).

[116] J. L. Hall, “Nobel Lecture: Defining and measuring optical frequencies”, *Reviews of Modern Physics* **78**, 1279 (2006).

[117] B. J. Bloom, T. L. Nicholson, J. R. Williams, S. L. Campbell, M. Bishof, X. Zhang, W. Zhang, S. L. Bromley, and J. Ye, “An optical lattice clock with accuracy and stability at the 10^{-18} level”, *Nature* **506**, 71 (2014).

[118] S. L. Campbell, R. B. Hutson, G. E. Marti, A. Goban, N. Darkwah Oppong, R. L. McNally, L. Sonderhouse, J. M. Robinson, W. Zhang, B. J. Bloom, *et al.*, “A Fermi-degenerate three-dimensional optical lattice clock”, *Science* **358**, 90 (2017).

[119] W. Demtröder, *Laser Spectroscopy 1*, (Springer Berlin Heidelberg, 2014).

[120] J. J. Olivero and R. L. Longbothum, “Empirical fits to the Voigt line width: A brief review”, *Journal of Quantitative Spectroscopy and Radiative Transfer* **17**, 233 (1977).

[121] R. F. Garcia Ruiz, M. L. Bissell, K. Blaum, A. Ekström, N. Frömmgen, G. Hagen, M. Hammen, K. Hebeler, J. D. Holt, G. R. Jansen, *et al.*, “Unexpectedly large charge radii of neutron-rich calcium isotopes”, *Nature Physics* **12**, 594 (2016).

[122] F. Sommer, K. König, D. M. Rossi, N. Everett, D. Garand, R. P. de Groote, J. D. Holt, P. Ingram, A. Incorvati, C. Kalman, *et al.*, “Charge Radii of $^{55,56}\text{Ni}$ Reveal a Surprisingly Similar Behavior at $N = 28$ in Ca and Ni Isotopes”, *Physical Review Letters* **129**, 132501 (2022).

[123] R. P. de Groote, J. Billowes, C. L. Binnersley, M. L. Bissell, T. E. Cocolios, T. Day Goodacre, G. J. Farooq-Smith, D. V. Fedorov, K. T. Flanagan, S. Franchoo, *et al.*, “Measurement and microscopic description of odd–even staggering of charge radii of exotic copper isotopes”, *Nature Physics* **16**, 620 (2020).

[124] B. A. Marsh, T. Day Goodacre, S. Sels, Y. Tsunoda, B. Andel, A. N. Andreyev, N. A. Althubiti, D. Atanasov, A. E. Barzakh, J. Billowes, *et al.*, “Characterization of the shape-staggering effect in mercury nuclei”, *Nature Physics* **14**, 1163 (2018).

[125] M. Laatiaoui, W. Lauth, H. Backe, M. Block, D. Ackermann, B. Cheal, P. Chhetri, C. E. Düllmann, P. van Duppen, J. Even, *et al.*, “Atom-at-a-time laser resonance ionization spectroscopy of nobelium”, *Nature* **538**, 495 (2016).

[126] S. Kaufmann, “Laser spectroscopy of nickel isotopes with a new data acquisition system at ISOLDE”, Doctoral thesis (PhD thesis) (Technische Universität Darmstadt, 2019).

[127] G. Lindblad, “On the generators of quantum dynamical semigroups”, *Communications in Mathematical Physics* **48**, 119 (1976).

[128] H. J. Carmichael, *Statistical Methods in Quantum Optics 1*, (Springer Berlin Heidelberg, 1999).

[129] D. Manzano, “A short introduction to the Lindblad master equation”, *AIP Advances* **10**, 025106 (2020).

[130] R. C. Hilborn, “Einstein coefficients, cross sections, f values, dipole moments, and all that”, *American Journal of Physics* **50**, 982 (1982).

[131] R. Dum, P. Zoller, and H. Ritsch, “Monte Carlo simulation of the atomic master equation for spontaneous emission”, *Physical Review A* **45**, 4879 (1992).

[132] J. R. Johansson, P. D. Nation, and F. Nori, “QuTiP 2: A Python framework for the dynamics of open quantum systems”, *Computer Physics Communications* **184**, 1234 (2013).

[133] R. C. Brown, S. Wu, J. V. Porto, C. J. Sansonetti, C. E. Simien, S. M. Brewer, J. N. Tan, and J. D. Gillaspy, “Quantum interference and light polarization effects in unresolvable atomic lines: Application to a precise measurement of the $^{6,7}\text{Li}$ D_2 lines”, *Physical Review A* **87**, 032504 (2013).

[134] P. Müller, “Collinear laser spectroscopy of Ca^+ isotopes and design of a lens-based optical detection region”, Master thesis (Technische Universität Darmstadt, 2019).

[135] P. Virtanen, R. Gommers, T. E. Oliphant, M. Haberland, T. Reddy, D. Cournapeau, E. Burovski, P. Peterson, W. Weckesser, J. Bright, *et al.*, “SciPy 1.0: fundamental algorithms for scientific computing in Python”, *Nature methods* **17**, 261 (2020).

[136] J. D. Hunter, “Matplotlib: A 2D Graphics Environment”, *Computing in Science & Engineering* **9**, 90 (2007).

[137] S. Eckel, D. S. Barker, E. B. Norrgard, and J. Scherschligt, “PyLCP: A Python package for computing laser cooling physics”, *Computer Physics Communications* **270**, 108166 (2020).

[138] P. Müller and W. Nörtershäuser, “*qspec*: A python package for calculations surrounding laser spectroscopy”, *to be published*, <https://pypi.org/project/qspec/>.

[139] W. H. King, *Isotope Shifts in Atomic Spectra*, (Springer New York, 1984).

[140] D. York, N. M. Evensen, M. L. Martínez, and J. de Basabe Delgado, “Unified equations for the slope, intercept, and standard errors of the best straight line”, *American Journal of Physics* **72**, 367 (2004).

[141] F. Gebert, Y. Wan, F. Wolf, C. N. Angstmann, J. C. Berengut, and P. O. Schmidt, “Precision Isotope Shift Measurements in Calcium Ions Using Quantum Logic Detection Schemes”, *Physical Review Letters* **115**, 053003 (2015).

[142] D. T. Yordanov, L. V. Rodríguez, D. L. Balabanski, J. Bieroń, M. L. Bissell, K. Blaum, B. Cheal, J. Ekman, G. Gaigalas, R. F. Garcia Ruiz, *et al.*, “Structural trends in atomic nuclei from laser spectroscopy of tin”, *Communications Physics* **3**, 107 (2020).

[143] S. Lechner, T. Miyagi, Z. Y. Xu, M. L. Bissell, K. Blaum, B. Cheal, C. S. Devlin, R. F. Garcia Ruiz, J. Ginges, H. Heylen, *et al.*, “Electromagnetic moments of the antimony isotopes $^{112-133}\text{Sb}$ ”, *Physics Letters B* **847**, 138278 (2023).

[144] P. Plattner, E. Wood, L. Al Ayoubi, O. Beliuskina, M. L. Bissell, K. Blaum, P. Campbell, B. Cheal, R. P. de Groote, C. S. Devlin, *et al.*, “Nuclear Charge Radius of ^{26m}Al and Its Implication for V_{ud} in the Quark Mixing Matrix”, *Physical Review Letters* **131**, 222502 (2023).

[145] K. König, J. Krämer, P. Imgram, B. Maaß, W. Nörtershäuser, and T. Ratajczyk, “Transition frequencies and hyperfine structure in $^{113,115}\text{In}^+$: Application of a liquid-metal ion source for collinear laser spectroscopy”, *Physical Review A* **102**, 042802 (2020).

[146] W. Nörtershäuser, A. Surzhykov, R. Sánchez, B. Botermann, G. Gwinner, G. Huber, S. Karpuk, T. Kühl, C. Novotny, S. Reinhardt, *et al.*, “Polarization-dependent disappearance of a resonance signal: Indication for optical pumping in a storage ring?”, *Physical Review Accelerators and Beams* **24**, 024701 (2021).

[147] K. T. Mohr, “First laser spectroscopy of Mg^+ at CRYRING@ESR and He-Like Boron at HITRAP”, PhD thesis (Technische Universität Darmstadt, 2022).

[148] A. Neumann, R. Walser, and W. Nörtershäuser, “Raman velocity filter as a tool for collinear laser spectroscopy”, *Physical Review A* **101**, 052512 (2020).

[149] J. I. Cirac and P. Zoller, “Quantum Computations with Cold Trapped Ions”, *Physical Review Letters* **74**, 4091 (1995).

[150] P. Imgram, K. König, J. Krämer, T. Ratajczyk, R. A. Müller, A. Surzhykov, and W. Nörtershäuser, “Collinear laser spectroscopy at ion-trap accuracy: Transition frequencies and isotope shifts in the $6s\ ^2\text{S}_{1/2} \rightarrow 6p\ ^2\text{P}_{1/2,3/2}$ transitions in Ba^+ ”, *Physical Review A* **99**, 012511 (2019).

[151] P. Müller, K. König, P. Imgram, J. Krämer, and W. Nörtershäuser, “Collinear laser spectroscopy of Ca^+ : Solving the field-shift puzzle of the $4s\ ^2\text{S}_{1/2} \rightarrow 4p\ ^2\text{P}_{1/2,3/2}$ transitions”, *Physical Review Research* **2**, 043351 (2020).

[152] J. Krämer, K. König, C. Geppert, P. Imgram, B. Maaß, J. Meisner, E. W. Otten, S. Passon, T. Ratajczyk, J. Ullmann, *et al.*, “High-voltage measurements on the 5 ppm relative uncertainty level with collinear laser spectroscopy”, *Metrologia* **55**, 268 (2018).

[153] K. König, “Laser-Based High-Voltage Metrology with ppm Accuracy”, Doctoral thesis (PhD thesis) (Technische Universität Darmstadt, 2019).

[154] M. Schmidt, A. Thorn, and G. Zschornacka, “Electron Beam Ion Sources”, European Council for Nuclear Research (CERN), 2014.

[155] L. V. Jorgensen, A. Nosych, J. Sanchez-Quesada, J. Harasimowicz, G. LeGodec, M. E. Angloletta, D. Kuchler, T. Zickler, T. Eriksson, O. Capatina, *et al.*, “Extra Low ENergy Antiproton (ELENA) ring and its Transfer Lines: Design Report”, European Council for Nuclear Research (CERN), 2014.

[156] B. Maaß, K. König, J. Krämer, A. J. Miller, K. Minamisono, W. Nörtershäuser, and F. Sommer, “A 4π Fluorescence Detection Region for Collinear Laser Spectroscopy”, arXiv:2007.02658 (2020).

[157] B. Maaß, “Laser Spectroscopy of the Boron Isotopic Chain”, Doctoral thesis (PhD thesis) (Technische Universität Darmstadt, 2020).

[158] F. Köhler, “Setup of precision high-voltage dividers and laser beam transport system at ISOLDE”, Bachelor thesis (Technische Universität Darmstadt, 2022).

[159] J. Spahn, “Untergrundbereinigte kollinare Sättigungsspektroskopie an $^{12}\text{C}^{4+}$ ”, Bachelor thesis (Technische Universität Darmstadt, 2022).

[160] H. Bodnar, “Collinear laser spectroscopy of $^{155}\text{Tm}^+ - ^{175}\text{Tm}^+$ ”, Master thesis (Technische Universität Darmstadt, 2023).

[161] S. B. Reinhardt, “Measurement of Time Dilation by Laser Spectroscopy on Fast Stored Lithium Ions”, PhD thesis (Universität Heidelberg, 2005).

[162] P. Alken, E. Thébault, C. D. Beggan, H. Amit, J. Aubert, J. Baerenzung, T. N. Bondar, W. J. Brown, S. Califf, A. Chambodut, *et al.*, “International Geomagnetic Reference Field: the thirteenth generation”, Earth, Planets and Space **73**, 49 (2021).

[163] V. Patkóš, V. A. Yerokhin, and K. Pachucki, “Higher-Order QED Corrections to the Hyperfine Splitting in ^3He ”, Physical Review Letters **131**, 183001 (2023).

[164] S. D. Rosner and F. M. Pipkin, “Hyperfine Structure of the 2^3S_1 State of He^3 ”, Physical Review A **1**, 571 (1970).

[165] J. J. Clarke and W. A. van Wijngaarden, “Hyperfine and fine-structure measurements of $^{6,7}\text{Li}^+$ $1s2s\ ^3\text{S}$ and $1s2p\ ^3\text{P}$ states”, Physical Review A **67**, 012506 (2003).

[166] K. Mohr, A. Buß, Z. Andelkovic, V. Hennen, M. Horst, P. Ingram, K. König, B. Maaß, W. Nörtershäuser, S. Rausch, *et al.*, “Collinear Laser Spectroscopy of Helium-like $^{11}\text{B}^{3+}$ ”, Atoms **11**, 11 (2023).

[167] S. Ozawa, T. Ariga, N. Inabe, M. Kase, I. Tanihata, M. Wakasugi, and Y. Yano, “Isotope Shift Measurement Between He-like ^{12}C and ^{13}C Ions in $1s2s\ ^3\text{S}_1 - 1s2p\ ^3\text{P}_{0,1,2}$ Transitions”, Physica Scripta **T92**, 195 (2001).

[168] P. Müller, M. Heinz, P. Ingram, K. König, B. Maaß, W. Nörtershäuser, and A. Schwenk *et al.*, *to be published*, Data cited with this reference will be submitted to a peer-reviewed journal.

- [169] H. A. Bentz, “Kernradien von ^{12}C , ^{13}C , ^{14}N und ^{16}O aus Elektronenstreuung zwischen 30 und 60 MeV”, *Zeitschrift für Physik A Hadrons and nuclei* **243**, 138 (1971).
- [170] B. Ohayon, S. Bara, T. E. Cocolios, O. Eizenberg, A. Fleischmann, L. Gastaldo, C. Godinho, M. Heines, D. Hengstler, G. Hupin, *et al.*, “Towards Precision Muonic X-Ray Measurements of Charge Radii of Light Nuclei”, arXiv:2310.03846 (2023).
- [171] D. R. Entem and R. Machleidt, “Accurate charge-dependent nucleon-nucleon potential at fourth order of chiral perturbation theory”, *Physical Review C* **68**, 041001 (2003).
- [172] A. Ekström, G. Hagen, T. D. Morris, T. Papenbrock, and P. D. Schwartz, “ Δ isobars and nuclear saturation”, *Physical Review C* **97**, 024332 (2018).
- [173] W. G. Jiang, A. Ekström, C. Forssén, G. Hagen, G. R. Jansen, and T. Papenbrock, “Accurate bulk properties of nuclei from $A = 2$ to ∞ from potentials with Δ isobars”, *Physical Review C* **102**, 054301 (2020).
- [174] J. Simonis, S. R. Stroberg, K. Hebeler, J. D. Holt, and A. Schwenk, “Saturation with chiral interactions and consequences for finite nuclei”, *Physical Review C* **96**, 014303 (2017).
- [175] S. K. Bogner, A. Schwenk, R. J. Furnstahl, and A. Nogga, “Is nuclear matter perturbative with low-momentum interactions?”, *Nuclear Physics A* **763**, 59 (2005).
- [176] S. Hofsäss, J. E. Padilla-Castillo, S. C. Wright, S. Kray, R. Thomas, B. G. Sartakov, B. Ohayon, G. Meijer, and S. Truppe, “High-resolution isotope-shift spectroscopy of Cd I”, *Physical Review Research* **5**, 013043 (2023).
- [177] D. Röser, J. E. Padilla-Castillo, B. Ohayon, R. Thomas, S. Truppe, G. Meijer, S. Stellmer, and S. C. Wright, “Hyperfine structure and isotope shifts of the $(4s^2) ^1\text{S}_0 \rightarrow (4s4p) ^1\text{P}_1$ transition in atomic zinc”, *Physical Review A* **109**, 012806 (2024).

Curriculum Vitae

Patrick Müller

Graduation

01/2020 - 02/2024 Graduation in the group of Prof. Wilfried Nörtershäuser,
Institut für Kernphysik, Technische Universität Darmstadt.
Thesis title: *Laserspectroscopic determination
of the nuclear charge radius of ^{13}C*

Participation in experiments at
- GSI Helmholtzzentrum für Schwerionenforschung, Darmstadt
- CERN European Organization for Nuclear Research, Geneva
- Argonne National Laboratory, Chicago
- University of Jyväskylä

Member of
- Helmholtz Graduate School for Hadron
and Ion Research (HGS-HIRe)
- LASer SPECtroscopy of radioactive isotopes
and isomers Collaboration (LASPEC)
- Sonderforschungsbereich SFB 1245

Awarded with the
- M.Sc.-Forschungspreis der Gerhard Herzberg Gesellschaft 2020
- Giersch-Excellence-Award 2021

Academic Education

10/2014 - 11/2019 Physics studies (M.Sc. & B.Sc.), Technische Universität Darmstadt

11/2018 - 11/2019 Master's degree in the group of Prof. Wilfried Nörtershäuser,
Institut für Kernphysik, Technische Universität Darmstadt.
Thesis title: *Collinear laser spectroscopy of Ca^+ isotopes
and design of a lens-based optical detection region*

07/2017 - 10/2017 Bachelor's degree in the group of Prof. Wilfried Nörtershäuser,
Institut für Kernphysik, Technische Universität Darmstadt.
Thesis title: *Simulation and analysis of systematic uncertainties
of the ALIVE experiment*

School education

06/2014 Abitur at Bachgaußschule Babenhausen

List of publications

Publications in peer-reviewed journals

Collinear laser spectroscopy of Ca^+ : Solving the field-shift puzzle of the $4s\ 2\text{S}_{1/2} \rightarrow 4p\ 2\text{P}_{1/2,3/2}$ transitions

P. Müller, K. König, P. Ingram, J. Krämer and W. Nörtershäuser
Physical Review Research **2**, 043351 (2020)

Collinear Laser Spectroscopy of $2\ 3\text{S}_1 \rightarrow 2\ 3\text{P}_J$ Transitions in Helium-like $^{12}\text{C}^{4+}$

P. Ingram, K. König, B. Maaß, P. Müller and W. Nörtershäuser
Physical Review Letters **131**, 243001 (2023)

Collinear laser spectroscopy of highly charged ions produced with an electron-beam ion source

P. Ingram, K. König, B. Maaß, P. Müller and W. Nörtershäuser
Physical Review A **108**, 062809 (2023)

Nuclear Charge Radius of ^{26m}Al and Its Implication for V_{ud} in the Quark Mixing Matrix

P. Plattner, E. Wood, L. Al Ayoubi, O. Beliuskina, M. L. Bissell, K. Blaum, P. Campbell, B. Cheal, R. P. de Groot, C. S. Devlin, T. Eronen, L. Filippin, R. F. Garcia Ruiz, Z. Ge, S. Geldhof, W. Gins, M. Godefroid, H. Heylen, M. Hukkanen, P. Ingram, A. Jaries, A. Jokinen, A. Kanellakopoulos, A. Kankainen, S. Kaufmann, K. König, Á. Koszorús, S. Kujanpää, S. Lechner, S. Malbrunot-Ettenauer, P. Müller, R. Mathieson, I. Moore, W. Nörtershäuser, D. Nesterenko, R. Neugart, G. Neyens, A. Ortiz-Cortes, H. Penttilä, I. Pohjalainen, A. Raggio, M. Reponen, S. Rinta-Antila, L. V. Rodríguez, J. Romero, R. Sánchez, F. Sommer, M. Stryjczyk, V. Virtanen, L. Xie, Z. Y. Xu, X. F. Yang, and D. T. Yordanov

Physical Review Letters **131**, 222502 (2023)

Conference contributions

High-precision collinear laser spectroscopy at the Collinear Apparatus for Laser Spectroscopy and Applied Physics (COALA)

P. Ingram, K. König, J. Krämer, T. Ratajczyk, B. Maaß, P. Müller, F. Sommer, and W. Nörtershäuser
Hyperfine Interactions **241**, 48 (2020)

First experiments with a laser ablation source at the COALA setup

L. Renth, P. Ingram, J. Krämer, K. König, T. Lellinger, B. Maaß, P. Müller, T. Ratajczyk, and W. Nörtershäuser
Hyperfine Interactions **241**, 56 (2020)

Acknowledgments

Herewith I want to thank my family, friends and the people who supported me over the last years during my doctorate time.

My first thanks goes to Wilfried Nörtershauser who gave me the opportunity to work in this exciting field of physics. His commitment and support are invaluable for the productive and pleasant working environment that I enjoy very much. He also enabled me to participate in conferences, summer schools and beamtimes around the world where I got to know many other scientists.

I want to thank Matthias Heinz from the group of Achim Schwenk for providing results from nuclear structure calculations and for his valuable input on the discussion of the results.

I also wish to thank all my colleagues in the LaserSpHERe group and at COLLAPS for the many ideas, discussions and great moments. Special thanks goes to Bernhard, Jörg, Kristian and Phillip, with whom I spent a lot of thrilling time in the laboratory, to Konstantin for the exciting discussions about light-atom interactions and to Laura, Max and Simon for the fun times during conferences and beamtimes.

Thanks also goes to the administration of the Institut für Kernphysik who solved any bureaucracy issue without hesitation, first and foremost Giovanna Umberti and Carina Seeger, and also the mechanical and electrical workshop for their ideas and excellent work.

I want to thank Thorsten Kröll, Achim Schwenk and Thomas Halfmann for taking part in my rigorosum.

Of course I wish to thank my friends from school and university for the entertaining time beyond physics. I would also like to take this opportunity to thank my football colleagues for the possibility to be part of a brotherly, competitive and successful team.

I thank my entire family for their continuous support throughout my life. I want to mention especially Maria Hock for her selfless support and kindheartedness, my godparents Yvonne and Matthias for their precious support as well as my brother Manuel for the many rich interdisciplinary discussions.

Last but not least, I would like to express my utmost gratitude to my parents Ursula and Frank for their unconditional support and for bringing me forth.